

**New Studies on Thermal Transport in Metal Additive Manufacturing Processes and
Products**

Submitted in partial fulfillment of the requirements for

the degree of

Doctor of Philosophy

in

Department of Mechanical Engineering

William Lien Chin Wei

B.S., Mechanical and Electro-Mechanical Engineering, National Sun Yat-sen University

M.S., Mechanical Engineering, National Cheng Kung University

Carnegie Mellon University
Pittsburgh, PA

August 2017

© William Lien Chin Wei, 2017 All Rights Reserved

Acknowledgements

I would like to thank my parents for being a role model to me. They guide me to live a normal life and to contribute to this society wherever I am. Their guidance keeps motivating and inspiring me to progress and move forward with a positive and active attitude toward all situations.

I thank my advisor Professor Jonathan A. Malen for being an inspiring advisor, helpful mentor, and genuine friend. I thank Professor Shi-Chune Yao for being one of my committee members and providing support and suggestion in CFD simulation of phase change processes. I also thank Professor Jack Beuth in the Mechanical Engineering Departments at Carnegie Mellon University and Professor Albert To in the Mechanical Engineering and Materials Science Department at the University of Pittsburgh for serving on my committee. Last but not least, I thank Professor Alan J. H. McGaughey for helpful input and insightful feedback to my presentations in joined group meetings.

I thank Dr. Lili Ehrlich, Matthew Powell-Palm, Colt Montgomery and Dr. Keith Regner for their contributions to our publications. I also thank Dr. Wee-Liat Ong, Dr. Scott Schiffres, Professor Satbir Singh, Dr. Shubhaditya Majumdar, Dr. Justin Freedman, Dr. Kevin Parrish, Dr. Francisco Ramirez, Dr. Ankit Jain, Dr. Simon Lu, Dr. Iyu Yu, Minyoung Jeong, Dipanjan Saha, Henry Aller, and Sushant Kumar for providing the collaborative and encouraging environment. You all make my Ph.D. years so meaningful to me. I would like to acknowledge the financial support from the Department of Energy via grant DE-EE0006702. I also thank the staff at Carnegie Mellon University for their assistance and guidance, specifically in Mechanical Engineering Machine Shop. Finally, I thank the lab mates from the joined meeting of Malen, McGaughey, and Jayan's groups for helping me refine my presentation skills.

Abstract

Additive manufacturing (AM) is a manufacturing technique that adds material, such as polymers, ceramics, and metals, in patterned layers to build three-dimensional parts for applications related to medicine, aviation, and energy. AM processes for metals like selective laser melting (SLM) hold the unique advantage of fabricating metal parts with complex architectures that cannot be produced by conventional manufacturing techniques. Thermal transport can be a focal point of unique AM products and is likewise important to metal AM processes. This dissertation investigates AM metal meshes with spatially varied thermal conductivities that can be used to maximize the charge and discharge rates for thermal energy storage and thermal management by phase change materials (PCMs). Further, manufacturing these meshes demands excellent thermal control in the metal powder bed for SLM processes. Since the thermal conductivities of metal powders specific to AM were previously unknown, we made pioneering measurements of such powders as a function of gas infiltration.

In the past, thermal transport was improved in phase change materials for energy storage by adding spatially homogeneous metal foams or particles into PCMs to create composites with uniformly-enhanced (UE) thermal conductivity. Spatial variation can now be realized due to the emergence of metal AM processes whereby graded AM meshes are inserted into PCMs to create PCM composites with spatially-enhanced (SE) thermal conductivity. As yet, there have been no studies on what kind of spatial variation in thermal conductivity can further improve charge and discharge rates of the PCM. Making such mesh structures, which exhibit unsupported overhangs that limit heat dissipation pathways during SLM processes, demands understanding of heat diffusion within the surrounding powder bed. This inevitably relies on the precise knowledge of

the thermal conductivity of AM metal powders. Currently, no measurements of thermal conductivity of AM powders have been made for the SLM process.

In chapter 2 and 3, we pioneer and optimize the spatial variation of metal meshes to maximize charge and discharge rates in PCMs. Chapter 2 defines and analytically determines an enhancement ratio of charge rates using spatially-linear thermal conductivities in Cartesian and cylindrical coordinates with a focus on thermal energy storage. Chapter 3 further generalizes thermal conductivity as a polynomial function in space and numerically optimizes the enhancement ratio in spherical coordinates with a focus on thermal management of electronics. Both of our studies find that higher thermal conductivities of SE composites near to the heat source outperform those of UE composites. For selected spherical systems, the enhancement ratio reaches more than 800% relative to existing uniform foams.

In chapter 4, the thermal conductivities of five metal powders for the SLM process were measured using the transient hot wire method. These measurements were conducted with three infiltrating gases (He, N₂, and Ar) within a temperature range of 295-470 K and a gas pressure range of 1.4-101 kPa. Our measurements indicate that the pressure and the composition of the gas have a significant influence on the effective thermal conductivity of the powder. We find that infiltration with He provides more than 300% enhancement in powder thermal conductivity, relative to conventional infiltrating gases N₂ and Ar. We anticipate that this use of He will result in better thermal control of the powder bed and thus will improve surface quality in overhanging structures.

Table of contents

Acknowledgements	iii
Abstract.....	iv
List of tables.....	ix
List of figures and illustrations.....	x
List of Abbreviations	xv
1. Introduction.....	1
1.1. Approaches to thermal conductivity enhancement in phase change materials.....	3
1.1.1. Phase change materials.....	3
1.1.2. Thermal conductivity enhancement	5
1.1.2.1. Particle-like fillers	6
1.1.2.2. Matrix or foam insertions.....	7
1.2. Quantification of energy storage rates in phase change processes	7
1.2.1. Phase change processes from solid to liquid phase	8
1.2.2. Quasi-steady approximation	12
1.2.3. Effective thermal conductivity models.....	14
1.3. Thermal transport in powder beds of selective laser melting processes	17
1.3.1. Poor surface finish on overhangs.....	17
1.3.2. Characterization of thermal conductivity-transient hot wire method.....	19
1.4. Organization of the dissertation	19
2. Amplified thermal transport of PCMs using AM metal meshes for energy storage	23
2.1. Overview	23
2.2. Method.....	27
2.2.1. The Stefan problem in Cartesian coordinates.....	27
2.2.2. Nondimensionalized solution for a spatially-enhanced thermal conductivity in 1-D Cartesian coordinates.....	28
2.2.3. Validation of quasi-steady state solution in 1-D Cartesian coordinates	30
2.2.4. The Stefan problem in 1-D cylindrical coordinates	31
2.2.5. Nondimensionalized solution for a spatially-enhanced thermal conductivity in 1-D cylindrical coordinates	32
2.2.6. Parameterization of thermal conductivity of a binary composite	34

2.3.	Results and discussion	37
2.3.1.	Spatial dependence of the melting front	37
2.3.2.	Optimization of mesh design	38
2.4.	Summary	40
3.	Hot spot thermal management by phase change materials enhanced by graded metal meshes	42
3.1.	Overview	42
3.2.	Methodology	45
3.2.1.	The Stefan problem in Cartesian coordinates	45
3.2.2.	Nondimensionalized solution for a spatially-enhanced thermal conductivity in 1-D spherical coordinates	46
3.2.3.	Parameterization of thermal conductivity in a polynomial form	48
3.3.	Results and discussion	50
3.3.1.	Effects of enhancement near the heat source ($\rho_{sp} = 0$)	50
3.3.2.	Effects by concavity of κ	51
3.3.3.	Effects by ratio of radii	54
3.4.	Summary	55
3.5.	Additional consideration of mesh design	56
4.	Thermal conductivity of metal powders for powder bed additive manufacturing	58
4.1.	Overview	58
4.2.	Methodology and materials	60
4.2.1.	Sample preparation	61
4.2.2.	Experimental setup and data reduction	62
4.3.	Results and discussion	65
4.3.1.	Pressure dependent thermal conductivity	65
4.3.2.	Temperature dependent thermal conductivity	69
4.3.3.	Sensitivity analysis	72
4.4.	Summary	73
4.5.	Additional consideration of helium in selective laser melting processes	74
5.	Side project-study of thermal transport using a two-temperature model including non-surface heat deposition	76
6.	Conclusions and future work	79

6.1.	Amplified thermal transport of PCMs using AM metal meshes for energy storage..	79
6.2.	Prompt thermal transport of PCMs incorporating AM metal meshes for thermal management	80
6.3.	Thermal conductivity of metal powders for powder bed additive manufacturing	82
6.4.	Future outlook	83
6.4.1.	Experiments of the charging processes of mesh/PCM composites	83
6.4.2.	Infiltration of He in SLM machines for overhangs	83
7.	Appendix	85
7.1.	Analysis adding spatially-dependent volumetric latent heat	85
7.2.	Derivation of the maximum melting times ($t_{z,max}$ and $t_{r,max}$)	87
7.3.	Derivation of the enhancement ratio in 1-D cylindrical coordinates (ϵ_r)	87
7.4.	Derivation of the maximum melting time ($t_{sp,max}$)	88
7.5.	Derivation of the numerical solution in the dimensionless form	89
7.6.	Derivation of the coefficients $C_{cv,i}$ in Eq. (3.9)	90
7.7.	Equations and parameters in 1-D cylindrical coordinates	91
7.8.	Uncertainty analysis	92
7.9.	Simulation of a melting process of paraffin in a vertical cylinder	93
7.9.1.	Introduction	93
7.9.2.	Parameters in COMSOL	94
7.9.3.	Results	98
7.9.4.	Outlook	101
8.	References	102

List of tables

Table 1.1 Thermal conductivity and latent heat of fusion of selected phase change materials [9, 40, 41, 62-66]	4
Table 3.1 Properties and parameters of $\kappa(\rho_{sp})$	49
Table 4.1 Properties and parameters of the powder bed samples ($V= 80 \text{ mm} \times 7.5 \text{ mm} \times 7.5 \text{ mm} = 4500 \text{ mm}^3$).....	62
Table 4.2 Geometrical parameters and properties of powder bed samples of 316L stainless steel at a temperature of 295 K for pressures ranging from 1.4 – 101 kPa ($\epsilon = 0.36$, $D_p = 35 \text{ }\mu\text{m}$, $k_e^0 = 0.03 \text{ W/m-K}$, and $k_s = k_b = 13.4 \text{ W/m-K}$).....	68
Table 7.1 Uncertainty of each independent variable in the transient hot wire method from one Inconel 718 measurement	93

List of figures and illustrations

Figure 1.1 Schematics of thermal conductivity enhancement techniques for PCMs in (a) Particle-like fillers (b) Matrix/foam insertion with homogeneous distribution in space (c) Graded mesh with spatially-varied volume fraction. 6

Figure 1.2 Schematics of a melting process of PCM from solid phase to liquid phase (a) The solid PCM is heated through heat conduction on the left boundary at a higher temperature, and the melting front is formed at the melting temperature. (b) This continuously-increasing distance results in a longer path for the heat conduction from the heat source to the melting front. (c) The whole solid phase PCM completely changes to the liquid phase PCM. 8

Figure 1.3 Schematic of the temporal melting front $z_m(t)$ and volume change from solid to liquid phase dV , due to the density variation between phases. Note, for $\rho_L < \rho_S$ in Eq. (1.10), the volume is expanding ($dV = (dz_L - dz_S)A > 0$). 9

Figure 1.4 Schematic of the additive manufacturing process (a) Two-dimensional patterns is added layer by layer, resulting in a three-dimensional part [102]. (b) Complex architectures in a lattice structure and a graded mesh. 16

Figure 1.5 Schematic of selective laser melting. Each layer of metal powder is heated and then solidified according to each certain pattern until all layers are completely patterned to result in the final 3-D part. Courtesy of Santos [103]. 17

Figure 1.6 Schematic of dross and protrusion on overhangs in SLM (a) Overmelting results in dross/protrusion on the overhangs. (b) Laser power is adjusted appropriately to prevent overmelting on the overhangs. 18

Figure 2.1 Conceptual schematics of metal meshes embedded in PCMs of length d in 1-D Cartesian coordinates. (a) The volume fraction of metal mesh (gray lines) is uniform in space (z direction) and results in a uniform enhancement to thermal conductivity, k_{UE} . (b) The volume fraction of metal mesh (gray lines) is a function of space. In this case, the mesh is most dense at $z = 0$ and results in a spatially-enhanced thermal conductivity, $k_{SE} = k(z)$ that is highest at $z = 0$ 24

Figure 2.2 Dimensionless position of melting front vs. rescaled dimensionless time. The Stefan number of these similarity solutions is 0.1. The diffusivity, which is proportional to $\zeta^{\frac{(2n-1)}{n}}$ with $n = 0.5$ (Ref. [131], constant diffusivity) is approximated using Eq. (2.3) with $\kappa = 1$. The nearly

linear distribution with $n \approx 1$ in Ref. [131] is approximated using $\kappa = A\zeta + B \approx \zeta$. Under these conditions, the positions of the dimensionless melting front predicted by the quasi-steady state approximations match these exact solutions. 30

Figure 2.3 Conceptual schematics of a metal mesh embedded in a PCM with inner radius r_1 and outer radius r_2 in the 1-D cylindrical case. (a) The uniform metal mesh results in a uniform enhancement to thermal conductivity, k_{UE} . (b) The graded metal mesh as a function of r results in spatially-enhanced thermal conductivity, $k(r)$ 32

Figure 2.4 The melting front progresses differently with various intercepts B . The faster melting process with $B = 1.63$ indicates higher average charge rate. The corresponding distributions of spatially-enhanced thermal conductivity are shown in the inset where the heat source is at $\zeta = 0$ 37

Figure 2.5 The enhancement ratio is a function of B in 1-D Cartesian coordinates (Eq. (2.18)) and H in 1-D cylindrical coordinates for several values of r_2/r_1 (Eq. (2.21)). The enhancement ratio in cylindrical coordinates with $r_2/r_1 = 1.00001$ is identical to that in a 1-D Cartesian coordinates. At high radius ratios spatial enhancement can improve the average charge rate over that of uniform enhancement by more than 100%. 38

Figure 2.6 The optimal enhancement ratio ϵr_{opt} and optimal intercept H_{opt} as a function of the radius ratio r_2/r_1 at $\rho_m = 0.5$ and 1. When the melting process is complete ($\rho_m = 1$), the enhancement ratio ascends rapidly for $1 < r_2/r_1 < 10$, then it gradually grows to 2.4 as $r_2/r_1 = 1000$. When the melting process is incomplete ($\rho_m = 0.5$), even higher enhancement takes place. 39

Figure 3.1 Schematic of a hemi-spherical PCM/Mesh composite for thermal management. (a) A processor (i.e., chip) on a mobile phone creates a localized hot spot (e.g., the hot spot size is in the tens of micrometers [59]). (b) The heat dissipation from the hot spot is absorbed by the PCM/Mesh composite. (c) The cross-sectional view of the hemi-spherical PCM/Mesh composite depicts a spatial variation in volume fraction of metal mesh, which results in spatially-enhanced thermal conductivity $k(r)$ 44

Figure 3.2 The combinations of spatial variation of $\kappa(\rho_{sp})$ of degree $n = 2$ in Eq. (3.3) are constrained by the conservation of volume fraction and limitations on the minimum/maximum of $\kappa(\rho_{sp})$ (i.e., κ_{min} and κ_{max}) listed in Table 3.1. The concave-up $\kappa(\rho_{sp})$ provides a higher thermal conductivity near the hot spot. 49

Figure 3.3 The higher spatially-enhanced thermal conductivity near to the hot spot (i.e., the intercept of $\kappa(\rho_{sp})$) with $r_2/r_1 = 101$ expedites the melting front ending at $\tau_{sp} = 0.12$, and, in other words, increases the heat dissipation rate relative to UE by more than eight times..... 51

Figure 3.4 For cases with vertices at $\rho_{sp} = 1$, the maximum of enhancement ratio ($\epsilon_{sp} = 8.2$) to the heat dissipation rates with $R_{max} = 101$ in (b) is 95% higher than that ($\epsilon_{sp} = 4.2$) with $R_{max} = 11$ in (a). Vertices at $\rho_{sp} = 1$ with intercepts of κ larger than one (e.g., higher thermal conductivity near hotspot) result in concave-up $\kappa(\rho_{sp})$ and thus higher enhancement ratio than those at $\rho_{sp} = 0$ and 0.5 with both $R_{max} = 11$ and 101..... 52

Figure 3.5 The enhancement ratio using Eq. (3.10) indicates that complex concave-up $\kappa(\rho_{sp})$ with degree higher than 1 (i.e., $n > 1$) enhance heat dissipation rates by nearly 700%..... 53

Figure 3.6 The optimal enhancement ratio as a function of the ratio of radii in cylindrical (Cyl) and spherical (Sp) systems. The optimal enhancement ratio ($\epsilon_{sp,opt}$) reaches nearly 10 for $n = 2$ and 3 in spherical systems with $r_2/r_1 = 1000$. For the cylindrical systems with similarly large R_{max} , the enhancement ratios ($\epsilon_{r,opt}$) are more than 3 (more than 200%) for $n = 2$ and close to 4 ($\approx 300\%$). In both cylindrical and spherical systems, the enhancement to thermal transport in cases of $n = 2$ and 3 is distinctively higher than that of $n = 1$ (i.e., spatially-linear $\kappa(\rho_{sp})$).. 54

Figure 4.1 Transient hot wire experimental setup: (a) Measured powders were loaded into a copper test section immersing a platinum wire used for transient hot wire experiments. (b) A nichrome wire was wrapped around the copper test section to heat the measured powders up to 470 K for temperature dependence experiments. (c) The copper test section was placed in a bell jar, in which the pressure was controlled by a vacuum pump and a leak valve that feeds select gases to pressures ranging from 1.4-101 kPa. A current source and multimeter connected in a four-point configuration heated and measured the resistance of the platinum wire as a function of time to determine the thermal conductivity of the surrounding powder. (d) The normalized temperature rises of the platinum wire in DI water and the 316L stainless steel sample are plotted versus logarithmic time where the effective thermal conductivity is calculated from the slope of the fitted curve based on Eq. (4.3). 60

Figure 4.2 Thermal conductivities of the powders under Ar increases as the Ar pressure increases from 1.4 to 101 kPa at a temperature of 295 K..... 65

Figure 4.3 (a) Pressure dependent thermal conductivity of the 316L stainless steel powder. The prediction of thermal conductivity agrees with the experimental data for He and N₂ but underpredicts the experiment results for Ar. (b) The thermal accommodation coefficients established by fitting the data are compared with values from literature 66

Figure 4.4 Temperature dependent thermal conductivity of the powders at 101 kPa under Ar increases as the temperature is raised from 295 to 470 K. The thermal conductivity of 316L stainless steel and Ti-6Al-4V at 1.6 kPa under Ar and He respectively shows no temperature dependence from 295 to around 430 K..... 70

Figure 4.5 Temperature dependent thermal conductivity of the 316L stainless steel powder at 101 kPa under He, N₂, and Ar. By using the model from Ref. [152] with a temperature dependent gas thermal conductivity, we accurately match the temperature dependent data for He and N₂ but underpredict the magnitudes for Ar as we observed for pressure dependent data..... 71

Figure 4.6 Sensitivity analysis. The thermal conductivity of 316L stainless steel is predicted using Eq. (4.4) with He and N₂. In (a) and (b), the sensitivity analysis of the case infiltrated with He is tested using average powder diameter D_p and void fraction ϵ . In (c) and (d), the sensitivity analysis of the case infiltrated with Ar is tested using average powder diameter D_p and void fraction ϵ . 72

Figure 5.1 We window fit BB-FDTR phase data for silicon at $T = 300$ K from Ref. [208]. We measure and window fit BB-FDTR phase data for a gold/chromium/aluminum/silicon sample with the two-temperature model and find the thermal conductivity to be independent of heating frequency compared to the gold/chromium/silicon sample. 77

Figure 6.1 Schematic of thermal resistances of different geometries. The thermal resistance of the spherical system, near to the heat source at the dimensionless position of 0, increases much faster than the other two geometries. Therefore, when spatially-enhanced thermal conductivity is high near to the position of 0, the thermal resistance in the spherical system is greatly reduced..... 81

Figure 7.1 The difference of the optimal enhancement ratio of the average charge/discharge rates using λ and λ_{SE} vs. v_{Mesh} . With $v_{Mesh} < 0.2$, the small difference indicates that the solutions using constant λ are not significantly affected..... 86

Figure 7.2 Octadecane in the cylindrical cavity is heated by a Pt wire of 25.4 μm in diameter. The melting of Octadecane near to the top end was faster than that near to the bottom. This indicates a non-uniform melting process. 94

Figure 7.3 The settings/parameters menu showing the physical dimension and properties for the simulation..... 95

Figure 7.4 Schematic of the cross-sectional view of the cylindrical cavity and corresponding boundary conditions. The bottom and outer walls are made of thermally-insulating Acrylic (i.e.,

PMMA), whereas the top is open to the surrounding air with a weak natural convection heat transfer coefficient of 2 W/m-K..... 95

Figure 7.5 Settings of the initial condition at 295 K for the simulation. 96

Figure 7.6 The density of octadecane changes from 814 kg/m³ to 744 kg/m³ (from solid to liquid phase) [221]. 97

Figure 7.7 The viscosity of octadecane changes from 3.9×10^3 Pa·s [221] to 3.9×10^{-3} Pa·s (from solid to liquid phase). Note the viscosity of the solid phase is set six orders of magnitudes higher than that of the liquid phase so as to approximate nearly as a solid. 97

Figure 7.8 The effective specific heat varies from 2150 J/kg-K to 2180 J/kg-K (from solid to liquid phase). The latent heat of fusion is approximated as the integration of the effective specific heat versus temperature from 298 to 307 K, which is close to the latent heat of 244000 J/kg [221]... 98

Figure 7.9 The local temperatures, located at coordinates $r, h = 0.005, 0.18$ marked with a red dot, are samples for three different mesh sizes (0.0025 m, 0.001 m, and 0.0005 m). The temperature versus time points out a distinct difference among the three cases. 99

Figure 7.10 Schematics of the 3-D plot of temperature field at 10800 sec after the melting begins. 100

Figure 7.11 Schematics of the melting front and the 3-D plot of temperature and flow velocity fields (mesh size is 0.0025 m). The blue line is the melting front position at 10800 sec after the melting begins. The red arrows indicate the direction and logarithmic-scale magnitude of the flow velocity in the melted region. The higher flow velocity takes places due to natural convection. 100

List of Abbreviations

additive manufacturing (AM)	2
argon (Ar).....	17
deionized water (DI water)	61
frequency domain thermorefectance (FDTR).....	21
helium (He).....	21
Latent heat thermal energy storage (LHTES).....	1
nitrogen (N ₂)	21
one-dimensional (1-D)	24
phase change materials (PCMs).....	1
platinum (Pt)	58
selective laser melting (SLM).....	1
spatially-enhanced (SE)	19
time domain thermorefectance (TDTR).....	21
ultrathin-graphite foams (UGF)	24
uniformly-enhanced (UE).....	24

1. Introduction

Research on thermal transport is significant and critical to the performance, efficiency, and durability of a wide scope of applications, such as energy storage [1-11], thermal management of electronics [12-16], solid-state lighting [17-22], and thermoelectrics [23-28]. Thermal energy storage, especially for renewable energy, stores excess energy and bridges the gap between energy consumption and generation, because the renewable energy source is intermittent (e.g., solar irradiation rises during the day but decreases at night) [9]. Latent heat thermal energy storage (LHTES) using phase change materials (PCMs) is particularly attractive due to the high energy storage density of PCMs. However, the pioneered study of PCMs by Telkes and Raymond [29] in the 1940s did not receive much attention until the energy crisis of late 1970s when PCMs were researched for solar heating systems [30]. Since then the overall thermal behaviors of latent heat thermal storage systems have been extensively studied [31-34]. Furthermore, design fundamentals, system and process optimization, transient behavior, and field performance of phase change systems have been investigated. The research has concentrated on both the optimization of typical phase change materials and characterization of new materials. As reported from literature, a major disadvantage of common PCMs has been the low thermal conductivities, leading to low charge and discharge rates. To achieve high-performance LHTES (e.g., high charge and discharge rates), novel materials such as composites with unique transport properties provide potential solutions to improve the efficiency of latent heat thermal energy storage [8, 9, 11, 35-41]. For instance, composites consisting of metal and paraffin wax (i.e., metal/PCM) feature high effective thermal conductivity while maintaining high energy density. With higher thermal conductivity than common waxes, these composites are capable of storing energy as latent heat more efficiently in technologies such as solar energy power plants and waste heat recovery [38]. Various high thermal

conductivity substances have been investigated and dispersed as homogeneous fillers to create such high-performance composites. In addition to the composition of the composites, structural configurations of the constituents also impact the effective thermal conductivity of the composites [42]. For thermal management of electronics, PCMs are also attractive options to buffer transient thermal spikes as a thermal capacitor under transient heat loading [12-16, 43-58]. Also, critical dimensions in modern electronics operate have shrunk from tens of micrometers [59] to tens of nanometers [60, 61] and the accompanying heat dissipation per unit area is sky rocketing. These factors have motivated investigations of the geometry and material properties of PCM-based thermal management technologies. The high thermal conductivity of these metal/PCM composites in specific geometrical configurations is a potential solution to raising the effectiveness of thermal management for next-generation electronics.

Recently, metal additive manufacturing (AM), such as electron beam melting and selective laser melting (SLM), has made possible the fabrication of products with complex architectures, such as lattice and cellular structures, which cannot be fabricated by traditional manufacturing methods. AM is thus able to add extra complexity to the structural configurations of meshes embedded in PCMs; specifically through the addition of graded meshes (with spatial variation in the volume fraction of metal). Therefore, these graded meshes make the effective thermal conductivity spatially-variable. Herein we describe how this novel effect of spatially-variable thermal conductivity on thermal transport in PCM composites can be exploited to design successful AM products for thermal energy storage and thermal management.

Metal meshes are mainly composed of unsupported structures (overhangs), and these overhangs with spatial variation are realized by metal AM. Although metal AM already reveals the unique tunability of structural configurations, the surface quality of AM products, especially

overhangs, is a major issue in AM processes. The surface quality of metal AM overhangs made by SLM is limited by thermal control of the powder bed, which traps heat from the laser source and results in over-melting on overhang surfaces. The thermal conductivities of metal powders for AM have not been measured. Therefore, characterization of thermal conductivities of metal powder beds is essential to better thermal control in the powder beds of SLM processes (e.g., adjusting laser powder accordingly in overhangs).

We herein focus on thermal transport related to metal AM products, graded metal meshes, which are embedded in phase change materials as composites, as well as metal AM powder beds for the SLM processes needed to manufacture them. This dissertation investigates AM metal meshes with spatially varied thermal conductivities that can be used to maximize the charge and discharge rates for thermal energy storage and thermal management by phase change materials (PCMs). We pioneer and optimize the spatial variation of metal meshes to maximize charge and discharge rates in PCMs in different geometries. Further, manufacturing these meshes demands excellent thermal control in the metal powder bed for SLM processes. Since the thermal conductivities of metal powders specific to AM were previously unknown, we made pioneering measurements of such powders as a function of gas infiltration using the transient hot wire method.

1.1. Approaches to thermal conductivity enhancement in phase change materials

1.1.1. Phase change materials

Thermal energy can be stored in the form of sensible heat, latent heat (heat of fusion), and chemical energy. [9, 32]. For energy storage applications, compared with sensible heat, latent heat stores more thermal energy per unit volume at a constant temperature due to phase change processes [9]. Therefore, phase change materials, in which the phase change takes place from

liquid to solid or vice versa, have been considered as potential materials for thermal energy storage applications.

Table 1.1 Thermal conductivity and latent heat of fusion of selected phase change materials [9, 40, 41, 62-66]

Type of PCMs	Name of the PCM	Thermal conductivity (W/m-K)	Latent heat of fusion (kJ/kg)	Melting temperature (K)
Organics	n-Octadecane	0.148 (liquid) 0.19 (solid)	243.5	301
	n-Eicosane	0.41 (solid)		310
	n-Docosane	0.26	157	326
	Palmitic acid (98%)	0.24	208	335
Inorganics	KNO ₃	0.5	266	607
	NaNO ₃	0.5	172	581
	CaCl ₂ · 6H ₂ O	0.540 (liquid) 1.088 (solid)	190.8	303
	MgCl ₂ · 6H ₂ O	0.570 (liquid) 0.694 (solid)	167	390
Inorganic eutectics	58.7%Mg(NO ₃) 6H ₂ O-	0.51 (liquid) 0.678 (solid)	132	332
	41.3%MgCl ₂ · 6H ₂ O			
	66.6%Urea- 33.4%NH ₄	0.331 (liquid) 0.682 (solid)	161	349

Desired thermophysical, kinetic, and chemical properties of PCMs have been compiled for applications of energy storage [8, 9, 12, 32, 36-38, 41, 67-74] as well as thermal management of electronics [8, 13, 37, 40, 74-81]. For instance, PCMs with high latent heat of fusion and high density can be held in a small volume (i.e., compact size). Also, PCMs should be chemically stable and non-corrosiveness/non-toxic, which is important to the longevity of construction materials. For thermal transport, thermal conductivity, latent heat of fusion, and melting temperature are the critical thermophysical properties [38]. Table 1.1 lists the thermophysical properties of selected PCMs.

Thermal conductivity of PCMs, among the properties mentioned above, is the transport property, which quantifies the transfer rate of thermal energy by the conduction process [82]. Higher thermal conductivities of PCMs can play a key role to better transport phenomena of thermal energy, from heat sources to the phase change interface (e.g., a melting front in a melting process), and thus the charging/discharging rates in energy storage systems [8, 9, 11, 36-38]. Yet, thermal conductivities of common PCMs are low (~ 0.1 W/m-K) and orders of magnitude smaller than metals and alloys ($\sim 10^2$ W/m-K), and thus limit the efficiency and performance of the applications.

1.1.2. Thermal conductivity enhancement

To overcome the poor thermal transport in PCMs due to low thermal conductivities, enhancement of thermal transport of PCMs has been investigated using several techniques, such as finned tubes of different configurations, bubble agitation, insertion of a metal matrix into the PCM, using PCM dispersed with high conductivity particles, micro-encapsulation of the PCM, and shell and tube (multitubes) [10, 36, 38, 63, 68, 83-86]. Some of those techniques improved the thermal transport using extended surface areas to increase heat transfer rates (e.g. finned tubes and multitubes), whereas the others increase the thermal conductivity by incorporating a high thermal conductivity dispersed phase into the PCM to create a composite.

Yet, the techniques involving extended surfaces need additional volume of materials on PCMs, and thus results in weight and volume penalties on systems [87]. To avoid these penalties, enhancement of thermal conductivity by adding low volume fraction of additives (i.e., particle-like fillers) of high thermal conductivity substances is preferred as shown in *Figure 1.1a*. In addition, because the volume of the inclusion is low, the high energy storage density of pure PCMs is preserved in the composites.

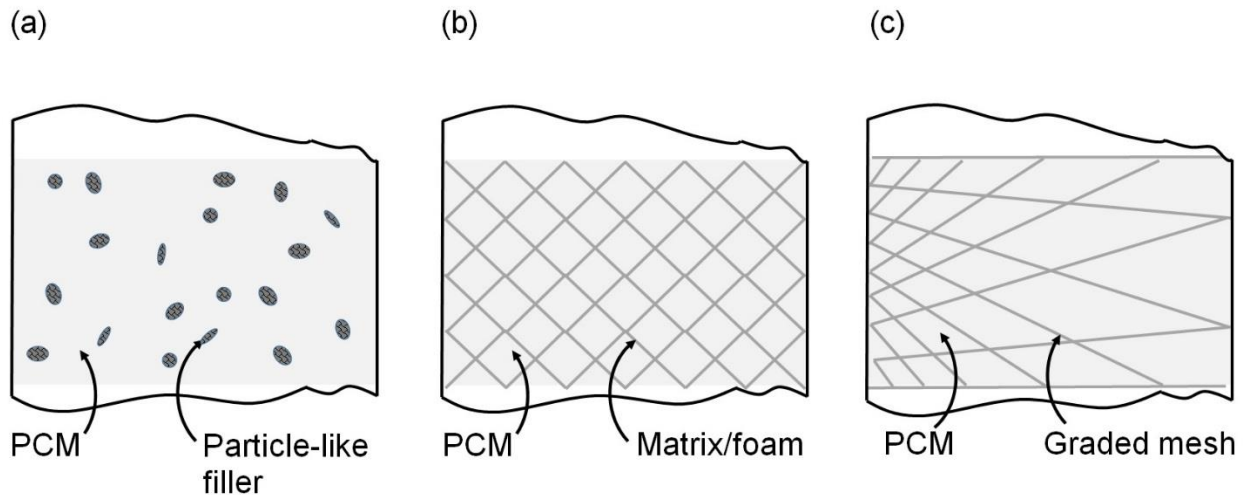


Figure 1.1 Schematics of thermal conductivity enhancement techniques for PCMs in (a) Particle-like fillers (b) Matrix/foam insertion with homogeneous distribution in space (c) Graded mesh with spatially-varied volume fraction.

1.1.2.1. Particle-like fillers

Studies have incorporated a wide range of particle-like additions (or fillers), as shown in (a), to enhance the thermal conductivity of PCMs [3, 10, 36, 38, 62, 63, 68, 83-86, 88-90]. These fillers commonly feature high thermal conductivity (e.g., single layer graphene: ~ 5000 W/m-K [90]), low density (e.g., carbon fiber: less than 2260 kg/m³ [86, 87]), and small size (e.g., multilayer graphene platelets: $\sim 1 - 2$ μm diameter and $4 - 10$ nm thickness). The thermal conductivities of these fillers, which are much higher than those of PCMs, are able to enhance thermal conductivity with the fairly low volume fraction of the fillers in the composites. Nevertheless, interfacial thermal resistances between the nano fillers and PCMs limit their effectiveness [89]. Besides the low volume fraction of fillers, low density of these fillers makes the composites lightweight. Furthermore, the fillers with small sizes (e.g., at the nanoscale) may be dispersed in PCMs more evenly than those with large sizes. For examples, the thermal conductivity of

nanocomposites of carbon nanofibers increases by 5%, with up to ~30 vol% of carbon nanofibers in the paraffin wax [87]. A maximum increase of thermal conductivity in graphene/1-octadecanol composites was ~150% with 4 wt% of nanostructured graphene [90]. The thermal conductivity of the carnauba wax/expanded graphite composite (5.92 W/m-K) was 16.4 times greater than that of carnauba wax (0.3404 W/m-K) [91].

Yet, the fillers, especially at the nanoscale, agglomerate after long-term usage that results in the unstable dispersion of these particle-like fillers in PCMs [71]. This unstable dispersion may also cause the non-homogenous concentration of the fillers, and, even worse, the sedimentation of the fillers in the composites.

1.1.2.2. Matrix or foam insertions

Matrix or foam insertions with porous structures, as shown in (b), provide an alternative to thermal conductivity enhancement without the negative concerns of particle-like fillers (e.g., agglomeration and sediment) [11, 36, 37, 40, 92-94]. These insertions commonly feature controllable porosity as well as shape and structure control of the pores [89, 93, 94]. For instance, Lafdi et al. [93] characterized cubic aluminum foams with up to 10 pores per inch and porosity as high as 96.6%. Such foams are conventionally manufactured by techniques, such as chemical vapor deposition onto a foam template [89]. Because these techniques do not provide spatial tenability of the foam volume fraction, there is no spatial variation in the resulting foam's thermal conductivity.

1.2. Quantification of energy storage rates in phase change processes

Melting and freezing during phase change processes are found in many applications, such as latent heat energy storage systems [9, 11, 36-38, 40, 41, 63, 66, 69, 72]. In these phase change processes, conduction with phase change features a moving interface (e.g., melting front in a

melting process) separating two phases (i.e., solid and liquid phases in our study) [95]. These problems involving solid-liquid phase changes are usually referred to as moving boundary, free boundary, or Stefan problems [96]. In addition, if the density change between liquid and solid phases is small, the natural convection by gravity-driven buoyancy can be neglected [82, 95]. *We herein consider phase change processes from solid to the liquid phase, where the melting front progresses and separates the solid and liquid phase.*

1.2.1. Phase change processes from solid to liquid phase

A one-dimensional melting process at three different times is shown in Figure 1.2. As shown in Figure 1.2a, the solid PCM is heated through heat conduction on the left boundary which is at a higher temperature. As the thermal energy is transferred continuously through heat conduction into the solid PCM, the temperature of the solid PCM is continuously raised. When the temperature of the solid PCM reaches a melting temperature of the PCM, a melting front is formed. Thermal energy is transferred by heat conduction from the left boundary to the melting front and is then stored as latent heat of fusion. At the same time, the solid phase PCM changes to the liquid phase PCM [82, 95].

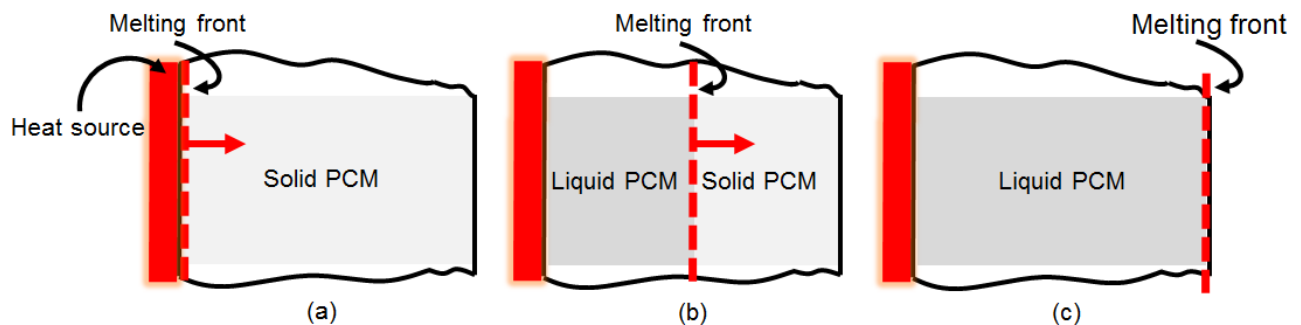


Figure 1.2 Schematics of a melting process of PCM from solid phase to liquid phase (a) The solid PCM is heated through heat conduction on the left boundary at a higher temperature, and the melting front is formed at the melting temperature. (b) This continuously-increasing distance results in a longer path for the heat conduction from the heat source to the melting front. (c) The whole solid phase PCM completely changes to the liquid phase PCM.

As shown in Figure 1.2b, the melting front progresses away from the heat source. The continuously-increasing distance between the heat source and the melting front results in a longer path for the heat conduction. In other words, the thermal resistance between the heat source and the melting front increases. As the thermal resistance continuously increases, the rate of heat transfer to the melting front is lower, and less thermal energy is stored as latent heat of fusion.

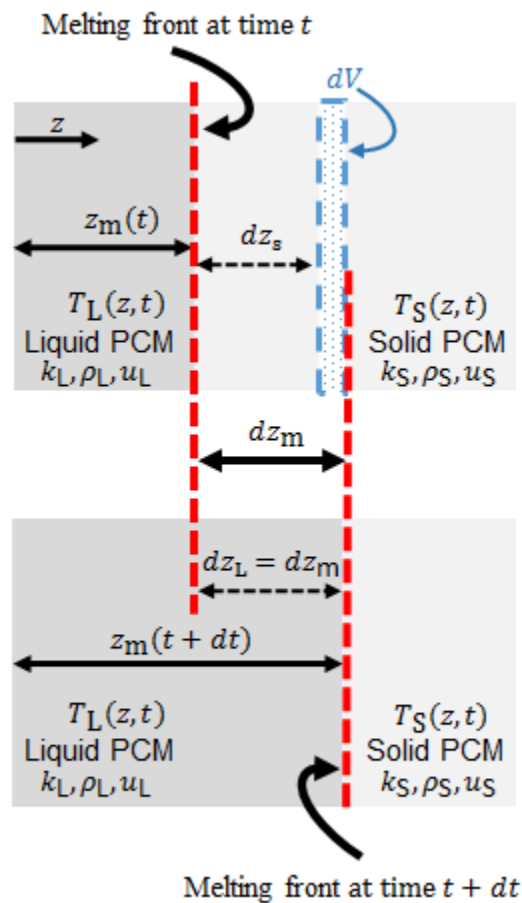


Figure 1.3 Schematic of the temporal melting front $z_m(t)$ and volume change from solid to liquid phase dV , due to the density variation between phases. Note, for $\rho_L < \rho_S$ in Eq. (1.10), the volume is expanding ($dV = (dz_L - dz_S)A > 0$).

The phase change process is quantified by an energy balance at the melting front [95].

$$\delta E = \delta E_{in} - \delta E_{out}, \quad (1.1)$$

where δE is energy change of the PCM at the melting front, δE_{in} is the energy into the melting front, and δE_{out} is the energy out of the melting front. In our case, δE_{in} is the thermal transport through heat conduction in the liquid phase PCM, whereas δE_{out} is the thermal transport leaving the melting front into solid phase PCM.

The energy terms, δE_{in} and δE_{out} , into and out of the melting front are respectively

$$\delta E_{in} = q_L dt, \quad (1.2)$$

$$\delta E_{out} = q_S dt + p dV, \quad (1.3)$$

where q is the heat transfer rate, t is time, p is the pressure on the melting front, subscripts S and L represent solid and liquid phase of PCM, and dV is volume variation of PCM changing from solid to liquid phase at the melting front as shown in Figure 1.3. In our study, δE_{in} is the thermal transport through heat conduction in the liquid phase PCM in Eq. (1.2), and δE_{out} is the thermal transport leaving the melting front into solid phase PCM in Eq. (1.3).

The energy stored at the melting front (i.e., δE in Eq. (1.1)) is equivalent to the internal energy difference between phases, described by

$$\delta E = (u_L - u_S) \delta m. \quad (1.4)$$

where u_L is the internal energy per unit mass at liquid phase PCM, and u_S is the internal energy per unit mass at solid phase. The energy terms in Eqs. (1.2), (1.3), and (1.4) are substituted into Eq. (1.1) as

$$(u_L - u_S)\delta m = q_L dt - [q_S dt + p dV], \quad (1.5)$$

or

$$(q_L - q_S)dt = (u_L - u_S)\delta m + p dV, \quad (1.6)$$

where the mass variation of PCM changing from solid to liquid phase at the melting front is δm , and q is the heat transfer rate. Heat conduction through both phases are

$$q_L = -k_L A \frac{\partial T_L(z_m, t)}{\partial z}, \quad (1.7)$$

$$q_S = -k_S A \frac{\partial T_S(z_m, t)}{\partial z}, \quad (1.8)$$

where k is the thermal conductivity of the PCM, A is the surface area normal to direction of the heat flux, T is the temperature, z_m is the melting front position, and z is position. The mass of PCM changing from solid to liquid phase at the melting front is

$$\delta m = \rho_L A dz_m, \quad (1.9)$$

where ρ_L is the density of the liquid phase PCM, and accordingly the changed volume of PCM takes the form

$$dV = \left(\frac{1}{\rho_L} - \frac{1}{\rho_S} \right) \delta m = \left(\frac{1}{\rho_L} - \frac{1}{\rho_S} \right) \rho_L A dz_m \quad (1.10)$$

Eqs. (1.7), (1.8), (1.9), and (1.10) are substituted into Eq. (1.6) as

$$\begin{aligned} & -k_L A \frac{\partial T_L(z_m, t)}{\partial z} + k_S A \frac{\partial T_S(z_m, t)}{\partial z} \\ & = (u_L - u_S)\rho_L A \frac{dz_m}{dt} + p \left(\frac{1}{\rho_L} - \frac{1}{\rho_S} \right) \rho_L A \frac{dz_m}{dt}. \end{aligned} \quad (1.11)$$

Eq. (1.11) is rearranged as

$$-k_L \frac{\partial T_L(z_m, t)}{\partial z} + k_S \frac{\partial T_S(z_m, t)}{\partial z} = \lambda \frac{dz_m}{dt}. \quad (1.12)$$

In Eq. (1.12), λ is the volumetric latent heat of fusion as

$$\lambda = \rho_L \left[\left(u_L + \frac{p}{\rho_L} \right) - \left(u_S + \frac{p}{\rho_S} \right) \right] = \rho_L [h_L - h_S], \quad (1.13)$$

where h is the enthalpy per unit mass.

Physically, during a melting process, for instance, thermal conductivity of liquid phase PCMs, k_L , is related to how efficient the thermal energy is transferred through heat condition, whereas the latent heat of fusion of PCMs, λ , represents the capacity of thermal energy stored as latent heat of fusion.

The one-dimensional heat diffusion equations, with constant properties and no energy generation, in each phase are

$$\frac{\partial^2 T_S}{\partial z^2} = \frac{C_{p,S}}{k_S} \frac{\partial T_S}{\partial t} \quad \text{for } z > z_m, \quad (1.14)$$

$$\frac{\partial^2 T_L}{\partial z^2} = \frac{C_{p,L}}{k_L} \frac{\partial T_L}{\partial t} \quad \text{for } 0 < z < z_m, \quad (1.15)$$

where $C_{p,S}$ and $C_{p,L}$ are volumetric heat capacities of solid and liquid phases.

1.2.2. Quasi-steady approximation

Due to the inherent nonlinearity of the energy equation at melting front, analytical solutions to the Stefan problems are difficult to obtain [95]. The quasi-steady model was introduced as an approximation to the exact solution and makes analytical solutions possible for various situations. The quasi-steady approximation is valid under certain criteria mentioned as follows.

According to the nondimensionalization of Eqs. (1.11), (1.14), and (1.15), the heat diffusion equations at both phases are converted as

$$\frac{\partial^2 \theta_s}{\partial \zeta^2} = Ste \frac{\partial \theta_s}{\partial \tau}, \quad (1.16)$$

$$\frac{\partial^2 \theta_L}{\partial \zeta^2} = Ste \frac{\partial \theta_L}{\partial \tau}, \quad (1.17)$$

$$-\frac{\partial \theta_L(\zeta_m, \tau)}{\partial \zeta} + \frac{\partial \theta_S(\zeta_m, \tau)}{\partial \zeta} = \frac{d\zeta_m}{d\tau}, \quad (1.18)$$

where ζ , θ , τ , and ζ_m are dimensionless position, temperature, time, and melting front position, and Ste is Stefan number [95]. The Stefan number is defined as

$$Ste = \frac{C_p \Delta T}{\lambda}. \quad (1.19)$$

In Eq. (1.19), the numerator is the sensible heat, which is the thermal energy per unit volume added to solid phase PCM so as to reach the melting temperature. Therefore, Stefan number quantifies the ratio of sensible of PCM to the latent heat of fusion.

The quasi-steady approximation is appropriate when $Ste < 0.1$. From Eq. (1.19), smaller $Ste \approx 0$ indicates that the sensible heat $C_p \Delta T \approx 0 \rightarrow C_p \approx 0$, and thus implies that thermal diffusivity of the PCM is infinite (i.e., $k/C_p \rightarrow \infty$). Physically, a small Stefan number means that the thermal effects propagate with extremely high speed, and thus a steady state is reached instantaneously at each moment [95, 97]. Given a small Stefan number, the quasi-steady approximation can be applied to Eqs. (1.16) and (1.17) as

$$\frac{\partial^2 \theta_s}{\partial \zeta^2} = 0, \quad (1.20)$$

$$\frac{\partial^2 \theta_L}{\partial \zeta^2} = 0. \quad (1.21)$$

The transformed heat diffusion equations (Eqs. (1.20) and (1.21)), with Eq. (1.18) using appropriate initial and boundary conditions, provide approximate solutions close to exact solutions.

1.2.3. Effective thermal conductivity models

From Eq. (1.12), the thermal conductivity of the PCM is critical. For instance, during a melting process, higher thermal conductivity of PCMs, k_L (we will use k instead of k_L in the remaining content of this dissertation), can reduce the thermal resistance between the heat source and the melting front and thus improve the thermal transport.

Effective thermal conductivity models predict the effective thermal conductivity of composites [42]. The prediction by these models depends on parameters including the thermal conductivities and volume fractions of the constituent phases in the composites (e.g., a metal mesh and a PCM in our study). There are five common effective thermal conductivity models: the Parallel, Series, Maxwell-Eucken 1, Maxwell-Eucken 2, and effective medium theory models. The mathematical forms of these models are categorized specifically based on the structures or configurations of the constituents in the composites. The detail of these models can be found in Ref. [42].

Based on the bi-continuous metal mesh and PCM phases. The Parallel model has been utilized as an appropriate model for the effective thermal conductivity [89, 97]. The general form of the Parallel model is

$$k = k_{\text{PCM}}(1 - v_{\text{Mesh}}) + k_{\text{Mesh}}v_{\text{Mesh}} \quad (1.22)$$

where k_{PCM} is the thermal conductivity of the PCM, k_{Mesh} is the thermal conductivity of the metal mesh, and v_{Mesh} is the volume fraction of the metal mesh. v_{Mesh} is a constant in uniformly-enhanced thermal conductivity, whereas, as introduced in the following sections, *the parallel model modified with spatially-varied volume fraction is incorporated in our analysis for AM graded meshes.*

1.2.4. AM graded mesh with spatially-varied volume fraction

Recently additive manufacturing (AM) is capable of fabricating complex patterns, which are impossible with conventional manufacturing techniques, such as lattice structures and graded meshes shown in Figure 1.4. Additive manufacturing (or rapid prototyping) is a technique adding two-dimensional patterns layer by layer and resulting in a three-dimensional part [98-101]. A variety of AM processes, such as stereolithography (SL), direct light projection (DLP), fused deposition modeling (FDM), inkjet, electron beam melting, and selective laser melting, are capable of fabricating parts from diverse materials, such as polymers, ceramics, and metals [98, 99]. AM is especially beneficial to the rapid prototyping of new parts, which is cost-effective in terms of tooling and can shorten the part development processes.

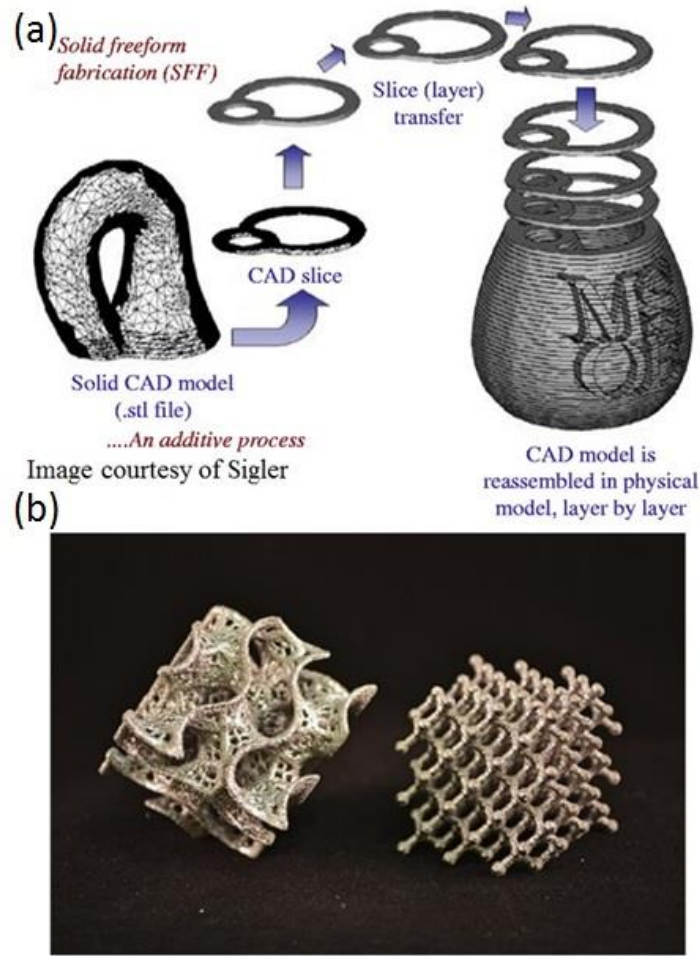


Figure 1.4 Schematic of the additive manufacturing process (a) Two-dimensional patterns is added layer by layer, resulting in a three-dimensional part [102]. (b) Complex architectures in a lattice structure and a graded mesh.

For our study on AM graded mesh/PCM composites, the spatially-varied volume fraction of the metal can be realized by metal SLM processes. Mathematically, based on the spatially-varied volume fraction of the metal, the Parallel model in Eq. (1.22) is modified as

$$k = k_{\text{PCM}}(1 - v'_{\text{Mesh}}) + k_{\text{Mesh}}v'_{\text{Mesh}} \quad (1.23)$$

where v'_{Mesh} is the spatially-varied volume fraction of the metal. ***This unique feature of AM motivated us to investigate whether spatially-varied thermal conductivity of graded mesh/PCM***

composites can improve thermal transport of PCMs further and outperform homogeneous matrices/foams.

1.3. Thermal transport in powder beds of selective laser melting processes

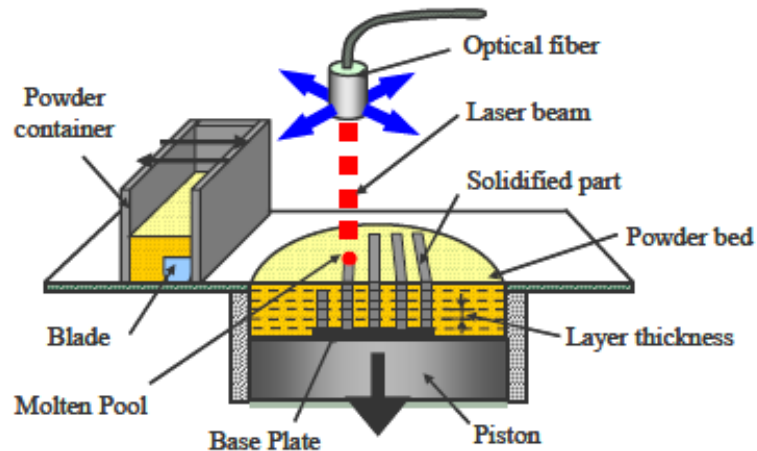


Figure 1.5 Schematic of selective laser melting. Each layer of metal powder is heated and then solidified according to each certain pattern until all layers are completely patterned to result in the final 3-D part. Courtesy of Santos [103].

Selective laser melting, also called direct laser sintering, has been used to manufacture metal parts for medical, aviation, and energy applications [102, 104]. As shown in Figure 1.5, the laser beam heats and melts a layer of metal powder (e.g., each layer is approximately 20 μm thick in EOS M270 machines) according to a specified pattern under a controlled environment filled with an inert gas, such as argon (Ar). After the melted pattern has solidified, a new layer of metal powder is spread by a blade and the process is repeated [103]. After multiple layers are patterned in succession, a three-dimensional part is formed [104-106].

1.3.1. Poor surface finish on overhangs

During all AM processes, supporting structures are essential to hold the built parts in position and to maintain the configurations of the parts. Structurally, the metal powder bed serves

as a temporary support to the metal part, whereas other AM processes, such as SL, DLP, and FDM, use the additional raw materials to print the supporting structures, in addition to the parts themselves [98, 104, 105]. The printed supporting structures cannot be reused. Therefore, these metal powder beds can save the usage of raw materials for the supporting structures.

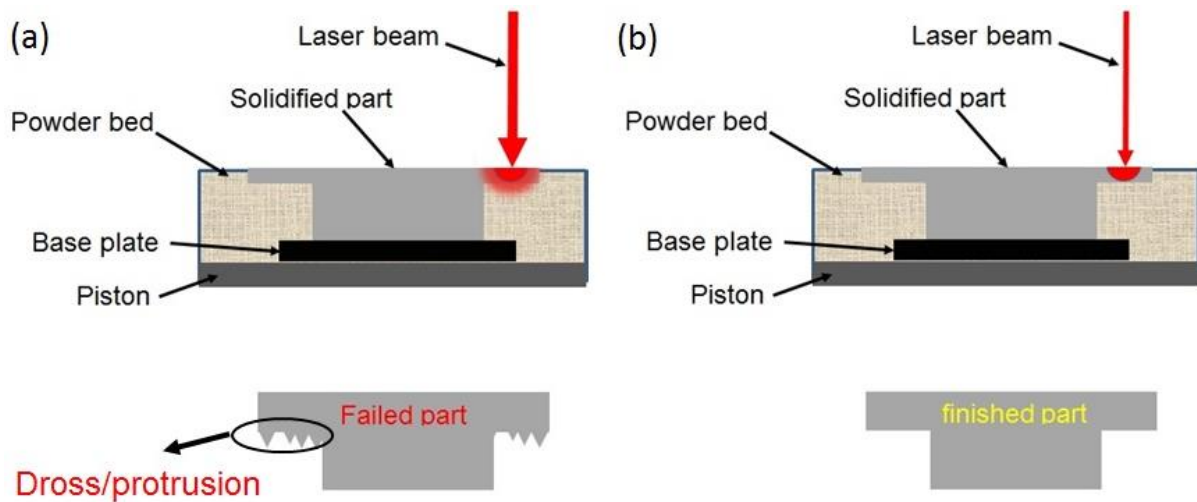


Figure 1.6 Schematic of dross and protrusion on overhangs in SLM (a) Overmelting results in dross/protrusion on the overhangs. (b) Laser power is adjusted appropriately to prevent overmelting on the overhangs.

Yet, the supporting powder is thermally disadvantageous to overhangs. As shown in Figure 1.6, the heat from the laser beam melts each layer of powder, and the melted powder particles are bonded together to a solidified layer pattern. After being bonded during the solidification, the phase change from liquid back to solid phase is an exothermic process. In the exothermic process, the heat is effectively dissipated through the solidified part which sits on the thermally conductive base plate. For overhangs, however, the solidified part does not sit on the thermally conductive base plate but is instead surrounded by the thermally insulating metal powder. This thermal trap causes an overmelting outside the patterned overhangs, perceived in the finished part as poor surface finish, dross, or protrusion, as shown in Figure 1.6a.

Hence, thermal control in metal SLM processes is especially significant to the surface finish of the overhangs in metal AM parts. If production parameters, such as the laser power and laser feed speed, can be adjusted specifically in overhang regions, the surface quality can be improved. Appropriate adjustment of these parameters relies on the precise knowledge of the thermal conductivity of AM metal powders. There are, however, no experimental studies of thermal conductivity of the metal powders used for SLM.

1.3.2. Characterization of thermal conductivity-transient hot wire method

We characterized the thermal conductivities of several AM metal powders for the SLM processes using the transient hot wire method [107-111]. The transient hot wire method is chosen because the AM metal powder can be arranged in a configuration similar to the powder bed in the AM machines, and thus “a hot wire” was easy to embed within the powder. Besides that, this transient hot wire method takes less measurement time than conventional steady state methods.

1.4. Organization of the dissertation

An overview of the organization of chapters in this dissertation and their scope is presented below:

Chapter2: Amplified thermal transport of PCMs using AM metal meshes for energy storage

[This chapter has been published as Wei, L. C. and J. A. Malen (2016). *Applied Energy* 181: 224-231].

Composites made with high thermal conductivity meshes embedded in phase change materials increase charge/discharge rates of latent heat energy storage systems. We study the benefits of spatially-dependent enhancements to thermal conductivity on the charge/discharge rates of PCMs in both one-dimensional Cartesian and one-dimensional cylindrical coordinates.

Our nondimensionalized quasi-steady (Stefan number < 0.1) solution indicates that the average charge (discharge) rate in a spatially-enhanced PCM outperforms the uniformly-enhanced case by maximizing the enhancement near the heat source and therein reducing the time-averaged thermal resistance to melting (solidifying). Relative to a uniformly-enhanced thermal conductivity, the optimal charge/discharge rate enhancement is a modest 12% in one-dimensional Cartesian coordinates but as high as 140% in one-dimensional cylindrical coordinates.

Chapter 3: Hot spot thermal management by phase change materials enhanced by graded metal meshes

[This chapter is in preparation for submission to *Applied Thermal Engineering*.]

Phase change materials (PCMs) provide a potential solution to thermal management of electronics. To maximize heat dissipation rates, the low thermal conductivity of PCMs has been enhanced by incorporating spatially-homogeneous porous fillers with high thermal conductivities. Relative to spatially-uniform fillers, we investigate the advantages of porous fillers with spatially-enhanced (SE) thermal conductivity. An arbitrary polynomial form of the spatial variation is optimized to enhance heat dissipation rates in one-dimensional cylindrical and spherical coordinates. The most desirable spatial distributions have higher thermal conductivity near the hot spot and concave-up shapes. Using a spatially-optimized thermal conductivity profile, we find enhancement of heat dissipation rates of up to more than 800% and 200% over those using uniform fillers of equivalent average volume fractions in spherical and cylindrical coordinates. One option to realize these structures is with additively-manufactured metal meshes of spatially graded volume fraction.

Chapter 4: Thermal conductivity of metal powders for powder bed additive manufacturing

[This chapter has been submitted to *Additive Manufacturing* and under review]

The thermal conductivities of five metal powders for powder bed additive manufacturing (Inconel 718, 17-4 stainless steel, Inconel 625, Ti-6Al-4V, and 316L stainless steel) were measured using the transient hot wire method. These measurements were conducted with three infiltrating gases (argon, nitrogen (N₂), and helium (He)) within a temperature range of 295-470 K and a gas pressure range of 1.4-101 kPa. The measurements of pressure dependent thermal conductivity indicate that the pressure and the composition of the gas have a significant influence on the effective thermal conductivity of the powder, but the metal powder properties and temperature do not. Our measurements provide a guideline for optimizing laser parameters in order to improve thermal control of powder beds in selective laser melting processes, especially in overhangs and cellular geometries where heat dissipation by the powder is critical.

Chapter 5: Side project-study of thermal transport using a two-temperature model including non-surface heat deposition

[This chapter has been published as Regner, K. T., et al. (2015). *Journal of Applied Physics* 118(23): 235101.]

In this project, I helped formulate and apply additional functionality to an existing two-temperature model for interpreting thermoreflectance measurements. This model interprets how different metal transducers result in opposing observations of frequency-dependent thermal conductivity in silicon when measured by broadband frequency domain thermoreflectance (FDTR) and time domain thermoreflectance (TDTR).

Chapter 6: Conclusions and future work

This chapter concludes the major contributions of my completed work and suggestions for future research in thermal transport that leverages additive manufacturing.

2. Amplified thermal transport of PCMs using AM metal meshes for energy storage

This chapter has been published as Wei, L. C. and J. A. Malen (2016). *Applied Energy* 181: 224-231.

2.1. Overview

The present-day mismatch between increasing power demand and limited energy resources motivates the discovery of novel and renewable energy sources and improvements to the energy efficiency of power conversion systems [37, 38, 69]. To improve utilization of renewable resources, energy storage devices and systems that reduce the imbalance between intermittent supply and demand are critical [37]. Research on thermal energy storage has improved the design of green buildings [50, 72], utilization of solar thermal energy [41, 112, 113], and recovery of waste heat [38].

Thermal energy can be stored in the form of sensible heat and latent heat [41]. Thermal energy storage in the form of sensible heat occurs primarily through the activation of vibrations, realized as heat capacity within the storage material. Thermal energy storage in the form of latent heat occurs through the breaking of chemical bonds when a substance changes from one phase to another phase at a constant temperature. Phase change materials can store more energy per unit volume in the form of latent heat than can be stored by sensible heat at practical temperature differences. For example, the temperature of a wax such as n-Octadecane (latent heat: $243.5 \text{ kJ}\cdot\text{kg}^{-1}$ at a melting temperature of 300.8 K and solid phase specific heat: $2.14 \text{ kJ}\cdot\text{kg}^{-1}\cdot\text{K}^{-1}$ [9]) has to be increased by more than 110 K for the sensible heat to equal the latent heat of fusion. Moreover, extended storage of energy at this elevated temperature requires increased insulation

relative to the PCM, which can be stored just above its melting temperature therein limiting the temperature difference driving heat loss. Hence, energy storage systems incorporating PCMs are used to meet high energy storage requirements in applications such as solar thermal power plants and thermal management systems [41, 68]. PCM-filled heat exchangers that rapidly dissipate heat can be employed for thermal management in small-sized dynamic systems, such as telecommunications devices and home appliances [114]. PCM-embedded (paraffin/expanded graphite) wall boards that react quickly to regulate temperature can reduce and shift the average consumption and peak loading of building electricity demands [115].

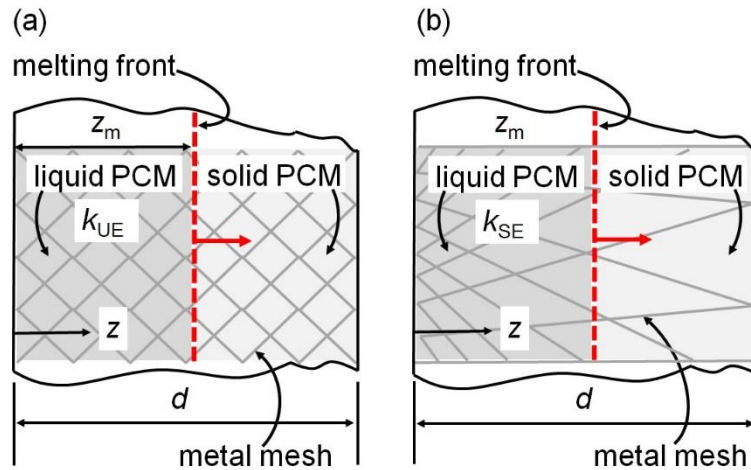


Figure 2.1 Conceptual schematics of metal meshes embedded in PCMs of length d in 1-D Cartesian coordinates. (a) The volume fraction of metal mesh (gray lines) is uniform in space (z direction) and results in a uniform enhancement to thermal conductivity, k_{UE} . (b) The volume fraction of metal mesh (gray lines) is a function of space. In this case, the mesh is most dense at $z = 0$ and results in a spatially-enhanced thermal conductivity, $k_{SE} = k(z)$ that is highest at $z = 0$.

Energy storage rates (also known as charge rates) of PCMs are governed by their thermal conductivity, which dictates the rate that heat reaches the solid-liquid interface. Low thermal conductivities of PCMs limit the charge (discharge) rate during melting (solidification) [116]. High thermal conductivity fillers such as carbon fiber, carbon nanotubes, graphite, graphite flakes, graphene nanocomposites, and expanded graphite have been dispersed into PCMs to increase their

thermal conductivities [15, 87, 90, 91, 117, 118]. However, the dispersion of these particle-like fillers may not be stable after long-term usage [71]. Nanoscale dispersed fillers also encounter appreciable thermal interface resistance between the filler and the PCM that limits their effectiveness [89].

Another method to overcome the low thermal conductivity of PCMs is through the incorporation of a high thermal conductivity porous structure [92] (e.g., foams or metal meshes) as depicted in Figure 2.1a. These structures are fixed, non-moving and continuous [36]. Successful implementation of high thermal conductivity porous structures made of copper, aluminum, and graphite have been investigated [85, 93, 119, 120]. Non-metals, such as PCM-expanded graphite were also shown to experimentally shorten charging times [119]. For ultrathin-graphite foams (UGF), Ji et al. [89] found that the enhancement in thermal conductivity per unit volume fraction exceeded metal fillers. They [89] also predicted the composite's thermal conductivity using a specific rule of mixtures [121] based on the structure and the volume fraction of UGF. In all of these cases, the enhancement of thermal conductivity was spatially uniform because the porous matrices were homogeneous.

Although the uniformly-enhanced (UE) thermal conductivity in a mesh embedded PCM composite in Figure 2.1a enhances the charge/discharge rates, we analyze whether a spatially-varied thermal conductivity, depicted in Figure 2.1b, can further enhance the charge/discharge rates while conserving the amount of added material. Due to the development of advanced fabrication techniques such as additive manufacturing, spatially complex architectures can be readily fabricated, and a spatially-varied thermal conductivity is feasible [122, 123]. The goal of our analysis is to determine the optimal spatially-varied thermal conductivity to charge/discharge PCMs faster than those with a uniformly-enhanced thermal conductivity. To do so, we develop

novel analytical solutions to the one-dimensional (1-D) Stefan problem under the quasi-steady state approximation incorporating a spatially-varied thermal conductivity generalized as a linear function of space in 1-D Cartesian and 1-D cylindrical coordinates. All the equations and solutions are nondimensionalized in space and time and compared to those of the uniformly-enhanced case. We find that relative to uniform enhancement with identical total mass, the maximum enhancement is just 12% in the planar geometry but can be more than 100% in the cylindrical geometry.

Melting phenomena of PCMs involving heat conduction with phase change at a moving interface or melting front, known as Stefan problems, were first studied in a one-dimensional water-ice system [96]. Neumann used an error function to propose a classic solution [95]. Tarzia considered new problems with a moving interface and assembled explicit and approximate solutions involving heat and mass transfer [124]. An exponential distribution of mass diffusivity was recently considered to determine the moisture content in soybeans [125]. Similarity solutions using varying diffusivity as a function of temperature or position were also developed [126-132]. In Ref. [128], an alternative nonlinear thermal diffusivity distribution was considered for evaporation modeling in soil mechanics. This solution was later modified so the nonlinear term was thermal conductivity instead of thermal diffusivity [127, 128], and then further modified to include convective effects [129, 130]. Voller and Falcini [131] utilized a power law diffusivity in Cartesian coordinates, motivated by sedimentary mass transport scenarios in fluvial systems. We herein generalize Voller and Falcini's result by including parameters that independently control the intercept and slope of a linear distribution for thermal conductivity, and optimize them based on maximizing charge/discharge rates in PCMs.

2.2. Method

2.2.1. The Stefan problem in Cartesian coordinates

The one-dimensional heat diffusion equation in a Stefan problem can be solved using the quasi-steady state approximation when the Stefan number $Ste < 0.1$. The Stefan number is defined as the ratio of the sensible heat to the latent heat $Ste = C_p \Delta T / \lambda$ where C_p is the volumetric heat capacity of a PCM, $\Delta T = T_s - T_m$ where T_s is a temperature of a heat source on the surface and T_m is a melting temperature of the PCM, and λ is the volumetric latent heat of fusion for the PCM [95]. The quasi-steady heat diffusion equation is expressed as

$$\frac{\partial}{\partial z} \left[k(z) \frac{\partial T(z, t)}{\partial z} \right] = 0, \quad (2.1)$$

where z is the coordinate, $k(z)$ is the spatially-varied thermal conductivity of a composite, $T(z, t)$ is the temperature of the PCM, and t is time. Schematics of PCM composites of length d with uniformly-enhanced thermal conductivity k_{UE} and spatially-enhanced thermal conductivity k_{SE} are shown in Figure 2.1a and b. The volume fraction of metal mesh in Figure 2.1a is uniform in space and results in k_{UE} , while the volume fraction of metal mesh in Figure 2.1b is most dense at $z = 0$ and results in k_{SE} that is highest at $z = 0$.

With constant temperature boundary conditions of $T(0, t) = T_s$ and $T(z_m(t), t) = T_m$, the temperature of the composite for $0 \leq z \leq z_m$ is solved, where z_m is the time-dependent melting front position. The temperature in the solid phase (for a melt process) is assumed to be at T_m , so no sensible heat is required.

The energy balance at the melting front [95] is

$$-k(z) \frac{\partial T(z, t)}{\partial z} \Big|_{z=z_m(t)} = \lambda \frac{dz_m(t)}{dt}. \quad (2.2)$$

For small mesh volume fractions, it is reasonable to assume k is independent of z though this is indeed an approximation made to facilitate analytical solutions (in section 7.1 we validate this assumption for volume fractions less than 0.2). The initial condition for the melting front position z_m in Eq. (2.2) is $z_m(t = 0) = 0$.

To nondimensionalize our result the thermal conductivity $k(z)$ in Eq. (2.1) is written as $k(\zeta)$ where a dimensionless coordinate is defined as $\zeta = z/d$, and d is the length of the PCM/mesh composites shown in Figure 2.1 (ζ ranges from 0 to 1). Then, we define $\kappa(\zeta) = k(\zeta)/k_{UE}$ and assume a linear form of $\kappa(\zeta)$ in Cartesian coordinates as

$$\kappa(\zeta) = A\zeta + B, \quad (2.3)$$

where A and B are adjustable coefficients. This linear form of $\kappa(\zeta)$, where the slope and intercept can be independently varied, was chosen for simplicity to reach analytical solutions. Refs. [127-131] also consider heterogeneous diffusivities, but with differing forms relevant to their application in fluvial and oceanic sedimentary phenomena. A power law based dimensionless diffusivity $D \propto \zeta^{\frac{2n-1}{n}}$ where $0 < n < 1$ is considered in Ref. [131]. Although $n = 1$ creates a spatially-linear distribution, the intercept and the slope cannot be adjusted separately, which we later identify as crucial to enhancing PCM charge and discharge rates. Using our linear form provides straightforward proof that spatial variation of thermal conductivity can outperform the uniform PCM/mesh composite.

2.2.2. Nondimensionalized solution for a spatially-enhanced thermal conductivity in 1-D Cartesian coordinates

We further nondimensionalize Eq. (2.1) by substituting the dimensionless coordinate $\zeta = z/d$, thermal conductivity $\kappa(\zeta) = k(\zeta)/k_{UE}$, and temperature $\theta(\zeta, \tau_z) = [T(\zeta, \tau_z) - T_m]/(T_s - T_m)$ where $\tau_{z,max}$ is the dimensionless time based upon $t_{z,max} = \lambda d^2/[2k_{UE}(T_s - T_m)]$, the total

melting time for a uniform PCM/mesh composite (see section 7.2 for the derivation of $t_{z,\max}$). The dimensionless temperature ranges from 0 and 1 since the temperature difference between heat source (T_s) and melting front (T_m) is the maximum temperature difference during the melting process. Notably, if $\kappa(\zeta) = 1$ ($A = 0, B = 1$), we recover the solution for k_{UE} . By doing so, we arrive at the dimensionless heat diffusion equation for 1-D Cartesian coordinates

$$\frac{\partial}{\partial \zeta} \left[\kappa(\zeta) \frac{\partial \theta(\zeta, \tau_z)}{\partial \zeta} \right] = 0. \quad (2.4)$$

The dimensionless temperature distribution in the melted PCM from Eq. (2.4) using dimensionless boundary conditions ($\theta = 1$ at $\zeta = 0$, and $\theta = 0$ at $\zeta = \zeta_m = z_m/d$) is obtained as

$$\theta(\zeta, \tau_z) = 1 - \frac{\ln\left(\frac{A\zeta}{B} + 1\right)}{\ln\left(\frac{A\zeta_m}{B} + 1\right)}. \quad (2.5)$$

The energy balance from Eq. (2.2) can be similarly nondimensionalized as

$$-\kappa(\zeta) \frac{\partial \theta(\zeta, \tau_z)}{\partial \zeta} \Big|_{\zeta=\zeta_m(\tau_z)} = 2 \frac{d\zeta_m(\tau_z)}{d\tau_z}. \quad (2.6)$$

Solving Eq. (2.6) with the initial condition of $\zeta_m(\tau_z = 0) = 0$ results in the following relationship between ζ_m and τ_z

$$\tau_z = \frac{2}{A} \left[\ln\left(\frac{A\zeta_m}{B} + 1\right) \left(\zeta_m + \frac{B}{A}\right) - \zeta_m \right]. \quad (2.7)$$

Because the same amount of PCM is melted in both cases, $\tau_{z,\max}(\zeta_m = 1)$ is the total melting time of the spatially-enhanced PCM relative to the uniformly-enhanced PCM. A value of $\tau_{z,\max}$ less than one implies that a faster melting process takes place. Hence, the average charge rate is proportional to $1/\tau_{z,\max}$. The enhancement ratio ϵ_z of the average charge rate of the

spatially-enhanced PCM to that of the uniformly-enhanced PCM is hence equivalent to the reciprocal of Eq. (2.7) with $\zeta_m = 1$

$$\epsilon_z(A, B) = \frac{A}{2 \left[\ln \left(\frac{A}{B} + 1 \right) \left(1 + \frac{B}{A} \right) - 1 \right]} \quad (2.8)$$

2.2.3. Validation of quasi-steady state solution in 1-D Cartesian coordinates

Our quasi-steady solution is compared with an exact similarity solution using a spatially-dependent thermal diffusivity [131].

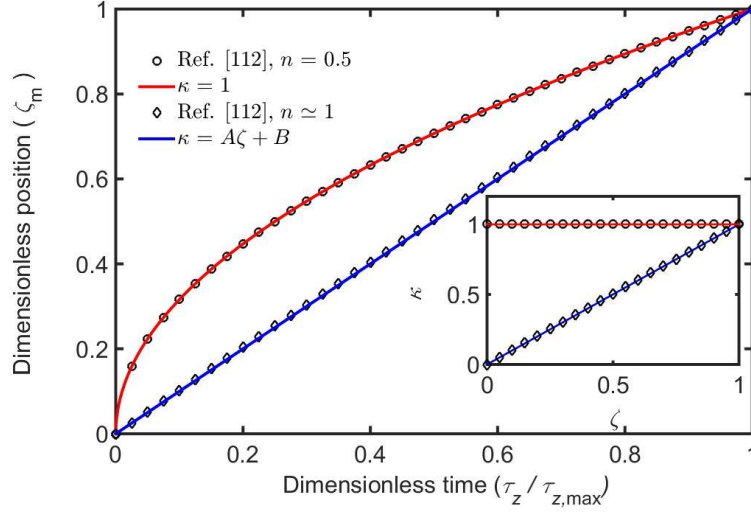


Figure 2.2 Dimensionless position of melting front vs. rescaled dimensionless time. The Stefan number of these similarity solutions is 0.1. The diffusivity, which is proportional to $\zeta^{\frac{(2n-1)}{n}}$ with $n = 0.5$ (Ref. [131], constant diffusivity) is approximated using Eq. (2.3) with $\kappa = 1$. The nearly linear distribution with $n \simeq 1$ in Ref. [131] is approximated using $\kappa = A\zeta + B \simeq \zeta$. Under these conditions, the positions of the dimensionless melting front predicted by the quasi-steady state approximations match these exact solutions.

In Ref. [131], the diffusivity is formulated as a power law of position, $\zeta^{\frac{(2n-1)}{n}}$ where $0 < n < 1$. In Figure 2.2, we compare our results to their solutions with $n = 0.5$ and $n \simeq 1$. For a constant diffusivity ($n = 0.5$) in Figure 2.2, we set $\kappa = 1$ in Eq. (2.3). For a nearly linear distribution with $n \simeq 1$, we use a spatially-dependent thermal conductivity $\kappa = A\zeta + B \simeq \zeta$ with $A = 1$ and $B \simeq 0$. The spatial dependence of κ is shown in the inset of Figure 2.2.

A comparison of the dimensionless position of the melting front ζ_m is shown in Figure 2.2. With $Ste = 0.1$ the positions of the melting front under the quasi-steady state approximation with both constant thermal conductivity and spatially-dependent thermal conductivity are identical to Ref. [131].

2.2.4. The Stefan problem in 1-D cylindrical coordinates

Cylindrical systems that experience temperature gradients in the radial direction are prevalent in energy storage applications [82]. During the melting process, the temperature $T(r_1, t) = T_s$ at the inner surface $r = r_1$ is higher than the melting temperature $T(r_m, t) = T_m$ at $r = r_m$ in Figure 2.3 where r is the radial coordinate, r_1 is the inner radius of the PCM/mesh composite, and r_m is the melting front position. The melting process starts at $r = r_1$ and progresses until the melting front arrives at the outer surface at $r = r_2$. The heat diffusion equation in a one-dimensional cylindrical system is

$$\frac{1}{r} \frac{\partial}{\partial r} \left[rk(r) \frac{\partial T(r, t)}{\partial r} \right] = 0. \quad (2.9)$$

The temporal position of the melting front is again determined using the energy balance at $r = r_m(t)$

$$-k(r) \frac{\partial T(r, t)}{\partial r} \Big|_{r=r_m(t)} = \lambda \frac{dr_m}{dt}. \quad (2.10)$$

The initial condition for the melting front is $r_m(t = 0) = r_1$.

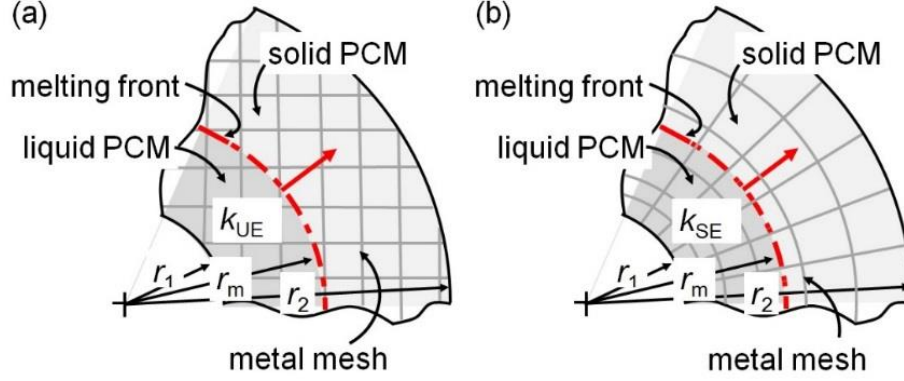


Figure 2.3 Conceptual schematics of a metal mesh embedded in a PCM with inner radius r_1 and outer radius r_2 in the 1-D cylindrical case. (a) The uniform metal mesh results in a uniform enhancement to thermal conductivity, k_{UE} . (b) The graded metal mesh as a function of r results in spatially-enhanced thermal conductivity, $k(r)$.

The radial coordinate is nondimensionalized by the thickness of the annulus ($r_2 - r_1$) of the PCM/mesh composite as shown in Figure 2.3, and the dimensionless radial coordinate defined as $\rho = (r - r_1)/(r_2 - r_1)$ ranges from 0 to 1. Thus, the dimensionless thermal conductivity of linear radial dependence is

$$\kappa(\rho) = G\rho + H. \quad (2.11)$$

where G is the slope and H is the intercept of the linear distribution.

2.2.5. Nondimensionalized solution for a spatially-enhanced thermal conductivity in 1-D cylindrical coordinates

Eq. (2.9) is nondimensionalized using the dimensionless radial coordinate $\rho = (r - r_1)/(r_2 - r_1)$, ratio of radii $R_{\max} = r_2/r_1$, thermal conductivity $\kappa(\rho) = k(\rho)/k_{UE}$, and temperature $\theta(\rho, \tau_r) = [T(\rho, \tau_r) - T_m]/(T_s - T_m)$ where $\tau_r = t/t_{r,\max}$ is the dimensionless time based upon $t_{r,\max} = \lambda r_1^2 [R_{\max}^2 \ln(R_{\max})/2 - R_{\max}^2/4 + 1/4]/[k_{UE}(T_s - T_m)]$, the total melting time for a uniform PCM/mesh composite with R_{\max} in 1-D cylindrical coordinates (see section 7.2 for the derivation of $t_{r,\max}$). The range of dimensionless radial coordinate and temperature are

exactly the same as those in 1-D Cartesian coordinates, whereas the ratio of radii $R_{\max} = r_2/r_1$ quantifies the size of the PCM and mesh in terms of the relative radii of the annulus. By doing so, we arrive at the dimensionless heat diffusion equation for 1-D cylindrical coordinates

$$\frac{1}{[\rho + 1/(R_{\max} - 1)]} \frac{\partial}{\partial \rho} \left[\left(\rho + \frac{1}{R_{\max} - 1} \right) \kappa(\rho) \frac{\partial \theta(\rho, \tau_r)}{\partial \rho} \right] = 0. \quad (2.12)$$

The dimensionless temperature distribution with boundary conditions ($\theta = 1$ at $\rho = 0$ and $\theta = 0$ at $\rho = \rho_m$) is,

$$\theta(\rho, \tau_r) = 1 - \frac{\ln(1 + \rho R_{\min}) - \ln\left(\frac{G}{H}\rho + 1\right)}{\ln(1 + \rho_m R_{\min}) - \ln\left(\frac{G}{H}\rho_m + 1\right)}. \quad (2.13)$$

where $\rho_m = \rho_m(\tau_r) = (r_m - r_1)/(r_2 - r_1)$ is time dependent melting front position and $R_{\min} = R_{\max} - 1$. The energy balance from Eq. (2.10) using all dimensionless terms in Eqs. (2.13) and (2.12) (see section 7.3 for the derivation of Eqs. (14) and (15)) is

$$\begin{aligned} & -\kappa(\rho) \frac{\partial \theta(\rho, \tau_r)}{\partial \rho} \Big|_{\rho=\rho_m(\tau_r)} \\ & = \left[\frac{(R_{\max} - 1)^2}{\frac{R_{\max}^2}{2} \ln(R_{\max}) - \frac{R_{\max}^2}{4} + \frac{1}{4}} \right] \frac{d\rho_m(\tau_r)}{d\tau_r}. \end{aligned} \quad (2.14)$$

As $R_{\max} \simeq 1$ (a thin cylindrical shell), the term in brackets approaches two, and Eq. (2.14) is the same as Eq. (2.6).

By solving Eq. (2.14) with the initial condition of $\rho_m(\tau_r = 0) = 0$, the relationship between ρ_m and τ_r is

$$\tau_r = \frac{R_{\min}}{(HR_{\min} - G) \left[\frac{R_{\max}^2}{2} \ln(R_{\max}) - \frac{R_{\max}^2 + 1}{4} \right]} \times \left[\frac{R_m^2}{2} \ln(R_{\max}) + \frac{R_m - 1}{2} - \frac{HR_{\min}}{2G} (R_m - 1) + \left(-\frac{R_m^2}{2} + \frac{H^2 R_{\min}^2}{2G^2} - \frac{HR_{\min}}{G} + \frac{1}{2} \right) \times \ln\left(\frac{G}{H} \rho_m + 1\right) \right], \quad (2.15)$$

where $R_m = r_m/r_1 = \rho_m R_{\min} + 1$. When $r_m = r_2$, then $R_m = R_{\max}$ and $\rho_m = 1$ such that the enhancement ratio from the reciprocal of Eq. (2.15) is

$$\begin{aligned} \epsilon_r(G, H, R_{\max}) &= \frac{HR_{\min} - G_{\min}}{R_{\min}} \left[\frac{R_{\max}^2}{2} \ln(R_{\max}) - \frac{R_{\max}^2}{4} + \frac{1}{4} \right] \\ &/ \left[\frac{R_{\max}^2}{2} \ln(R_{\max}) + \frac{R_{\min}}{2} - \frac{HR_{\min}^2}{2G} \right. \\ &+ \left. \left(-\frac{R_{\max}^2}{2} + \frac{H^2 R_{\min}^2}{2G^2} - \frac{HR_{\min}}{G} + \frac{1}{2} \right) \right. \\ &\left. \times \ln\left(\frac{G}{H} + 1\right) \right]. \end{aligned} \quad (2.16)$$

2.2.6. Parameterization of thermal conductivity of a binary composite

Next, we apply restrictions that equate the average volume fraction of metal mesh in the UE and SE cases. We first need to relate the thermal conductivity of the composite to the volume fraction of mesh and PCM in the composite. Analytical effective medium models for the thermal conductivity of heterogeneous or composite materials described as functions of the component materials' volume fractions and thermal conductivities were reviewed by Wang et al. [42]. To predict the effective thermal conductivity of a binary mixture like a metal/PCM composite, five basic structural models (two forms of the Maxwell-Eucken, the Effective Medium Theory, the Series, and the Parallel model) based on the constituent volume fractions were generalized [42]. Based on the structure of metal/PCM composites where the metal mesh and PCM are bi-continuous phases, the Parallel Model (i.e., the rule of mixtures) is chosen to predict the effective

thermal conductivity in a uniformly-enhanced case. This model defines $k_{\text{UE}} = k_{\text{Mesh}}v_{\text{Mesh}} + k_{\text{PCM}}(1 - v_{\text{Mesh}})$ [42] where k_{Mesh} is the thermal conductivity of the metal mesh, v_{Mesh} is the volume fraction of the metal mesh, and k_{PCM} is the thermal conductivity of the PCM. As previously noted, a modified rule of mixtures based on the structure and volume fraction of graphite foams accurately predicted the thermal conductivity of UGF-erythritol composite [89].

Within the Parallel model, we modify v_{Mesh} to be a function of position $v'_{\text{Mesh}}(z)$ and $v'_{\text{Mesh}}(r)$. For 1-D Cartesian coordinates, $k(z) = k_{\text{Mesh}}v'_{\text{Mesh}}(z) + k_{\text{PCM}}[1 - v'_{\text{Mesh}}(z)]$. To create a fair comparison the average volume fraction of the metal mesh in the spatially-enhanced case is equated to that in the uniform case $v_{\text{Mesh}} = \bar{v}'_{\text{Mesh}}(z) = \int_0^d dz v'_{\text{Mesh}}(z)/d$. Under this constraint, $A = 2(1 - B)$, which makes the dimensionless thermal conductivity from Eq. (2.3) a function of only B

$$\kappa(\zeta) = 2(1 - B)\zeta + B, \quad (2.17)$$

Therefore, the enhancement ratio ϵ_z in Eq. (2.8) takes the form

$$\epsilon_z(B) = \frac{(1 - B)}{\left[\ln \left(\frac{2(1 - B)}{B} + 1 \right) \left(1 + \frac{B}{2(1 - B)} \right) - 1 \right]}. \quad (2.18)$$

Because κ is linear in ζ , the minimum $\kappa = k_{\text{PCM}}/k_{\text{UE}} = [v_{\text{Mesh}}(k_{\text{Mesh}}/k_{\text{PCM}} - 1) + 1]^{-1}$ occurs either at $\zeta = 0$ or at $\zeta = 1$, and the range of the intercept B is

$$[v_{\text{Mesh}}(k_{\text{Mesh}}/k_{\text{PCM}} - 1) + 1]^{-1} < B < 2 - [v_{\text{Mesh}}(k_{\text{Mesh}}/k_{\text{PCM}} - 1) + 1]^{-1}, \quad (2.19)$$

As $k_{\text{PCM}}/k_{\text{Mesh}}$ approaches zero, the range of the intercept B is $0 < B < 2$.

For a 1-D cylindrical coordinates, the spatially-enhanced thermal conductivity is written as $k(r) = k_{\text{Mesh}}v'_{\text{Mesh}}(r) + k_{\text{PCM}}[1 - v'_{\text{Mesh}}(r)]$. Equating the average volume fraction, $v_{\text{Mesh}} = \bar{v}'_{\text{Mesh}}(r) = \int_{r_1}^{r_2} 2\pi r dr v'_{\text{Mesh}}(r) / (\pi r_2^2 - \pi r_1^2)$, results in $G = [3(1 - H)(R_{\text{max}} + 1)R_{\text{min}}^2] /$

$(2R_{\max}^3 - 3R_{\max}^2 + 1)$ in Eq. (2.11). Here, the dimensionless thermal conductivity as a function of H and R_{\max} is

$$\kappa(\rho) = \frac{3(1-H)(R_{\max}+1)R_{\min}^2}{2R_{\max}^3 - 3R_{\max}^2 + 1} \rho + H. \quad (2.20)$$

Thus, the enhancement ratio in Eq. (2.16) can be parameterized as

$$\begin{aligned} \epsilon_r(H, R_{\max}) = & \left[H - \frac{3(1-H)\epsilon_{R2}}{\epsilon_{R3}} \right] \left[\frac{R_{\max}^2}{2} \ln(R_{\max}) - \frac{R_{\max}^2}{4} + \frac{1}{4} \right] \\ & / \left\{ \frac{R_{\max}^2}{2} \ln(R_{\max}) + \frac{R_{\min}}{2} - \frac{H\epsilon_{R3}}{6(1-H)(R_{\max}+1)} \right. \\ & + \left(\frac{1-R_{\max}^2}{2} \right) \ln \left[\frac{3(1-H)(R_{\max}+1)R_{\min}^2}{H\epsilon_{R3}} \right. \\ & \left. \left. + 1 \right] + \left[\frac{H^2\epsilon_{R3}^2}{18(1-H)\epsilon_{R2}^2} - \frac{H\epsilon_{R3}}{3(1-H)\epsilon_{R2}} \right] \right. \\ & \left. \times \ln \left[\frac{3(1-H)(R_{\max}+1)R_{\min}^2}{H\epsilon_{R3}} + 1 \right] \right\}, \quad (2.21) \end{aligned}$$

where $\epsilon_{R2} = R_{\max}^2 - 1$ and $\epsilon_{R3} = 2R_{\max}^3 - 3R_{\max}^2 + 1$. The range of the intercept H is

$$\begin{aligned} \frac{1}{v_{\text{Mesh}}(k_{\text{Mesh}}/k_{\text{PCM}} - 1) + 1} & < H \\ & < \frac{3R_{\max}^3 - 3R_{\max}^2 - 3R_{\max} + 3}{R_{\max}^3 - 3R_{\max} + 2} \\ & - \frac{\epsilon_{R3}}{\left[v_{\text{Mesh}} \left(\frac{k_{\text{Mesh}}}{k_{\text{PCM}}} - 1 \right) + 1 \right] (R_{\max}^3 - 3R_{\max} + 2)}. \quad (2.22) \end{aligned}$$

This range becomes $0 < H < 3$ when $k_{\text{PCM}}/k_{\text{Mesh}} \simeq 0$ and $1/R_{\max} \simeq 0$.

2.3. Results and discussion

The solutions from Eqs. (2.18) and (2.21) are used to calculate the spatial distribution of k that optimizes the average charge rate of the PCM composite.

2.3.1. Spatial dependence of the melting front

For 1-D Cartesian coordinates, the melting front positions as a function of time for three different values of B are shown in Figure 2.4. The corresponding distributions of κ are shown in the inset of Figure 2.4. With $B \simeq 0$ the melting front progresses much slower than for $B = 1$ (k_{UE}). Notably the solution from [131] with $n = 1$ is limited to this $B \simeq 0$ scenario. Alternatively, with $B = 1.63$ the melting front reaches $\zeta_m = 1$ approximately 10% faster than with $B = 1$ ($B = 1$ represents the uniformly-enhanced case). Notably the melting front with $B = 1.63$ arrives at $\zeta_m = 0.5$ (half melted) 35% faster than the uniformly-enhanced case. Hence, by enhancing the thermal conductivity near to the heat source ($\zeta = 0$), the time averaged thermal resistance to get heat to the melting front is reduced, and the PCM can be charged/discharged faster.

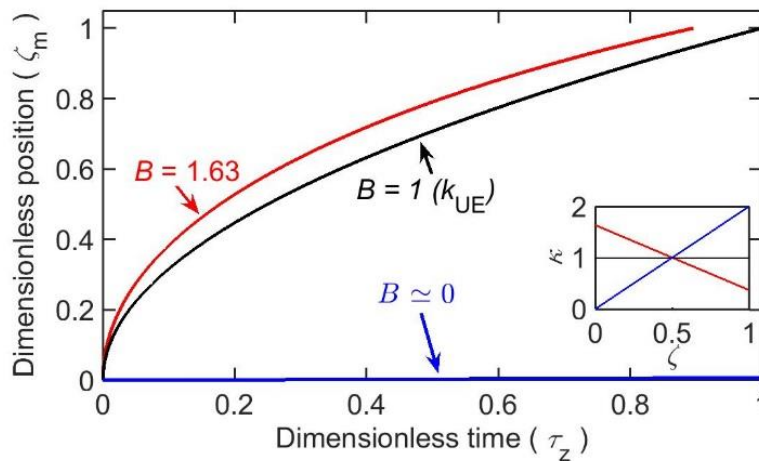


Figure 2.4 The melting front progresses differently with various intercepts B . The faster melting process with $B = 1.63$ indicates higher average charge rate. The corresponding distributions of spatially-enhanced thermal conductivity are shown in the inset where the heat source is at $\zeta = 0$.

2.3.2. Optimization of mesh design

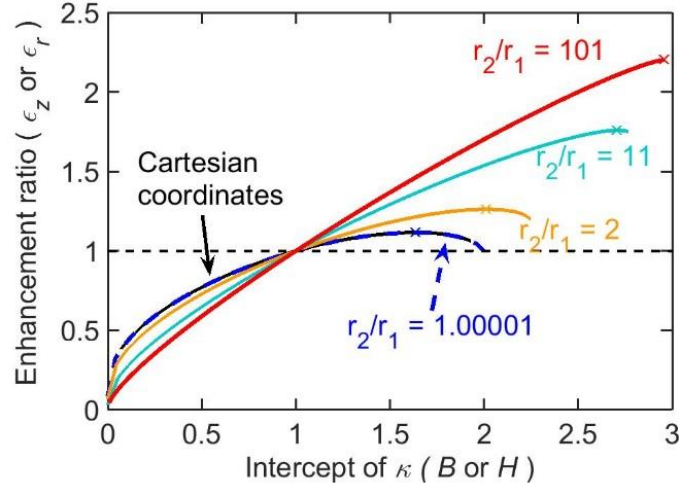


Figure 2.5 The enhancement ratio is a function of B in 1-D Cartesian coordinates (Eq. (2.18)) and H in 1-D cylindrical coordinates for several values of r_2/r_1 (Eq. (2.21)). The enhancement ratio in cylindrical coordinates with $r_2/r_1 = 1.00001$ is identical to that in a 1-D Cartesian coordinates. At high radius ratios spatial enhancement can improve the average charge rate over that of uniform enhancement by more than 100%.

The enhancement ratio ϵ_z is shown in Figure 2.5 as a function of B for 1-D Cartesian coordinates. We see that ϵ_z is enhanced between $B = 1$ and $B = 2$ ($\epsilon_z > 1$), whereas, below $B = 1$, the average heat transfer rate is worse than that with k_{UE} ($\epsilon_z < 1$). These results can be used as a guide to design $k(z)$ that outperforms the uniformly-enhanced case.

The maximum ϵ_z occurs when the derivative $d\epsilon_z(B)/dB = 0$ because the enhancement ratio as a function of B , shown in Figure 2.5, is a concave-down curve. Figure 2.5 indicates that $B = 1.64$ is optimal and increases the charge rate over that of k_{UE} by 11.6% ($\epsilon_{z,opt} = 1.116$).

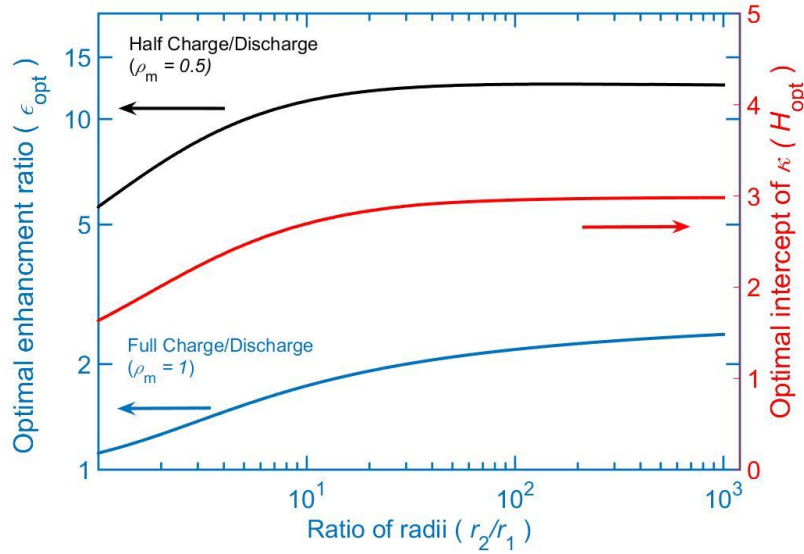


Figure 2.6 The optimal enhancement ratio $\epsilon_{r,opt}$ and optimal intercept H_{opt} as a function of the radius ratio r_2/r_1 at $\rho_m = 0.5$ and 1. When the melting process is complete ($\rho_m = 1$), the enhancement ratio ascends rapidly for $1 < r_2/r_1 < 10$, then it gradually grows to 2.4 as $r_2/r_1 = 1000$. When the melting process is incomplete ($\rho_m = 0.5$), even higher enhancement takes place.

Similarly, the enhancement ratio in 1-D cylindrical coordinates is shown in Figure 2.5. The enhancement ratio ϵ_r in a cylindrical system varies with the radii ratio r_2/r_1 as well as the intercept H . First, we plot ϵ_r with $r_2/r_1 = 1.00001$ where the enhancement ratio is similar to that in 1-D Cartesian coordinates. This result confirms that the melting process in a thin cylindrical shell is approximated by the 1-D Cartesian coordinates solution. We further increase r_2/r_1 from 2 to 101 and plot ϵ_r in Figure 2.5. The upper limit of H approaches 3 and ϵ_r increases above 2 as r_2/r_1 increases. The crosses in Figure 2.5 indicate the optimal enhancement ratio for each r_2/r_1 .

The optimal enhancement ratio $\epsilon_{r,opt}$ and the corresponding intercept H_{opt} are shown in Figure 2.6 as a function of r_2/r_1 . As $r_2/r_1 \approx 1000$ $\epsilon_{r,opt}$ approaches 2.4. More extreme enhancements can be achieved in cylindrical coordinates because in a homogeneous solid cylindrical annulus the derivative of thermal resistance, which represents the thermal resistance per unit cylindrical shell thickness, is highest at $r = r_1$ (i.e., thermal resistance accumulates most

rapidly when the melt front is near $r = r_1$). As a result, spatial enhancement of thermal conductivity near the heat source at r_1 drastically reduces the time averaged thermal resistance during the charge/discharge process. It is remarkable that simply redistributing the mesh, while conserving its average volume fraction, results in enhancements to the charge/discharge rates exceeding 100% in the radial geometry system. Moreover, if the same meshes undergo an incomplete melting process such that $\rho_m = 0.5$, the average charge rate is enhanced even more than that of a complete melting processes ($\rho_m = 1$), as shown in Figure 2.6.

2.4. Summary

We show that a spatially-enhanced thermal conductivity can enhance the charge/discharge rate in PCM/mesh composites in both 1-D Cartesian and 1-D cylindrical coordinate systems. Our spatially-enhanced thermal conductivity uniquely incorporates a linear distribution with separately adjustable slope and intercept. Through nondimensionalizing the equations, we acquire and define the enhancement ratio of the average charge/discharge rates to that of the uniformly-enhanced case while conserving the average volume fraction of the metal mesh. We find that enhancing the thermal conductivity near the heat source effectively reduces the average thermal resistance throughout the phase change process, and thus improves the average charge rate by more than 100% in select cylindrical systems. Among other applications, these enhanced charge/discharge rates will benefit thermal management in small dynamic systems and temperature regulation in buildings by PCMs. Likewise, equivalent performance can be achieved with less metal, which is appealing for applications that demand lightweight alternatives (e.g., a Cu mesh of volume fraction 0.1 nearly doubles the weight of a wax PCM). Progress in advanced fabrication techniques such as additive manufacturing offers hope that complex metal meshes with spatially-varied thermal

conductivity are a near-term reality [122, 123]. Our work provides a critical guide for the design of such spatially-varied metal meshes.

3. Hot spot thermal management by phase change materials enhanced by graded metal meshes

This chapter is in preparation for submission to *Applied Thermal Engineering*.

3.1. Overview

The computational performance of electronic devices, such as laptop computers and cellular phones, continues to improve while they continue to get smaller [13, 14, 43, 54]. High computational performance demands large power consumption. The result is increased energy density, which challenges conventional thermal management strategies [14, 46, 54]. Both active (e.g., fan-blown air, thermoelectric coolers) and passive (e.g., heat sinks, heat pipes) cooling techniques have been widely investigated [14, 133-135].

Passive thermal management consumes less power and is more reliable than active thermal management with fans and pumps [54]. Therefore, for small devices such as cellular phones and tablets, passive thermal management is more desirable. Nevertheless, passive thermal management has limitations. For instance, capillary or gravity-driven heat pipes are only operable when the device is in specific configurations, and passive heat sinks rely on natural convection with low heat transfer coefficients.

Phase change materials (PCMs) are an attractive alternative to heat pipes and heat sinks that have been studied for the purpose of maintaining the exterior temperature of devices within a comfortable range to users (e.g., $< 60^{\circ}\text{C}$) and absorbing transient spikes in the heat load [44, 46, 51-54, 136-139]. The transient temperature rise is affected by the composition of PCM, the configuration of the thermal management systems, and the size and heat load of the hot spots [44, 46, 54]. PCMs, such as octadecane and eicosane, are commonly selected due to their phase change

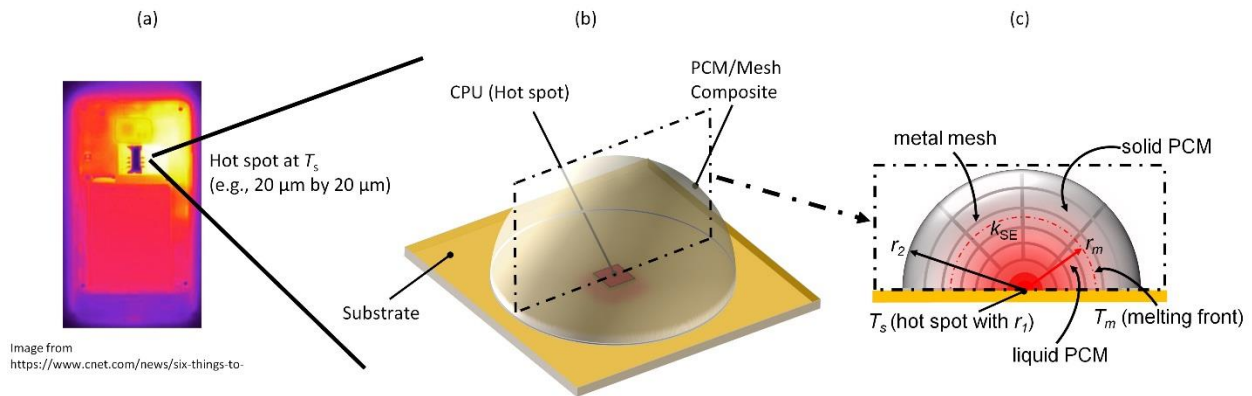
temperatures (30°C to 40°C), which maintain a comfortable device temperature for the users [46, 54]. Nevertheless, due to low thermal conductivity of such PCMs, heat from hot spots may diffuse in unintended directions instead of directly into PCMs (i.e., the thermal resistance of PCMs is higher than the other parts surrounding the hot spots.). To mitigate this effect, heat sinks have been embedded into PCMs to minimize thermal resistance [44]. Yet, these extended parts displace the latent heat benefit of PCMs and result in noticeable weight and volume on smaller devices.

An alternative way to increase heat dissipation rates of PCMs is through the addition of low volume fraction, high thermal conductivity, porous materials. The effective thermal conductivity of PCMs can be enhanced by incorporating either dispersed fillers [15, 87, 89, 90, 117, 118] or high thermal conductivity porous structures (e.g., metal foams or meshes) [36, 89, 92, 93, 120]. Because both fillers and porous structures are spatially homogeneous, the thermal conductivity of the PCMs is uniformly-enhanced (UE).

Recent advancements in additive manufacturing provide a feasible way to fabricate complex metal architectures, such as lattices and graded meshes. With these AM graded meshes in PCMs, the metal volume fraction can be spatially-varied, and thus the thermal conductivity becomes spatially-enhanced (SE) [97-99, 140]. With SE meshes it is possible to concentrate the enhancement near to the heat source, thus minimizing the thermal resistance for heat to reach the melt front [97]. For equivalent average volume fractions of mesh, a linear spatial variation can improve the heat dissipation rates by 12% in planar and 140% in cylindrical configurations [97]. Spatially-enhanced diffusivities with other mathematical forms, such as power law functions, have been studied for mathematically similar sedimentary mass transport applications [95-97, 124, 127-129, 131]. Also, while prior studies focused on Cartesian and cylindrical coordinates, none have

considered spatially-heterogeneous thermal conductivity on moving boundary problems in spherical coordinates.

To improve upon state of the art PCM based thermal management designs, we herein utilize a generalized polynomial function to determine the optimal radial thermal conductivity distribution in spherical PCM/mesh systems. Furthermore, we for the first time apply the concept of spatial enhancement to spherical coordinates. Furthermore, we for the first time apply the concept of spatial enhancement to spherical coordinates.



*For the hot spot to be seen clearly, the mesh structure is only shown in the cross-section view.

Figure 3.1 Schematic of a hemi-spherical PCM/Mesh composite for thermal management. (a) A processor (i.e., chip) on a mobile phone creates a localized hot spot (e.g., the hot spot size is in the tens of micrometers [59]). (b) The heat dissipation from the hot spot is absorbed by the PCM/Mesh composite. (c) The cross-sectional view of the hemi-spherical PCM/Mesh composite depicts a spatial variation in volume fraction of metal mesh, which results in spatially-enhanced thermal conductivity $k(r)$.

3.2. Methodology

3.2.1. The Stefan problem in Cartesian coordinates

Hot spots drive radial temperature gradients in the surrounding medium, and thus the radial direction is considered in the spherical heat diffusion equation [82]. A Stefan problem can be solved using the quasi-steady state approximation where the Stefan number $Ste < 0.1$ [95, 97]. A small Stefan number indicates that the sensible heat is small compared to the latent [95].

The quasi-steady state approximation implies that as the melting process progresses, thermal transport from the hot spot to the melting front propagates rapidly compared to the melting velocity and a steady state temperature distribution is reached instantaneously [95]. The heat diffusion equation under the quasi-steady state approximation in a one-dimensional spherical system is

$$\frac{1}{r^2} \frac{\partial}{\partial r} \left[r^2 k(r) \frac{\partial T(r, t)}{\partial r} \right] = 0, \quad (3.1)$$

where r is the radial coordinate, $k(r)$ is the spatially-varied thermal conductivity of a PCM/mesh composite, $T(r, t)$ is the temperature of the composite, and t is time. Schematics of PCM/Mesh composites with spatially-enhanced thermal conductivity $k_{SE} = k(r)$ are shown in Figure 3.1. The hot-spot at a temperature $T(r_1, t) = T_s$ is surrounded by a spherical PCM/Mesh shell with inner and outer radii r_1 and r_2 . The time dependent position of the melting front at a melting temperature $T(r_m, t) = T_m$ from the hot spot (or heat source) is $r_m(t)$.

With constant temperature boundary conditions of $T(r_1, t) = T_s$ and $T(r_m, t) = T_m$, the temperature of the composite for $r_1 < r < r_m$ can be determined. The temperature in the solid PCM (for a melt process) is assumed to be at T_m , so no sensible heat is required [95, 97].

The energy balance at the melting front is

$$-k(r) \frac{\partial T(r, t)}{\partial r} \Big|_{r=r_m(t)} = \lambda \frac{dr_m(t)}{dt}. \quad (3.2)$$

For small mesh volume fractions, the latent heat of fusion λ is assumed to be independent of r [97].

Our analysis of the spatially enhanced PCM is nondimensionalized to the uniformly-enhanced PCM. By nondimensionalizing the coordinate $\rho_{\text{sp}} = (r - r_1)/(r_2 - r_1)$, the dimensionless thermal conductivity is defined as $\kappa(\rho_{\text{sp}}) = k(\rho_{\text{sp}})/k_{\text{UE}}$ and formulated as a polynomial

$$\begin{aligned} k(\rho_{\text{sp}}) &= C_n \rho_{\text{sp}}^n + C_{n-1} \rho_{\text{sp}}^{n-1} + \dots + C_1 \rho_{\text{sp}} + C_0 \\ &= \sum_{i=0}^{i=n} C_i \rho_{\text{sp}}^i, \end{aligned} \quad (3.3)$$

where C_i are the adjustable coefficients of the i^{th} degree terms that will be optimized. Although mathematical forms of dimensionless thermal diffusivity or thermal conductivity, such as power law and linear functions, were previously introduced [97, 128, 129, 131], our polynomial form provides added degrees of freedom to generate complex spatial-variations of thermal conductivity.

3.2.2. Nondimensionalized solution for a spatially-enhanced thermal conductivity in

1-D spherical coordinates

We nondimensionalize Eq. (3.1) by substituting ρ_{sp} , $\kappa(\rho_{\text{sp}})$, the ratio of bounding radii $R_{\text{max}} = r_2/r_1$, and dimensionless temperature $\theta(\rho_{\text{sp}}, \tau_{\text{sp}}) = [T(\rho_{\text{sp}}, \tau_{\text{sp}}) - T_m]/(T_s - T_m)$. The dimensionless time $\tau_{\text{sp}} = t/t_{\text{sp,max}}$ is defined based upon the time required to melt all of the PCM in the case of uniformly-enhanced thermal conductivity $t_{\text{sp,max}} = \lambda r_1^2 (2R_{\text{max}}^3 - 3R_{\text{max}}^2 + 1)/[6k_{\text{UE}}(T_s - T_m)]$ (see section 7.4 for the derivation of $t_{\text{sp,max}}$). The resulting nondimensionalized radial heat diffusion equation is,

$$\frac{1}{(1 + \rho_{\text{sp}} R_{\text{min}})^2} \frac{\partial}{\partial \rho_{\text{sp}}} \left[(1 + \rho_{\text{sp}} R_{\text{min}})^2 \kappa(\rho_{\text{sp}}) \frac{\partial \theta(\rho_{\text{sp}}, \tau_{\text{sp}})}{\partial \rho_{\text{sp}}} \right] = 0. \quad (3.4)$$

where $R_{\text{min}} = R_{\text{max}} - 1$.

The energy balance from Eq. (3.2) is normalized using the same dimensionless parameters

$$\begin{aligned} -\kappa(\rho_{\text{sp}}) \frac{\partial \theta(\rho_{\text{sp}}, \tau_{\text{sp}})}{\partial \rho_{\text{sp}}} \Big|_{\rho_{\text{sp}} = \rho_{\text{sp},m}(\tau_{\text{sp}})} \\ = \left(\frac{6R_{\text{min}}^2}{2R_{\text{max}}^3 - 3R_{\text{max}}^2 + 1} \right) \frac{d\rho_{\text{sp},m}(\tau_{\text{sp}})}{d\tau_{\text{sp}}}, \end{aligned} \quad (3.5)$$

where $\rho_{\text{sp},m}(\tau_{\text{sp}})$ is the dimensionless melting front position in spherical coordinates. As $R_{\text{max}} \approx 1$, the term in brackets of Eq. (3.5) approaches 2 and is the same as Eq. (2.6) from Ref. [97] for 1-D Cartesian coordinates, indicating that a thin spherical shell ($r_2 - r_1 \ll r_1$) behaves like a planar solid.

An analytical solution to Eq. after substitution of $\kappa(\rho_{\text{sp}})$ from Eq. (3.3), does not exist. Thus, $\rho_{\text{sp},m}$ is numerically solved from Eqs. (3.4) and (3.5). The numerical details are in section 7.5.

Regardless of $\kappa(\rho_{\text{sp}})$ the maximum of $\rho_{\text{sp},m}$ is 1, and $\tau_{\text{sp}}(\rho_{\text{sp},m} = 1) = \tau_{\text{sp},\text{max}}$. Because the same volume of PCM is melted, $\tau_{\text{sp},\text{max}} < 1$ signifies that the SE thermal conductivity distribution dissipates heat faster than the UE thermal conductivity distribution. The reciprocal of $\tau_{\text{sp},\text{max}}$ is defined as the enhancement ratio of SE to UE for heat dissipation in SE PCM composites,

$$\epsilon_{\text{sp}} = \frac{1}{\tau_{\text{sp},\text{max}}}. \quad (3.6)$$

3.2.3. Parameterization of thermal conductivity in a polynomial form

Constraints that equate the average volume fraction of metal mesh in UE and SE cases are first applied to constrain the form of $\kappa(\rho_{\text{sp}})$. The local volume fraction and thermal conductivity are related by an effective medium model. Because the metal mesh and PCM are bi-continuous phases, the Parallel Model is appropriate [42, 97], and $k_{\text{SE}}(r) = k_{\text{Mesh}}v'_{\text{Mesh}}(r) + k_{\text{PCM}}[1 - v'_{\text{Mesh}}(r)]$. From Ref. [97], the dimensionless thermal conductivity ($\kappa = k_{\text{SE}}/k_{\text{UE}}$) is described as

$$\kappa = \frac{k_{\text{PCM}} + \Delta k v'_{\text{Mesh}}(r)}{k_{\text{UE}}}, \quad (3.7)$$

where k_{PCM} is the thermal conductivity of the PCM, $\Delta k = k_{\text{Mesh}} - k_{\text{PCM}}$ is the thermal conductivity difference, and k_{Mesh} is the thermal conductivity of the metal mesh.

The average volume fractions for the SE and UE distributions are equated so that $\bar{v}'_{\text{Mesh}}(r) = \int_{r_1}^{r_2} 4\pi r^2 v'_{\text{Mesh}}(r) dr / [4\pi(r_2^3 - r_1^3)/3] = v_{\text{Mesh}}$. With this constraint $v'_{\text{Mesh}}(r)$ and the form of $\kappa(\rho_{\text{sp}})$ based on Eq. (3.3) the coefficients C_i are related as

$$\sum_{i=0}^{i=n} C_{\text{cv},i} C_i = 1, \quad (3.8)$$

where $C_{\text{cv},i}$ (see the detailed derivation in section 7.6) take the form

$$C_{\text{cv},i} = \left[\frac{(R_{\text{max}} - 1)^2}{i + 3} + \frac{2(R_{\text{max}} - 1)}{i + 2} + \frac{1}{i + 1} \right] \frac{3(R_{\text{max}} - 1)}{R_{\text{max}}^3 - 1}. \quad (3.9)$$

The coefficients C_i are also constrained such that $v'_{\text{Mesh}}(r) > 0$ so that at a minimum, no metal mesh is present. This also implies that the dimensionless thermal conductivity at that position is $\kappa(\rho_{\text{sp}}) = k_{\text{PCM}}/k_{\text{UE}}$.

Furthermore, if $v'_{\text{Mesh}}(r)$ is less than 0.2 (i.e., $v'_{\text{Mesh}}(\rho_{\text{sp}})$), it is reasonable to assume that the latent heat of the PCM/Mesh composite is the same as pure PCM with no spatial variation [97]. Therefore, we limit our study to $v'_{\text{Mesh}}(\rho_{\text{sp}}) < 0.2$.

Table 3.1 Properties and parameters of $\kappa(\rho_{\text{sp}})$

PCM/Mesh	k_{PCM} (W/m-K)	k_{Mesh} (W/m-K)	\bar{v}'_{Mesh}	k_{UE} (W/m-K)	κ_{min}	κ_{max}
Octadecane/Al mesh	0.15	237	0.02	4.89	0.03	9.72

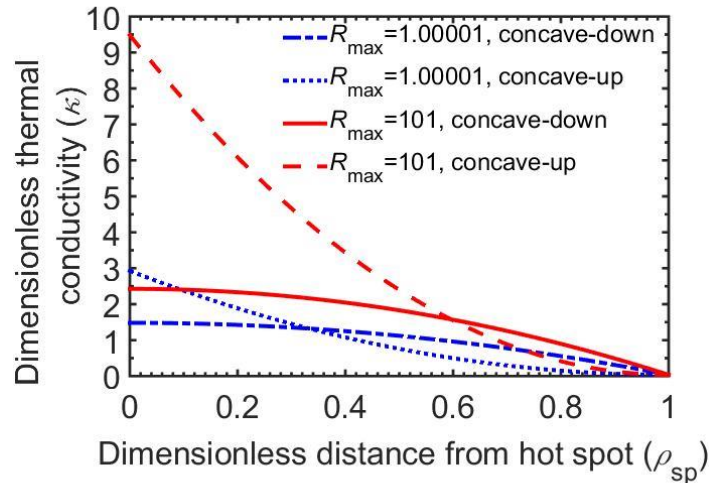


Figure 3.2 The combinations of spatial variation of $\kappa(\rho_{\text{sp}})$ of degree $n = 2$ in Eq. (3.3) are constrained by the conservation of volume fraction and limitations on the minimum/maximum of $\kappa(\rho_{\text{sp}})$ (i.e., κ_{min} and κ_{max}) listed in Table 3.1. The concave-up $\kappa(\rho_{\text{sp}})$ provides a higher thermal conductivity near the hot spot.

In Figure 3.2, we show four combinations of $\kappa(\rho_{\text{sp}})$ polynomial of degree $n = 2$ in Eq. (3.3) using properties and parameters listed in Table 3.1. Near to the hot spot ($\rho_{\text{sp}} \approx 0$) with $R_{\text{max}} =$

101 is higher than κ with $R_{\max} = 1.00001$, because the high v'_{Mesh} is compensated by low v'_{Mesh} of spherical shells at more distant radii.

To maximize the intercept of Eq. (3.3), the minimum of κ (i.e., $k_{\text{PCM}}/k_{\text{UE}}$) is chosen to be at $\rho_{\text{sp}} = 1$ under the constraint of Eq. (3.8). Furthermore, for the same R_{\max} , Eq. (3.3) can generate parabolic κ with both concave-up and concave-down shapes as shown in Figure 3.2. The concave-up shapes have vertices at $\rho_{\text{sp}} = 1$, while the concave-down shapes have vertices at $\rho_{\text{sp}} = 0$. The concave-up κ place more enhancement near to the heat source. For instance, with $R_{\max} = 1.00001$ as shown in Figure 3.2, the concave-up κ is twice the concave-down κ at $\rho_{\text{sp}} = 0$. The difference is even more extreme with $R_{\max} = 101$ where the concave-up case ($\kappa \approx 9.5$) is 280% higher than the concave-down case ($\kappa \approx 2.5$) at $\rho_{\text{sp}} = 0$. This clarifies that the concave-up shape results in higher enhancement of thermal conductivity near to the hot spot in large spherical systems.

3.3. Results and discussion

We first consider κ defined by a second order polynomial ($n = 2$). This parabolic form provides more complexity than linear κ , and allows us to examine the interplay between enhancement of κ at $\rho_{\text{sp}} = 0$, concavity of κ , and the ratio of radii R_{\max} . For this comparison, we use the parameters listed in Table 3.1 with three different vertices at $\rho_{\text{sp}} = 0, 0.5$, and 1.

3.3.1. Effects of enhancement near the heat source ($\rho_{\text{sp}} = 0$)

Figure 3.3 shows the dimensionless distance of the melting front from the hot spot, as a function of time for $r_2/r_1 = 101$. For concave-up $\kappa(\rho_{\text{sp}})$, $\tau_{\text{sp,max}} = 0.12$ is faster than concave-down and uniformly-enhanced cases with $\tau_{\text{sp,max}} = 0.41$ and $\tau_{\text{sp,max}} = 1$, respectively. The faster melting process implies a higher enhancement ratio [97]. In this spherical system, $\epsilon_{\text{sp}} = 8.2$ using

the concave-up $\kappa(\rho_{sp})$ is 240% better than the concave-down $\kappa(\rho_{sp})$. This result confirms that higher enhancement at $\rho_{sp} = 0$ expedites the melting process and thus enhances the heat dissipation rates of PCMs in spherical systems as was shown previously in Cartesian and cylindrical systems from Ref. [97].

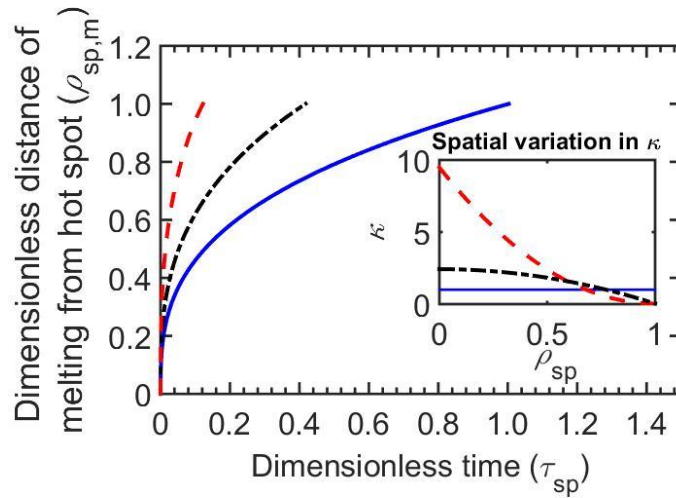


Figure 3.3 The higher spatially-enhanced thermal conductivity near to the hot spot (i.e., the intercept of $\kappa(\rho_{sp})$) with $r_2/r_1 = 101$ expedites the melting front ending at $\tau_{sp} = 0.12$, and, in other words, increases the heat dissipation rate relative to UE by more than eight times.

3.3.2. Effects by concavity of κ

As shown in Fig. 4, the maximum enhancement ratio with concave-up $\kappa(\rho_{sp})$ with κ_{min} at $\rho_{sp} = 1$ reaches 8.2. The $\kappa(\rho_{sp})$ associated with the three crosses are shown in the inset. While $\epsilon_{sp} > 1$ are found in each case, the concave-up $\kappa(\rho_{sp})$ with κ_{min} at $\rho_{sp} = 1$ most significantly amplifies the enhancement ratio.

Given the performance benefits of a concave-up $\kappa(\rho_{sp})$, we further constrain the form of Eq. (3.3) so that $\kappa(\rho_{sp})$ is always concave-up, as

$$\kappa(\rho_{sp}) = \Delta\kappa(1 - \rho_{sp})^n + \kappa_{min}, \quad (3.10)$$

where $\Delta\kappa$ is the dimensionless thermal conductivity difference between $\rho_{sp} = 0$ and $\rho_{sp} = 1$. By equating Eqs. (3.7) and (3.10), we solve for $v'_{Mesh} \cdot v'_{Mesh} = [\Delta\kappa(1 - \rho_{sp})^n + (\kappa_{min} - k_{PCM}/k_{UE})]k_{UE}/\Delta\kappa$ is substituted into Eq. (7.7.1) to enforce volume fraction conservation. As a result, $\Delta\kappa$ is

$$\Delta\kappa = \frac{1 - \kappa_{min}}{\frac{3(R_{max} - 1)}{R_{max}^3 - 1} \left[\frac{(R_{max} - 1)^2}{n + 3} + \frac{2(R_{max} - 1)R_{max}}{n + 2} + \frac{R_{max}^2}{n + 1} \right]}, \quad (3.11)$$

where $\Delta\kappa$ is always positive because the range of κ_{min} is always between k_{PCM}/k_{UE} and 1. Therefore, $1 - \kappa_{min} \geq 0$. For the uniformly-enhanced κ , $n = 0$ and $\Delta\kappa = 1 - \kappa_{min}$ from Eq. (3.11) make such that $\kappa(\rho_{sp}) = 1$ from Eq. (3.10).

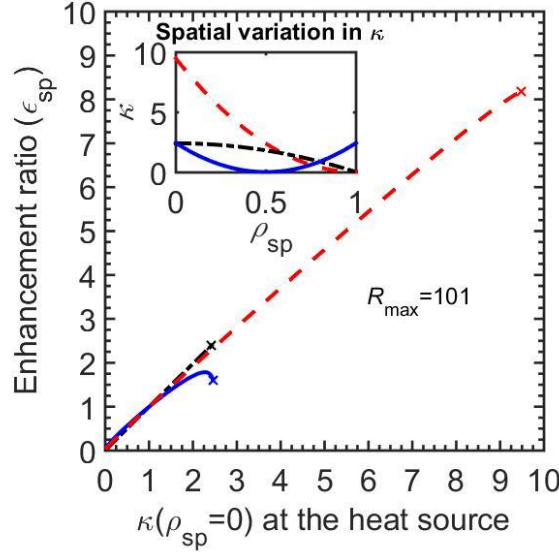


Figure 3.4 For cases with vertices at $\rho_{sp} = 1$, the maximum of enhancement ratio ($\epsilon_{sp} = 8.2$) to the heat dissipation rates with $R_{max} = 101$ in (b) is 95% higher than that ($\epsilon_{sp} = 4.2$) with $R_{max} = 11$ in (a). Vertices at $\rho_{sp} = 1$ with intercepts of κ larger than one (e.g., higher thermal conductivity near hotspot) result in concave-up $\kappa(\rho_{sp})$ and thus higher enhancement ratio than those at $\rho_{sp} = 0$ and 0.5 with both $R_{max} = 11$ and 101.

Concave-up shapes are preserved by Eq. (3.10) even with $n > 2$ because the second derivative of Eq. (3.10) is always positive for $0 \leq \rho_{sp} \leq 1$. For the same κ_{\min} in Eq. (3.10), higher order n result in larger $\Delta\kappa$ and thus higher intercepts of $\kappa(\rho_{sp})$. Nevertheless, the highest $\kappa(\rho_{sp})$ for each n is herein constrained by κ_{\max} where $v'_{\text{Mesh}}(\rho_{sp}) = 0.2$, as not to replace too much PCM with mesh, per the discussion in section 3.2.3.

The enhancement ratio using Eq. (3.10) is shown in Figure 3.5 and indicates that heat dissipation rates are not further enhanced with $n > 3$ for $R_{\max} = 101$. This results due to the constraints on κ_{\min} and κ_{\max} , which limit the utility of higher degree polynomials. Nevertheless, an important conclusion is that there are significant gains by moving beyond simple linear distributions of thermal conductivity (i.e., $n = 1$).

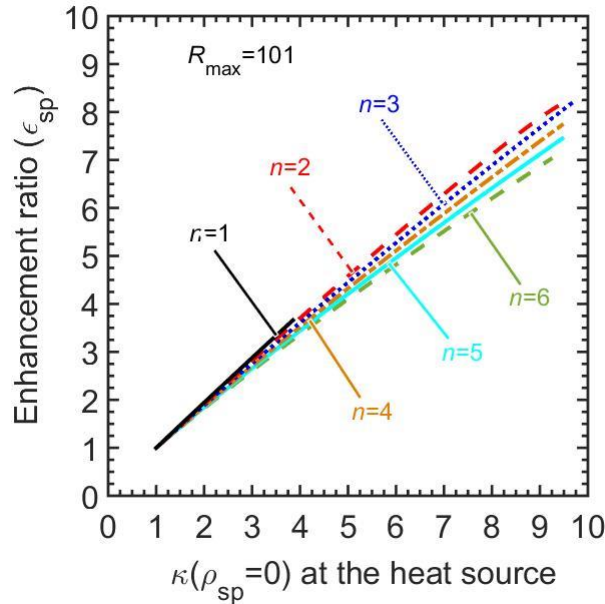


Figure 3.5 The enhancement ratio using Eq. (3.10) indicates that complex concave-up $\kappa(\rho_{sp})$ with degree higher than 1 (i.e., $n > 1$) enhance heat dissipation rates by nearly 700%.

3.3.3. Effects by ratio of radii

In Figure 3.6 we show the enhancement ratio versus r_2/r_1 in spherical and cylindrical coordinates for $n = 1, 2$, and 3. The equations for the cylindrical cases generalized the derivation for linear distributions from Ref. [97] and are shown in section 7.7. The enhancement ratio reaches 9.4 (more than 800%) with $n = 3$ in spherical systems with $R_{\max} \approx 1000$. For the cylindrical systems with similarly large R_{\max} , the enhancement ratios are more than 3 (more than 200%) for $n = 2$ and close to 4 ($\approx 300\%$). The enhancement ratios for spherical and cylindrical systems increase similarly with $n = 2$ and 3, and exceed those of $n = 1$ for $r_2/r_1 > 10$. Those monotonically increasing curves result imply that higher heat dissipation rates can be achieved for hot spots of smaller r_1 , with the same size of PCM/mesh composites (i.e., r_2).

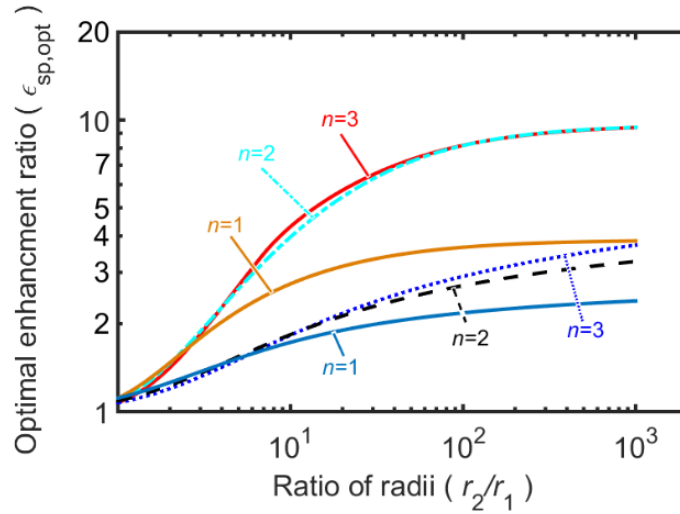


Figure 3.6 The optimal enhancement ratio as a function of the ratio of radii in cylindrical (Cyl) and spherical (Sp) systems. The optimal enhancement ratio ($\epsilon_{sp,opt}$) reaches nearly 10 for $n = 2$ and 3 in spherical systems with $r_2/r_1 = 1000$. For the cylindrical systems with similarly large R_{\max} , the enhancement ratios ($\epsilon_{r,opt}$) are more than 3 (more than 200%) for $n = 2$ and close to 4 ($\approx 300\%$). In both cylindrical and spherical systems, the enhancement to thermal transport in cases of $n = 2$ and 3 is distinctively higher than that of $n = 1$ (i.e., spatially-linear $\kappa(\rho_{sp})$).

More extreme enhancements can be achieved in spherical coordinates because in a homogeneous solid sphere the derivative of thermal resistance, which represents the thermal resistance per unit spherical shell thickness, is highest at $r = r_1$ (i.e., thermal resistance accumulates most rapidly when the melt front is near $r = r_1$). Mathematically, the derivatives of thermal resistance are proportional to $1/r^2$ and $1/r$ respectively for spherical and cylindrical systems. As r is near to r_1 , the higher derivatives of thermal resistance represent rapid thermal resistance accumulations. Therefore, spatial enhancement of thermal conductivity near the heat source at $r = r_1$ drastically reduces the time averaged thermal resistance. Remarkably, spherical geometries with SE thermal conductivity, $\epsilon_{sp,opt}$ can reach more than 800%.

3.4. Summary

Our study pioneered an arbitrary polynomial form of the spatially-varied thermal conductivity to enhance heat dissipation rates for thermal management. We identify that thermal transport is enhanced using a concave-up thermal conductivity distribution that is highest near to the hot spot (i.e., an intercept) in both 1-D spherical and 1-D cylindrical systems. Our dimensionless thermal conductivity is generalized as a polynomial function of spatial coordinates to generate complex thermal conductivity distributions. We find that concave-up thermal conductivity distributions, peaked at the hot spot, maximize heat dissipation rates. Enhancements of more than 800% (i.e., $\epsilon_{sp} = 9.4$) relative to the UE case can be achieved using a spatially-parabolic thermal conductivity. For the large cylindrical systems, the enhancement ratios are *more* than 3 (more than 200%) for $n = 2$ and close to 4 ($\approx 300\%$) for $n = 3$. This spatially-parabolic thermal conductivity can effectively improve thermal dissipation rates using PCM/mesh composites to improve thermal management for electronic devices such as laptops and cellular phones.

Beyond our study using the constrained distribution of κ in Eq. (3.10) to maximize the thermal transport rate, the more general form of κ in Eq. (3.3) offers solutions for other design objectives. For instance, when constant heat transfer rates of PCMs are critical (i.e, a constant heat generation CPU needs a constant rate of heat dissipation), our generalized polynomial of thermal conductivity may generate spatial variations appropriate for leveling heat transfer rates during phase change processes.

3.5. Additional consideration of mesh design

Besides the volume fraction distribution, characteristics of the porous structures such as pore size in the mesh also affect the melting and solidification processes of a PCM/mesh composite [141-147]. Since thermal conductivities of meshes (e.g., ~ 200 W/m-K for aluminum) and PCMs (e.g., ~ 0.1 W/m-K for octadecane) are different from each other by as much as three orders of magnitude, this may cause non-equilibrium between meshes and PCMs during the melting process [147]. Thermal non-equilibrium (i.e., different temperatures) between meshes and PCMs may become significant during transient processes. Because of the thermal non-equilibrium, the performance of mesh/PCM may deviate from the ideal configuration where the mesh and PCM are in thermal equilibrium. Refs. [141, 147] indicate that larger pore sizes where the natural convection of melted PCMs becomes significant are more likely to realize thermal equilibrium between the mesh and PCM. Therefore, pore size is a critical factor to mesh design [141, 147] and one limitation of our study is that we have assumed equilibrium without specifying pore size.

Also, the minimum size of rod-like overhangs may need to be considered if the resolution of the AM goes down to the nanoscale. For rod-like overhangs at the nanoscale, thermal transport between metal and PCM is limited because the mean free paths of energy carriers (e.g., 19 nm for electrons in aluminum) are constrained by the rod size. For instance, Ref. [89] indicated that as the

strut size of the foams is larger than mean free path of the energy carriers (e.g, phonons in this study), there was no surface scattering of phonons, which constrains thermal transport between the PCM and struts. Although the resolution of current metal AM processes is on a microscale (e.g., 30-50 μm for selective laser melting processes), the minimum size of the rods can be an issue when the resolution at the nanoscale is reached.

4. Thermal conductivity of metal powders for powder bed additive manufacturing

This chapter has been submitted to *Additive Manufacturing* and under review.

4.1. Overview

Additive manufacturing is an advanced manufacturing technique that adds material in patterned layers to build a three-dimensional part [98-100, 105, 122, 140, 148-150]. A variety of AM processes, such as stereolithography, direct light projection, fused deposition modeling, inkjet, electron beam melting, and selective laser melting, are capable of fabricating parts from diverse materials, such as polymers, ceramics, and metals [98, 99]. The metal powder SLM processes manufacture parts by melting a thin powder layer atop the existing build with a rastered laser beam or electron beam. The powder bed is infiltrated with inert gases, such as Ar or N₂, to prevent oxidation from the powder surface in the SLM processes.

The powder bed serves as a temporary supporting structure during the build process for overhangs and cellular structures. This capability enables complex geometries with overhangs and enclosed cavities that cannot be fabricated by other processes [105, 122], but the quality of surface finish and accuracy of these structures are limited by thermal control of the powder bed [100]. Surfaces with rough finish and unexpected protrusions (i.e., dross) are common in overhangs or cellular structures due to heat trapping and overmelting of the thermally insulating powder that surrounds and supports these structures during the build [140, 150]. If the thermal conductivity of the powder bed is precisely known, dross can be limited by optimization of laser parameters such as laser beam power and scan speed. As yet, limited measurements of thermal conductivity have been made for the metal powders specific to the SLM processes. Therefore, we herein carry out

thermal conductivity measurements of packed beds of common AM metal powders infiltrated with various gases.

The thermal conductivities of gas infiltrated powder beds have been investigated for applications including catalytic reactors, heat exchangers, and thermal methods of oil recovery [151-171]. Key parameters such as particle size, contact resistance between solid particles, gas composition, gas pressure, and gas thermal accommodation coefficient have been studied in uncompressed powder beds infiltrated with motionless gases where conduction is the dominant heat transfer mechanism [151-153, 157-160, 162, 163, 169-171]. Heat conduction in a powder bed is typically modeled with three parallel pathways for energy transport: all gas, all solid, and a combination of solid and gas in series (i.e., gas/solid) [152]. For large particle sizes (e.g., ≈ 1 mm in diameter), the solid pathway dominates because the distance between contacts is large, and hence thermal contact resistance between solid particles can be neglected [151, 153, 155, 163, 171]. As the particle size decreases (e.g., ≈ 10 μm in diameter), the closely spaced contacts add considerable thermal contact resistance to the solid pathway, and the gas and gas/solid pathways influence the effective thermal conductivity [153, 158, 160, 164, 166-170]. In this case, thermal transport through the gas/solid path dominates the effective thermal conductivity except under vacuum conditions where there are too few gas molecules to conduct heat [166, 167]. For heat conduction through the gas/solid pathway, the effective thermal conductivity depends on the composition and pressure of the gas and its thermal accommodation coefficient with the solid [152, 153, 155, 158, 162, 163, 172]. Effective medium models can accurately predict the effective powder thermal conductivity for many solid/gas combinations, but Refs. [159-161, 163, 172] find deviations from experimental data when the ratio of the solid thermal conductivity to the gas thermal conductivity is large (e.g., $k_s/k_g > 100$). In this study, we measured the thermal

conductivities of several gas-infiltrated AM powders and determined the interplay between the properties of the gas and the powder using an existing analytical model of effective thermal conductivity.

4.2. Methodology and materials

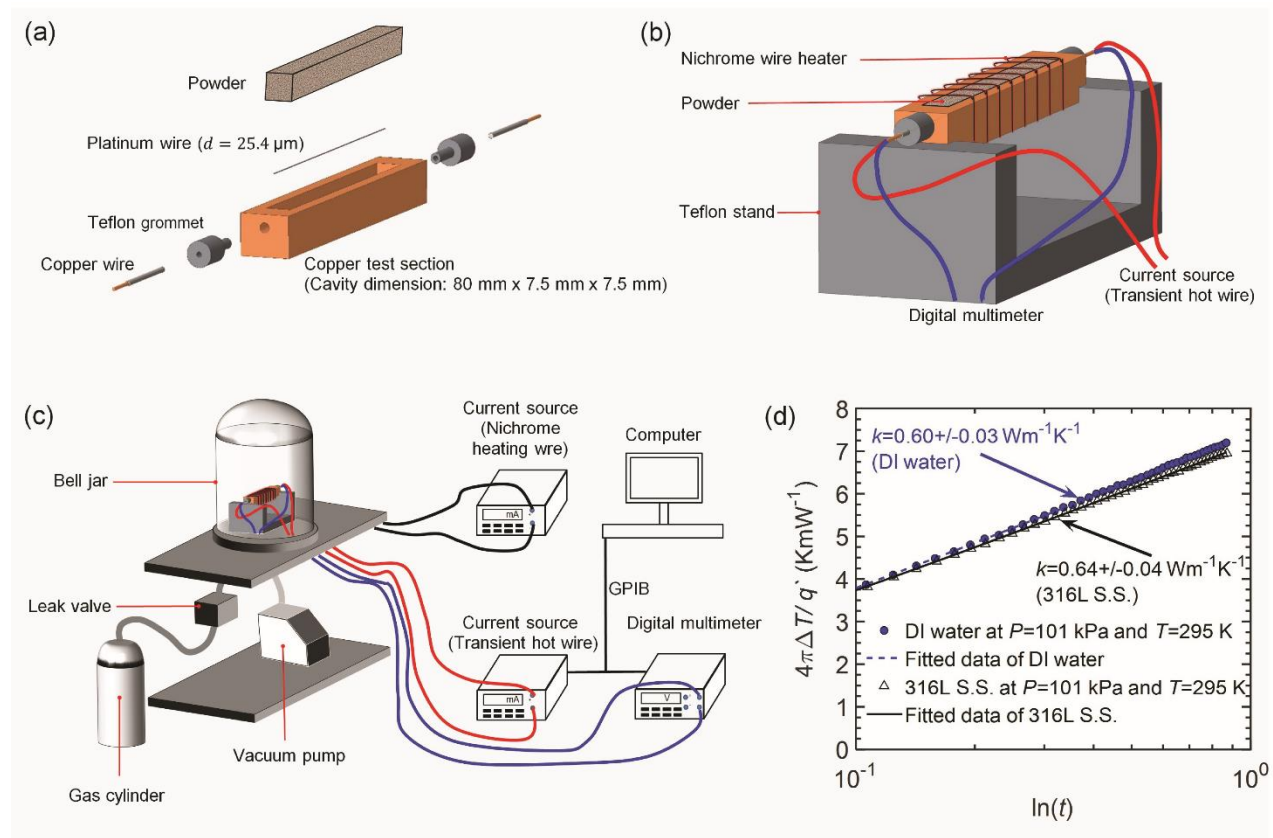


Figure 4.1 Transient hot wire experimental setup: (a) Measured powders were loaded into a copper test section immersing a platinum wire used for transient hot wire experiments. (b) A nichrome wire was wrapped around the copper test section to heat the measured powders up to 470 K for temperature dependence experiments. (c) The copper test section was placed in a bell jar, in which the pressure was controlled by a vacuum pump and a leak valve that feeds select gases to pressures ranging from 1.4-101 kPa. A current source and multimeter connected in a four-point configuration heated and measured the resistance of the platinum wire as a function of time to determine the thermal conductivity of the surrounding powder. (d) The normalized temperature rises of the platinum wire in DI water and the 316L stainless steel sample are plotted versus logarithmic time where the effective thermal conductivity is calculated from the slope of the fitted curve based on Eq. (4.3).

We herein report thermal conductivity measurements of five popular AM metal powders:

Inconel 718, 17-4 stainless steel, Inconel 625, Ti-6Al-4V, and 316L stainless steel (supplied by

Electro Optical Systems, Krailling, Germany). Thermal conductivities were measured using the transient hot wire method within a pressure range of 1.4-101 kPa and a temperature range of 295-470 K, using various infiltrating gases including Ar, N₂, and helium.

4.2.1. Sample preparation

The test section shown in Figure 4.1a was made from machined copper, chosen to help establish a uniform temperature distribution over the powder for temperature dependent measurements. A cavity 80 mm × 7.5 mm × 7.5 mm was machined in the copper test section to hold the powder sample. A platinum (Pt) wire 25.4 μm in diameter and coated with an electrically insulating Isonel layer 1.27 μm in thickness (A-M Systems, Sequim, WA, USA) was soldered to copper leads (AWG 22, 0.645 mm in diameter) and then fixed in place spanning the cavity, functioning as the transient hot wire (discussed further in section 4.2.2). To electrically insulate the solder joints from the powder sample and the copper test section, they were coated with an epoxy and held in place by Teflon grommets that fit into the copper test section. To validate each hot wire and ensure robust insulated solder joints, the thermal conductivity of deionized water (DI water), as shown in Figure 4.1d, at 295 K and 101 kPa (1 ATM) was benchmarked against Ref. [173] within ± 5% uncertainty (i.e., $0.60 \pm 0.03 \text{ W} \cdot \text{m}^{-1} \cdot \text{K}^{-1}$ for DI water). Each copper test section was then cleaned sequentially by Acetone, Isopropyl alcohol, and DI water. To remove the residual moisture, the empty copper test section was heated at a temperature of $70 \pm 2^\circ\text{C}$ for at least 30 minutes before loading the powder into the cavity.

The empty copper test section was weighed by an electronic balance (OHAUS, Parsippany, NJ, USA) and then weighed again after being filled with powder to determine the mass and void fraction of the powder. The powder was filled to the brim of the copper test section, and the surface of powder was leveled with a knife edge. The void fraction quantifies the volume fraction of the

cavity that is not filled by powder (i.e., the interstitial volume between powder grains). The void fraction ϵ of each powder sample was determined by

$$\epsilon = 1 - \frac{(m' - m)/\rho}{\forall}, \quad (4.1)$$

where m' is the total mass of the copper test section and the powder, m is the mass of the copper test section alone, ρ is the density of the powder, and \forall is the cavity volume. The density and void fraction of the powders are listed in Table 4.1.

Table 4.1 Properties and parameters of the powder bed samples ($\forall = 80 \text{ mm} \times 7.5 \text{ mm} \times 7.5 \text{ mm} = 4500 \text{ mm}^3$)

Powder	k_b (W/m-K) ^c	D_p (μm)	ϵ	ρ (kg/m^3)
Inconel 718	10.6 ($\pm 3\%$) [174]	35 ($\pm 15\mu\text{m}$)	0.39 ($\pm 0.2\%$)	8240
17-4 stainless steel	15.2 ($\pm 10\%$) ^a [175]	35 ($\pm 15\mu\text{m}$)	0.37 ($\pm 0.2\%$)	7800
Inconel 625	7.3 ($\pm 10\%$) ^a [176]	35 ($\pm 15\mu\text{m}$)	0.39 ($\pm 0.2\%$)	8400
Ti-6Al-4V	6.6 ($\pm 5\%$) ^b [177]	35 ($\pm 15\mu\text{m}$)	0.35 ($\pm 0.2\%$)	4410
316L stainless steel	13.4 ($\pm 5\%$) [178]	35 ($\pm 15\mu\text{m}$)	0.36 ($\pm 0.2\%$)	7900

^a 10% is the common uncertainty of the laser flash method [179].

^b 5% is the common uncertainty of the Kohlrausch method (p. 223, [177]).

^c k_b is bulk thermal conductivity.

^d D_p is average diameter of the powder particles.

4.2.2. Experimental setup and data reduction

The experimental setup was enclosed in a bell jar (Kurt J Lesker Company, Jefferson Hills, PA, USA), shown in Figure 4.1c, so that the gas pressure could be controlled. The pressure in the bell jar was controlled by evacuating the bell jar to 0.2 kPa and feeding gas through a leak valve

(Kurt J Lesker Company, Jefferson Hills, PA, USA) from the gas cylinder until the desired pressure was established. In order to control the ambient temperature of the powder sample, an insulated nichrome wire (shown in Figure 4.1b) was wrapped around the copper test section and connected to a current source (labeled Nichrome heating wire in Figure 4.1c), providing joule heating. The wire-wrapped copper test section was secured on a Teflon stand, for both electrical and thermal insulation from the bell jar baseplate. To measure the temperature dependent thermal conductivity, after the pressure setpoint (e.g., 101 kPa) was stabilized, the sample was heated by the nichrome heater, and its local temperature was monitored using the Pt wire's resistance.

In the transient hot wire method, the Pt wire serves as both a heater and a resistance-based thermometer. The Pt wire was 75 ± 2 mm long and was connected to a current source (labeled Nichrome heating wire in Figure 4.1c) and a digital multimeter, both of which were controlled by a computer through the GPIB interface. The current source leads and multimeter leads, as shown in Figure 4.1b, are connected in a four-point configuration to minimize errors due to contact resistance. At time $t = 0$, a current I in the form of a Heaviside step function joule heated the Pt wire. Heat diffused into the surrounding powder, and the temperature rise in the wire was measured by the multimeter based on its temperature dependent resistance. We determined the transient temperature rise ΔT from the varying resistance of the Pt wire ΔR , relative to its nominal resistance R_{ref} at 22°C, as

$$\Delta T = \frac{\Delta R}{R_{\text{ref}} \beta_{\text{ref}}}, \quad (4.2)$$

where $\beta_{\text{ref}} = 3.729 \times 10^{-3} \text{ K}^{-1}$ is the temperature coefficient of resistivity for Pt at 22°C.

An analytical solution to the radial heat diffusion equation, for a line source (i.e., the Pt wire) embedded in an infinite medium (i.e., the AM powders), was used to model the transient hot

wire experiment and extract the thermal conductivity of the powders [107-109, 180]. With these assumptions, the thermal conductivity of the measured powder can be expressed as

$$k = \frac{q'/4\pi}{d(\Delta T)/d(\ln t)}, \quad (4.3)$$

where t is the elapsed time measured from the onset of heating, and q' is the heat generation rate per unit length of the Pt wire ($q' = I^2 R_0/L$, where L is the length of wire and R_0 is the resistance of the platinum wire measured at the onset of heating in each measurement). We used $I = 5 - 70$ mA and a Pt wire with $R_0 = 15 - 17$ ohm.

According to Eq. (4.3), the extracted thermal conductivity of the powder bed sample, k , is inversely proportional to the slope of the normalized transient temperature rise $4\pi\Delta T/q'$ versus logarithmic time $\ln(t)$. From the raw data of DI water shown in Figure 4.1d, the slope of the normalized transient temperature rise is linear and thus validates our analytical model used to extract k (Eq. (4.3)). In addition, since k is inversely proportional to the slope where $k^{-1} \propto d(4\pi\Delta T/q')/d(\ln t)$ in Eq. (4.3), Figure 4.1d indicates that the extracted thermal conductivity of the powder at $P = 101$ kPa is higher than that of DI water. High k samples demand higher I to generate adequate ΔT (> 0.1 K), which maintains a high signal to noise ratio to ensure the linearity of the temperature rise with $\ln(t)$ as shown in Figure 4.1d.

We also confirmed that the transient hot wire signal was not influenced by the copper test section by calculating the worst-case (316L stainless steel infiltrated with He) thermal penetration depth $L_p = (4kt/C)^{1/2}$, where $k = 0.8$ W \cdot m $^{-1}$ \cdot K $^{-1}$, $t = 0.9$ s, and the volumetric heat capacity $C = 2.6 \times 10^6$ J \cdot m $^{-3}$ \cdot K $^{-1}$, to find $L_p = 1.1$ mm. Since L_p is much smaller than half the width and height (3.75 mm by 3.75 mm) of the cavity in the copper test section, the

temperature response of the transient hot wire method is sensitive only to the properties of the gas-infiltrated powders.

4.3. Results and discussion

4.3.1. Pressure dependent thermal conductivity

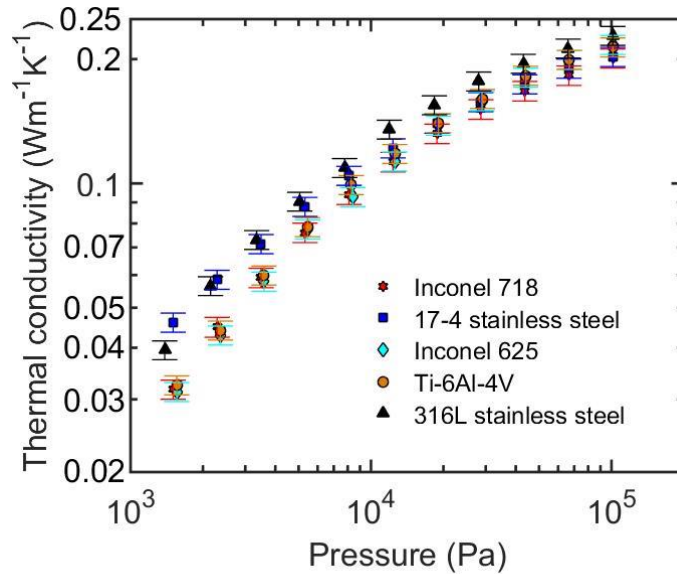


Figure 4.2 Thermal conductivities of the powders under Ar increases as the Ar pressure increases from 1.4 to 101 kPa at a temperature of 295 K.

The pressure dependent thermal conductivities of the five different powders in Ar at 295 K are shown in Figure 4.2. At the lowest pressure of ≈ 1.4 kPa, the thermal conductivity ranges from $0.031 \text{ W} \cdot \text{m}^{-1} \cdot \text{K}^{-1}$ for Inconel 625 to $0.046 \text{ W} \cdot \text{m}^{-1} \cdot \text{K}^{-1}$ for 17 – 4 stainless steel. At this pressure, the thermal conductivities of the different powder bed samples are less than $1/100^{\text{th}}$ of the solid bulk thermal conductivities k_b listed in Table 4.1. Furthermore, Figure 4.3 shows that the thermal conductivity of the 316L stainless steel powder is nearly independent of infiltrated gas at 2.2 kPa. Collectively these results indicate that the low pressure thermal conductivity is

dominated by contact resistance between the particles rather than the thermal conductivity of the particles or gases [152, 153, 155, 158].

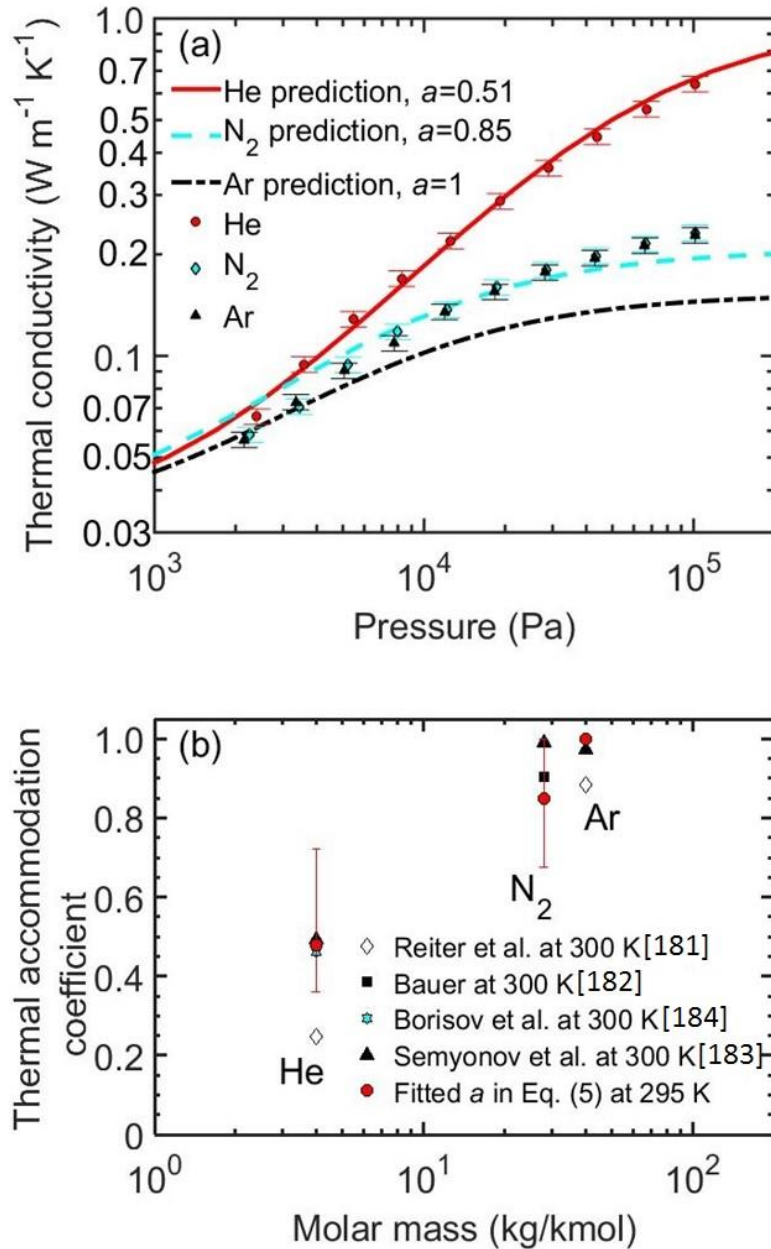


Figure 4.3 (a) Pressure dependent thermal conductivity of the 316L stainless steel powder. The prediction of thermal conductivity agrees with the experimental data for He and N_2 but underpredicts the experiment results for Ar. (b) The thermal accommodation coefficients established by fitting the data are compared with values from literature [162, 181-184].

The thermal conductivity increases with Ar pressure up to $0.21 - 0.23 \text{ W} \cdot \text{m}^{-1} \cdot \text{K}^{-1}$ at $P = 101 \text{ kPa}$ (1 atm), as shown in Figure 4.2. This rise in thermal conductivity of the powder ($\approx 0.2 \text{ W} \cdot \text{m}^{-1} \cdot \text{K}^{-1}$) is much larger than the thermal conductivity of Ar itself ($k_g = 0.0176 \text{ W} \cdot \text{m}^{-1} \cdot \text{K}^{-1}$) and hence cannot simply result from parallel and independent contributions of the solid and infiltrating gas [152, 153, 155]. This additional enhancement results from thermal transport through collisions between gas molecules and solid particles, which were modeled as a solid thermal resistance and a gas thermal resistance in series by Masamune and Smith [152].

The pressure dependent thermal conductivities of 316L stainless steel powder infiltrated by Ar, N₂, and He are shown in Figure 4.3a, where at 101 kPa thermal conductivity of 316L stainless steel powder infiltrated with He is distinctively higher than those infiltrated with N₂ and Ar. Infiltration with He provides more than 300% enhancement in powder thermal conductivity, relative to N₂ and Ar, which may help dissipate heat in overhanging regions to improve surface quality and reduce dross. This enhancement in powder thermal conductivity infiltrated with He is also predicted using the analytical model of effective thermal conductivity k_e by Ref. [152], as shown in Figure 4.3a, in comparison with our experimental results. Ref. [152] defines the effective thermal conductivity as a function of the geometrical parameters and gas and solid thermal conductivities

$$k_e = \alpha \epsilon k_g + \frac{(1 - \alpha \epsilon)(1 - \delta)}{\frac{\phi}{k_g^*} + \frac{1 - \phi}{k_s}} + (1 - \alpha \epsilon) \delta k_s, \quad (4.4)$$

where k_g is the gas thermal conductivity, k_s is the thermal conductivity of the bulk solid ($k_s = k_b$ in Table 4.1). Parameters δ , α and ϕ are dimensionless geometrical functions of ϵ , k_s and k_e^0 (k_e^0

is the powder thermal conductivity at zero pressure). The gas thermal conductivity k_g^* between simulated parallel plates separated by distance L_g takes the form

$$k_g^* = \frac{k_g}{1 + \frac{\frac{2-a}{\sqrt{2}a} \left(\frac{9\gamma-5}{\gamma+1} \right) \frac{k_B T}{\pi \sigma^2 P}}{L_g}}, \quad (4.5)$$

where a is the thermal accommodation coefficient, γ is the specific heat ratio of the gas, k_B is the Boltzmann constant ($1.38 \times 10^{-23} \text{ J} \cdot \text{K}^{-1}$), T is the temperature of the powder sample, σ is the gas molecule's effective collision diameter, P is the pressure in the bell jar, L_g is the effective path length between adjacent solid powder particles as a function of ϵ and D_p , where D_p is the average diameter of the powder particles, which are assumed to be spheres. As listed in Table 4.2 for 316L stainless steel, the geometrical parameters (ϵ , D_p , and L_g) and material properties of the powders and gases (k_s , k_g , γ , and σ) are known, and a is a fitting parameter used to obtain to the least square fit of Eq. (4.4) to the data. The value $k_e^0 = 0.03 \text{ W} \cdot \text{m}^{-1} \cdot \text{K}^{-1}$ was also used as a fitting parameter but constrained to be equivalent between all infiltrating gases as it represents the thermal conductivity of the evacuated powder.

Table 4.2 Geometrical parameters and properties of powder bed samples of 316L stainless steel at a temperature of 295 K for pressures ranging from 1.4 – 101 kPa ($\epsilon = 0.36$, $D_p = 35 \text{ } \mu\text{m}$, $k_e^0 = 0.03 \text{ W/m-K}$, and $k_s = k_b = 13.4 \text{ W/m-K}$)

Gas	k_g (W/m-K)	γ [185]	σ (pm) [186]	L_g (μm)	a (from fit)
Helium	0.1502 [82]	1.660	218		$0.48^{+0.24}_{-0.12}$
Nitrogen	0.0255 [82]	1.401	375	3.67	$0.85^{+0.15}_{-0.17}$
Argon	0.0176 [187]	1.670	364		$1.00^{+0}_{-0.0002}$

The effective thermal conductivity using the model from Ref. [152] agrees well with the experimental data when the powder is infiltrated with both He and N₂ from 2 to 101 kPa, yet is lower than the experimental measurements when the powder is infiltrated with Ar. The discrepancy in the case of Ar may come from a high ratio of solid thermal conductivity to gas thermal conductivity ($k_s/k_g > 700$), which has been attributed to under-prediction by the effective medium models in prior studies [18–20, 22]. The fitted thermal accommodation coefficients a are $0.48^{+0.24}_{-0.12}$, $0.85^{+0.15}_{-0.17}$, and $1.00^{+0}_{-0.0002}$ respectively for He, N₂, and Ar, where the error bars of a are estimated using the uncertainties of k_b , D_p and ϵ , listed in Table 4.1. The thermal accommodation coefficient characterizes the extent of thermal acclimation of gas molecules to a solid surface after a collision, and ranges from 0 to 1 [153, 188]. The thermal accommodation coefficient is 1 when the gas molecule’s average temperature after a collision is equal to the temperature of the solid and 0 when it is unchanged relative to its temperature before the collision. Higher thermal accommodation implies better thermal energy transport through the collisions between the gas molecules and the powder. For the 316L stainless steel powder, the thermal accommodation coefficient is lower for lighter gases ($a = 0.48$ for He) and higher for heavier gases ($a = 1$ for Ar), in agreement with the predictions from Ref. [172] and the experimental results from Refs. [162, 181-184] shown in Figure 4.3b. Notably, because thermal accommodation is already at its limit ($a = 1$) for Ar, it is not possible to raise the prediction by increasing a , further suggesting the inadequacy of the model for Ar.

4.3.2. Temperature dependent thermal conductivity

The temperature dependent thermal conductivities of the powders are shown in Figure 4.4 from 295 to 470 K. The thermal conductivities increase monotonically from 295 to 470 K at a gas pressure of 101 kPa, while at a low gas pressure of 1.6 kPa, they remain essentially constant.

This result indicates that the increase of effective thermal conductivity is mainly due to the increase of gas thermal conductivity at 101 kPa in agreement with Refs. [152, 153, 155, 158, 163].

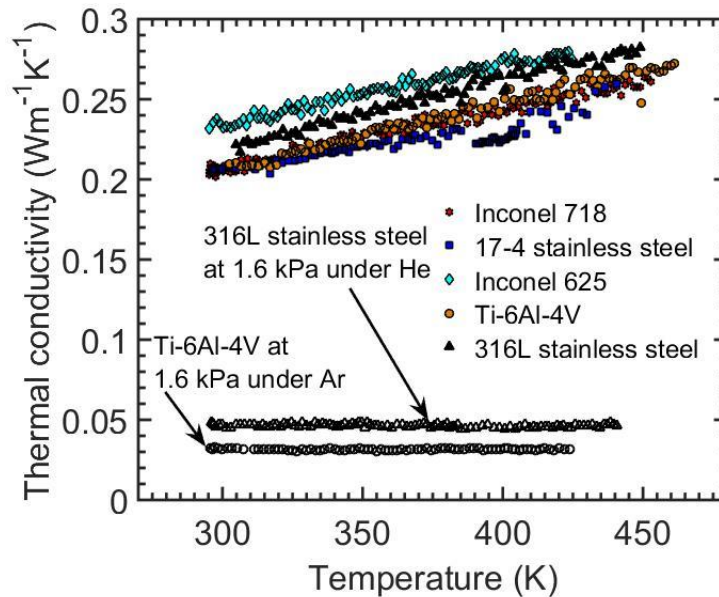


Figure 4.4 Temperature dependent thermal conductivity of the powders at 101 kPa under Ar increases as the temperature is raised from 295 to 470 K. The thermal conductivity of 316L stainless steel and Ti-6Al-4V at 1.6 kPa under Ar and He respectively shows no temperature dependence from 295 to around 430 K.

At a gas pressure of 1.6 kPa, heat conducts mainly through the solid pathways where thermal contact resistance dominates [153, 158, 160, 164, 166-170]. The effective thermal conductivities of 316L stainless steel and Ti-6Al-4V shown in Figure 4.4 are constant at 1.6 kPa, providing evidence that thermal contact resistance is temperature invariant in our powders. Furthermore, this data indicates that radiative transport, which increases with temperature (as T^4 for far field effects), is negligible over this temperature range perhaps owing to the low emissivity of metals [41] and their limited near field radiative exchange [189, 190].

We incorporated the temperature dependent thermal conductivity of gases ($k_g = k_g(T)$) into Eq. (4.4) and determined the temperature dependent $k_g^*(T)$ from Eq. (4.5). As shown in Figure

4.5, the prediction agrees well for both He and N₂ yet fails again for Ar infiltrated 316L stainless steel powder. Despite failing in absolute magnitude, however, the predicted temperature trend for Ar is consistent with the data. Collectively the temperature invariance of the low pressure data and the predicted temperature dependence of the high pressure data indicates that higher gas thermal conductivity at a higher temperature results in the increase of the powder's effective thermal conductivity.

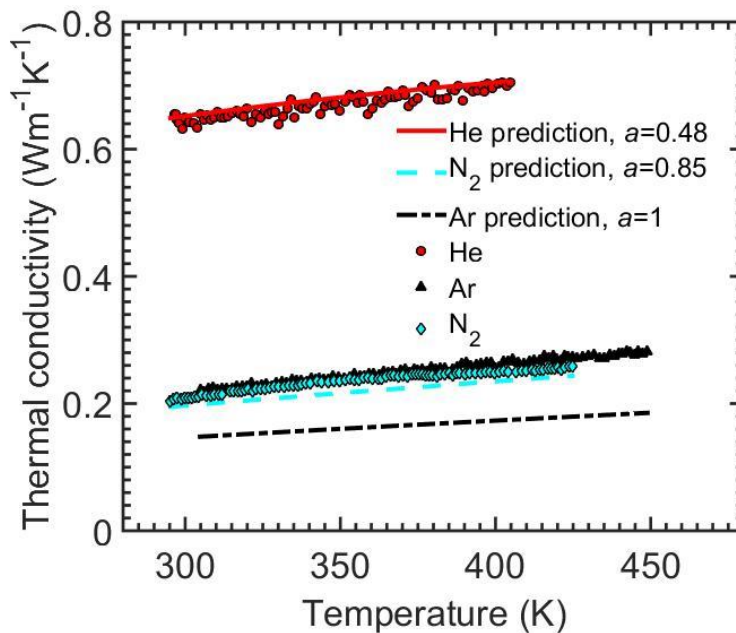


Figure 4.5 Temperature dependent thermal conductivity of the 316L stainless steel powder at 101 kPa under He, N₂, and Ar. By using the model from Ref. [152] with a temperature dependent gas thermal conductivity, we accurately match the temperature dependent data for He and N₂ but underpredict the magnitudes for Ar as we observed for pressure dependent data.

Notably, we have herein assumed that the thermal accommodation coefficients derived from the pressure dependent measurements are invariant over our temperature range. No universal temperature dependence of the thermal accommodation coefficient for a gas has been observed because temperature dependence of the thermal accommodation coefficients is affected by the properties of both the gas and solid [191-194]. Even with the same solid-gas pair, different

temperature trends have been observed [195, 196]. Therefore, our assumption of constant thermal accommodation coefficients is reasonable and shows an agreement between the prediction and data without further complication.

4.3.3. Sensitivity analysis

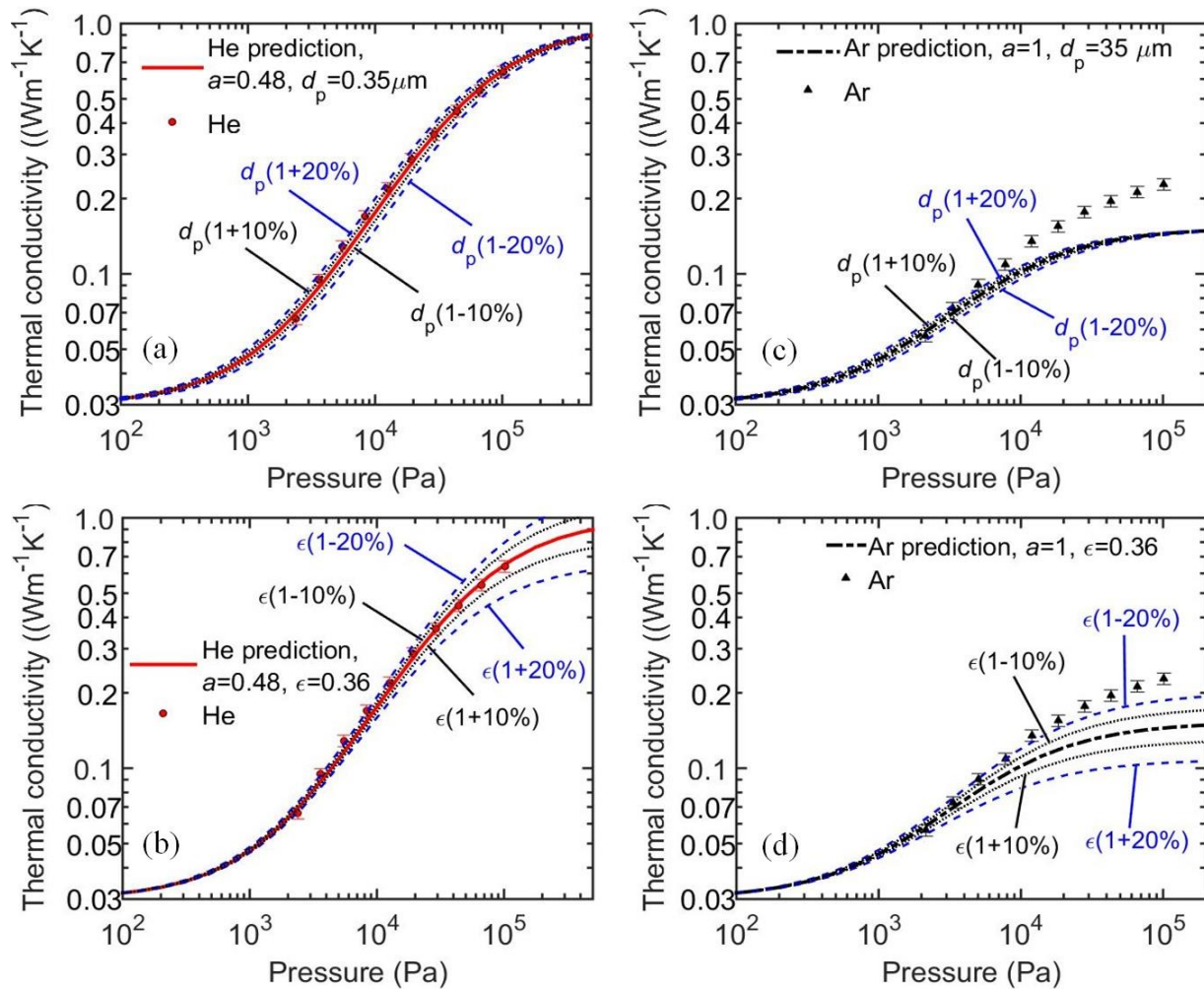


Figure 4.6 Sensitivity analysis. The thermal conductivity of 316L stainless steel is predicted using Eq. (4.4) with He and N₂. In (a) and (b), the sensitivity analysis of the case infiltrated with He is tested using average powder diameter D_p and void fraction ϵ . In (c) and (d), the sensitivity analysis of the case infiltrated with Ar is tested using average powder diameter D_p and void fraction ϵ .

We perform a sensitivity analysis to identify how sensitive the predicted thermal conductivity of 316L stainless steel using Eq. (4.4) is to different average powder diameter D_p and

void fraction ϵ . These two parameters were varied by +/- 20% (i.e., $28 \mu\text{m} \leq D_p \leq 42 \mu\text{m}$ and $0.288 \leq \epsilon \leq 0.432$) while fitted thermal accommodation coefficients are the same for each infiltrating gas, He and Ar, respectively.

In Figure 4.6a, a marginal variation of thermal conductivity of 316L stainless steel/He is plotted with D_p +/- 10% and 20% ($\epsilon = 0.36$ here). The change of D_p affects L_g more relative to other geometrical parameters. Therefore, the interplay between L_g and gas mean free path changes the thermal conductivity horizontally but preserves the maximum (at high pressure) and minimum (solid/solid at low pressure) the same. The case infiltrated with Ar shown in Figure 4.6c shows similarly weak variation within D_p +/- 20%.

The test of 316L stainless steel/He with respect to ϵ +/- 10% and 20% ($D_p = 35 \mu\text{m}$ here), as shown in Figure 4.6b. The change of epsilon affects the series gas thermal pathway (L_g) and the length ratio of series pathway of gas/solid (ϕ) and thus overall thermal resistance of gas/solid in series. For instance, by decreasing epsilon by 20%, the solid portion in the series thermal pathway is more than that with original epsilon. This results in the better thermal transport at high pressure when the solid portion is bridged by the increasing series gas pathway and higher thermal conductivity relative to the case with original epsilon. However, at low pressure, the solid/solid thermal pathway is insensitive to ϵ , as it is dominated by contact resistance, and the thermal conductivity remains the same. In Figure 4.6d, the similar trend in the case infiltrated with Ar affirms this variation.

4.4. Summary

We investigated the thermal conductivities of five AM powders for the SLM processes using the transient hot wire method with different infiltrating gases. We find that the pressure and

the composition of the gas have a significant effect on the thermal conductivity of the powder when we consider interactions between that solid and the gas, rather than simply treating them as separate but parallel pathways for heat. We find reasonable agreement with an effective medium model to our experimental data. The highest temperature of our measurement is limited to 200°C (473 K) due to the maximum working temperature of the Insonel insulation of the Pt wire and the epoxy in the transient hot wire setup. Nevertheless, these measurements of AM powder thermal conductivities provide a guideline to optimize laser parameters for better thermal control of the AM processes, and the predictions from the effective medium model can be scaled to higher temperatures. We cannot rule out the possibility that other heat transfer processes may play a role as we approach the sintering temperature, but radiative effects appear minimal over our temperature range. Collectively our results suggest that the infiltrating gas can be an important parameter in controlling heat transfer in the powder in metal AM processes. Infiltration with He provides more than 300% enhancement in powder thermal conductivity, relative to N₂ and Ar, which may help dissipate heat in the overhang regions to improve surface quality and reduce dross.

4.5. Additional consideration of helium in selective laser melting processes

Practically, cost-effectiveness such as the price of He is always one of the major concerns to the selection of the inert gas in SLM, although the increase of powder thermal conductivity infiltrated with helium, relative Ar and N₂, can realize better thermal control of overhangs and good surface quality of final products [197]. To incorporate He in a cost-effective way, there are alternatives-1.) Using gas mixture of He/Ar or He/N₂ and 2.) Purging SLM chamber with He only in the final stage. For the gas mixture, the thermal conductivity of He/N₂ is 0.34 W/m-K with a He mole fraction of 0.159 [198-200], and nearly 40% higher than pure N₂. This marginal increase would nonetheless improve thermal control of the powder bed. For purging the SLM chamber, Ar

and N_2 can be utilized as the gas source during most of the purging procedure, while at the end of this procedure He can be switched as the major gas so as to maintain the powder bed and the chamber infiltrated with He.

5. Side project-study of thermal transport using a two-temperature model including non-surface heat deposition

This chapter was published in *Journal of Applied Physics* [201].

Thermoreflectance-based techniques can now create experimental length and timescales comparable to energy carrier length and timescales and thus enable resolution of the underlying processes governing thermal transport [202]. The primary thermoreflectance-based techniques used to measure thermal transport properties are TDTR [203-206] and FDTR [207-209]. A previous study using FDTR observed a heating frequency-dependent thermal conductivity in silicon at room temperature and attributed it to nondiffusive phonon transport in the silicon substrate [208]. Yet, the results are in disagreement with TDTR measurements where the thermal conductivity of silicon is invariant with heating frequency [210, 211]. This discrepancy may result from the use of different thin film metal transducers on samples in TDTR and FDTR. The two major complications of transducers to analysis and interpretation of experimental results are (1) an additional fitted thermal interface conductance G between the transducer and the sample and (2) interactions between electrons and phonons in metal transducers. In this work, the second complication is addressed and discussed.

A tool well suited to capture these physics is the two-temperature diffusion model, which has been applied to thermoreflectance experiments in the literature [212-218]. The two temperature model describes heat transfer in the n^{th} layer through two distinct channels, each having its own thermal conductivity, volumetric heat capacity, and temperature. Heat is exchanged between each channel at a rate proportional to the coupling parameter in that layer. In an FDTR experiment, a periodic, radially Gaussian heat flux with angular frequency ω is incident on the sample. Thus, to

be consistent with the geometry of the experiment and to take advantage of the cylindrical symmetry of the problem, we solved the coupled heat diffusion equation in cylindrical coordinates.

We first fit BB-FDTR measurements of SiO₂ and platinum at a temperature of 300 K with our two-temperature solution to parameterize the gold/chromium transducer layer. On the top of these samples are gold/chromium transducers. Since no heating frequency dependence is expected in SiO₂ and platinum samples due to short carrier mean free paths that ensure diffusive transport, the parameters of the transducers, such as heat deposition depth, electron-electron interface thermal conductance, and phonon-phonon interface thermal conductance, can be consistently characterized.

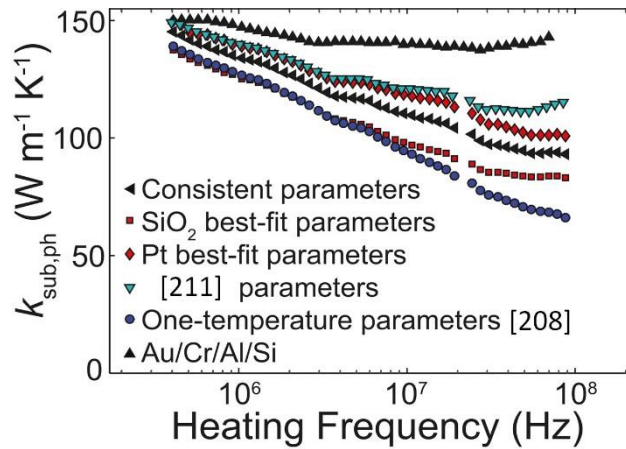


Figure 5.1 We window fit BB-FDTR phase data for silicon at $T = 300$ K from Ref. [208]. We measure and window fit BB-FDTR phase data for a gold/chromium/aluminum/silicon sample with the two-temperature model and find the thermal conductivity to be independent of heating frequency compared to the gold/chromium/silicon sample.

We then refit BB-FDTR measurements of silicon shown in Figure 5.1 and find that accounting for nonequilibrium between electrons and phonons in the gold layer does lessen the previously observed heating frequency dependence reported in Regner et al. [208], but does not completely eliminate it (i.e., the thermal conductivity is still a strong function of heating frequency).

We performed additional experiments on a gold/chromium/aluminum/silicon sample, which showed a thermal conductivity with limited heating frequency dependence in our BB-FDTR experiments, suggesting that the metal dielectric interface plays a large role in the observed heating frequency dependence of the dielectric substrate [219, 220]. Our hypothesis is that the discrepancy between thermoreflectance measurements with different transducers results in part from spectrally dependent phonon transmission at the transducer/silicon interface. The different metal/dielectric interfaces may selectively excite different phonon modes in the dielectric substrate resulting in different nondiffusive effects and thus observation of different k vs. f behavior.

6. Conclusions and future work

Recent advances in additive manufacturing have already enabled new products with complex geometries, which were previously impossible to fabricate with traditional manufacturing methods. For AM products and processes, thermal transport matters. The complex geometries facilitated by AM provide unprecedented tunability and controllability of thermal transport in porous materials to enhance the thermal conductivity of PCMs for energy storage and thermal management. Realization of such porous structures relies on precise characterization of AM powder properties, which will help to optimize parameters in AM machines (e.g., inert gas composition, gas pressure, laser power, and laser feed speed). In the near future, interdisciplinary study of thermal science and AM will lead to valuable technologies.

6.1. Amplified thermal transport of PCMs using AM metal meshes for energy storage

Our study in chapter 2 covered the first-ever investigation of the effect of spatially-enhanced thermal conductivity on charge/discharge rates in latent energy storage applications. We pioneered a spatially-linear thermal conductivity in the analytical solution to the Stefan problem. The enhancement ratio to the charge rate, compared to homogeneously (or uniformly)-enhanced composites, provides a straightforward quantification of the effectiveness of spatially-enhanced thermal conductivity. Key findings were:

- Higher enhancement of spatially-varied thermal conductivity is beneficial to the charge/discharge processes. When the thermal conductivity is enhanced higher near to the heat source, the charge/discharge (melting/solidification) processes are accelerated.
- Higher enhancement can be achieved in radial systems (i.e., cylindrical systems). The maximum enhancement ratio in a 1-D planar configuration is 11.6%, whereas the

maximum enhancement ratio in a cylindrical wall, with a ratio of radii as 2, heated at the interior circumference, reaches ~30%. More extreme enhancements can be achieved in cylindrical coordinates because in a homogeneous solid cylindrical annulus the derivative of thermal resistance, which represents the thermal resistance per unit cylindrical shell thickness, is highest at $r = r_1$ (i.e., thermal resistance accumulates most rapidly when the melting front is near $r = r_1$). As a result, spatial enhancement of thermal conductivity near the heat source at r_1 drastically reduces the time averaged thermal resistance during the charge/discharge process.

- In cylindrical systems with a higher ratio of radii (~1000), while having the same volume fraction as a 1-D slab, the enhancement ratio is as high as ~2.4 (~140% higher than homogeneously-enhanced cases). The higher the ratio of radii in the cylinders, the larger the possible spatial variation of metal volume fraction. Therefore, with much higher mesh volume fraction near to the heat source, the spatially-varied thermal conductivity (i.e., higher intercept) is enhanced more near to the heat source at the inner radius.

6.2. Prompt thermal transport of PCMs incorporating AM metal meshes for thermal management

Chapter 3 explores the effect of more complex variation of thermal conductivity to the thermal transport for electronic thermal management. We generalize the spatially-enhanced thermal conductivity as a polynomial function of space. Beyond Cartesian and cylindrical systems in chapter 2, we formulated our solution for spherical systems to maximize the heat dissipation using AM mesh/PCM composites, compared to uniformly-enhanced cases. Key findings were:

- Spatially-enhanced thermal conductivity at inner radius can be 9 times higher than uniformly-enhanced cases, while the average metal volume fractions are the same. We examined different geometrical combinations (e.g., vertex location and concave-up shape) of a parabolic thermal conductivity, and found that, with a concave-up shape and a vertex far away from the inner radius, thermal conductivity is enhanced more than 9 times higher than the uniformly-enhanced cases.
- Enhancement ratio to the heat dissipation rates reaches 8.2 for selected ratio of radii. We found that the parabolic thermal conductivity with a concave-up and a vertex far away from inner radius effectively amplifies the enhancement ratio to heat dissipation, whereas, with concave-down shape, the maximum enhancement ratio reaches 2.4, which was close to linearly-enhanced cases in selected cylindrical systems.

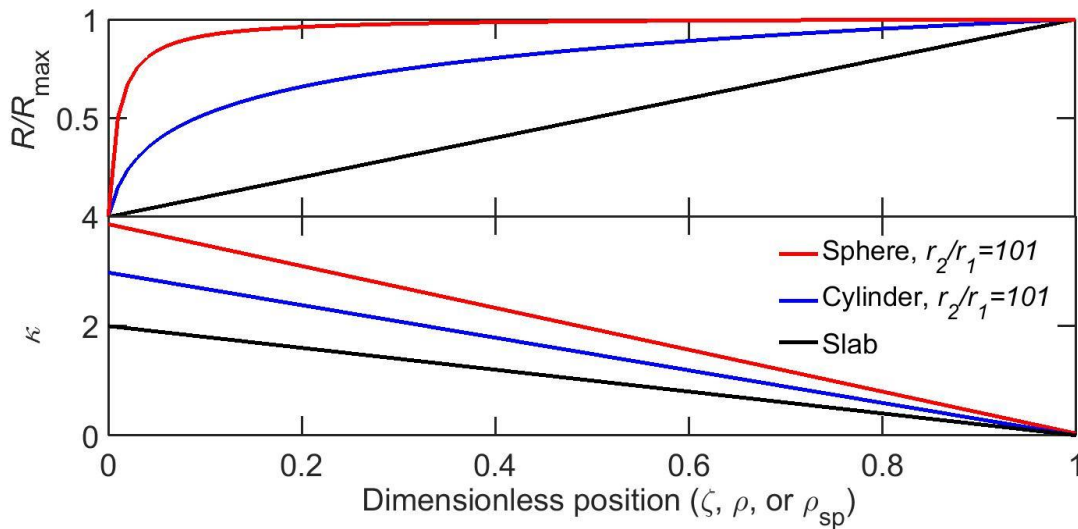


Figure 6.1 Schematic of thermal resistances of different geometries. The thermal resistance of the spherical system, near to the heat source at the dimensionless position of 0, increases much faster than the other two geometries. Therefore, when spatially-enhanced thermal conductivity is high near to the position of 0, the thermal resistance in the spherical system is greatly reduced.

- The spatially-enhanced thermal conductivity is the most effective to thermal transport in spherical systems. The normalized thermal resistances of phase change processes from different geometries are compared in Figure 6.1. The normalized resistance of 1 indicates the maximum thermal resistance, which takes place at the end of phase change. The thermal resistance of the spherical system, near to the heat source at the dimensionless position of 0, increases much faster than the other two geometries. Therefore, when spatially-enhanced thermal conductivity is high near to the position of 0, the thermal resistance in the spherical system is greatly reduced.

6.3. Thermal conductivity of metal powders for powder bed additive manufacturing

In chapter 4, we report the measurements of the thermal conductivities of five SLM metal powders for powder bed additive manufacturing (Inconel 718, 17-4 stainless steel, Inconel 625, Ti-6Al-4V, and 316L stainless steel) using the transient hot wire method. The measurements were conducted in a configuration similar to that inside the SLM machines. Argon, nitrogen, and helium were individually utilized as the infiltrating gas in the measurement. The measurements were also carried out under different combinations of gas pressure and temperature. Key findings are:

- The pressure and the composition of the gas have a significant influence on the effective thermal conductivity of the powder, but the metal powder properties and temperature do not. Infiltration with He provides more than 300% enhancement in powder thermal conductivity, compared to N₂ and Ar, which may help dissipate heat in overhanging regions to improve surface quality and reduce dross.
- The fitted thermal accommodation coefficients of gases in the measurement agree with reported values in the existing literature. The accommodation coefficient of Ar is 1,

whereas it is 0.4 for He. This discrepancy implies that there are complex physics beyond the gas thermal conductivity that impact the effective thermal conductivity of metal powders.

- Both the pressure and temperature dependent thermal conductivities are well-predicted using an existing analytical model from Ref. [152]. This agreement confirms the significance of infiltrating gas properties to the effective thermal conductivity of AM powders.

6.4. Future outlook

6.4.1. Experiments of the charging processes of mesh/PCM composites

The distinct enhancement of thermal transport in our analysis is beneficial to energy storage and thermal management applications. Experiments of phase change processes using mesh/PCM composites would be another critical step to see how these composites work practically. For energy applications, cylindrical systems is a common geometry. Therefore, it would be useful and exciting to have experimental data on cylindrical systems. As described in section 7.9, a simulation of pure PCM in a vertical cylinder, with a heat source in the center, was carried out so as to understand the melting processes in these configurations. Besides heat conduction being modeled in the melted PCMs, natural convection may come into play to affect the thermal transport [45, 93, 94]. This simulation can be a benchmark for comparison with experiments of mesh/PCM cases.

6.4.2. Infiltration of He in SLM machines for overhangs

The infiltration of He in AM metal powder in our measurements showed a much higher thermal conductivity than that with common inert gas, Ar, in SLM processes. This characterization of effective thermal conductivity is not only a reference guide for optimization of SLM machine parameters (e.g., laser power and laser feed speed) for overhangs but also indicates that He is a

potential inert gas that can help dissipate heat from overhangs. Recently, a similar application of He for SLM processes was also suggested [197]. It would be compelling to build structures with overhangs in He-filled chambers in SLM machines – a fact that opens another door for advanced thermal control in the powder bed.

7. Appendix

7.1. Analysis adding spatially-dependent volumetric latent heat

As the volume fraction of a mesh v_{Mesh} increases, the effective latent heat of fusion of the PCM composite decreases. For a uniformly-enhanced case, λ in Eq. (2.2) can be modified as

$\lambda_{\text{UE}} = \lambda(1 - v_{\text{Mesh}})$. For a spatially-enhanced case, λ is replaced as $\lambda_{\text{SE}} = \lambda(1 - v'_{\text{Mesh}})$. The dimensionless energy balance in 1-D Cartesian coordinates from Eq. (2.6) becomes

$$-\kappa(\zeta) \frac{\partial \theta(\zeta, \tau_z)}{\partial \zeta} \Big|_{\zeta=\zeta_m(\tau_z)} = 2 \frac{\lambda_{\text{SE}}}{\lambda_{\text{UE}}} \frac{d\zeta_m}{d\tau_z} = 2 \left(\frac{1 - v'_{\text{Mesh}}}{1 - v_{\text{Mesh}}} \right) \frac{d\zeta_m}{d\tau_z}, \quad (7.1.1)$$

where v'_{Mesh} can be expressed using Eq. (2.17) ($\kappa = k_{\text{PCM}}/k_{\text{UE}} + v'_{\text{Mesh}} \Delta k/k_{\text{UE}}$ where $\Delta k = k_{\text{Mesh}} - k_{\text{PCM}}$, thermal conductivity difference) as a linear function

$$v'_{\text{Mesh}}(\zeta) = \left[\frac{2k_{\text{UE}}(1 - B)}{\Delta k} \right] \zeta + \frac{Bk_{\text{UE}} - k_{\text{PCM}}}{\Delta k}. \quad (7.1.2)$$

By incorporating Eq. (7.1.2) into Eq. (7.1.1) with the same initial condition for Eq. (2.6), the optimal enhancement ratio with λ_{SE} ; $\epsilon'_{z,\text{opt}}$, can be obtained.

The dimensionless energy balance in 1-D cylindrical coordinates from Eq. (2.14) becomes

$$\begin{aligned} & -\kappa(\rho) \frac{\partial \theta(\rho, \tau_r)}{\partial \rho} \Big|_{\rho=\rho_m(\tau_r)} \\ & = \left(\frac{1 - v'_{\text{Mesh}}}{1 - v_{\text{Mesh}}} \right) \frac{(R_{\text{max}} - 1)^2}{\frac{R_{\text{max}}^2}{2} \ln(R_{\text{max}}) - \frac{R_{\text{max}}^2}{4} + \frac{1}{4}} \frac{d\rho_m(\tau_r)}{d\tau_r}. \end{aligned} \quad (7.1.3)$$

The volume fraction v'_{Mesh} using Eq. (2.20) takes the form

$$v'_{\text{Mesh}}(\rho) = \left[\left(\frac{3(1-H)(R_{\text{max}}+1)R_{\text{min}}^2}{2R_{\text{max}}^3 - 3R_{\text{max}}^2 + 1} \right) \frac{k_{\text{UE}}}{\Delta k} \right] \rho + \frac{Hk_{\text{UE}} - k_{\text{PCM}}}{\Delta k}. \quad (7.1.4)$$

By incorporating Eq. (7.1.4) into Eq. (7.1.3) with the same initial condition used for Eq. (2.14), the optimal enhancement ratio with λ_{SE} , $\epsilon'_{r,\text{opt}}$, can be obtained. The relative difference is defined as

$$\Delta\epsilon_{i,\text{opt}} = \epsilon_{i,\text{opt}} - \epsilon'_{i,\text{opt}}, \quad (7.1.5)$$

where the subscript $i = z$ or r .

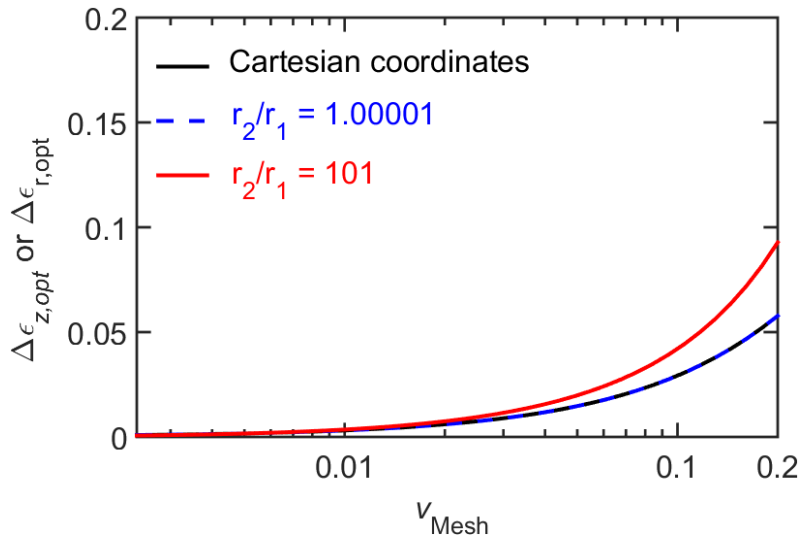


Figure 7.1 The difference of the optimal enhancement ratio of the average charge/discharge rates using λ and λ_{SE} vs. v_{Mesh} . With $v_{\text{Mesh}} < 0.2$, the small difference indicates that the solutions using constant λ are not significantly affected.

The relative difference of optimal enhancement ratio between using λ and λ_{SE} from $v_{\text{Mesh}} = 0.001$ to $v_{\text{Mesh}} = 0.2$ is shown in Fig. A.1. The maximum difference reaches 0.1 with $v_{\text{Mesh}} = 0.2$ and $r_2/r_1 = 101$. This difference implies that the change from λ to λ_{SE} does not

significantly decrease the optimal enhancement. This result validates the assumption of using the constant λ to simplify our analysis.

7.2. Derivation of the maximum melting times ($t_{z,\max}$ and $t_{r,\max}$)

The maximum melting time is the time for the melting front to reach $z_m = d$ ($t = t_{z,\max}$) in 1-D Cartesian coordinates or $r_m = r_2$ ($t = t_{r,\max}$) in 1-D cylindrical coordinates. The maximum melting time for uniform mesh (k_{UE}) is determined when k_{UE} is substituted for $k(z)$ in Eqs. (2.1) and (2.2) or for $k(r)$ in Eqs. (2.9) and (2.10). The temporal temperature distribution $T(z, t) = T_s + (T_m - T_s)z/z_m$ in 1-D Cartesian coordinates is substituted into Eq. (2.2), and $t_{z,\max}$ is acquired by integration as

$$\int_0^{t_{z,\max}} dt' = \int_0^{z_m=d} dz'_m z'_m \left[\frac{\lambda}{k_{UE}(T_s - T_m)} \right]. \quad (7.2.1)$$

For 1-D cylindrical coordinates, $T(r, t) = T_s + (T_m - T_s)\ln(r_m/r_1)$ is substituted into Eq. (2.10), and $t_{r,\max}$ is acquired by integration as

$$\int_0^{t_{r,\max}} dt' = \int_{r_1}^{r_m=r_2} dr'_m r'_m \ln\left(\frac{r'_m}{r_1}\right) \left[\frac{\lambda}{k_{UE}(T_s - T_m)} \right]. \quad (7.2.2)$$

7.3. Derivation of the enhancement ratio in 1-D cylindrical coordinates (ϵ_r)

The enhancement ratio of the average charge/discharge rate is defined as the reciprocal of the nondimensionalized time with $\rho_m = 1$ and $R_m = R_{\max}$ in Eq. (2.15), which is acquired by integration of Eq. (2.14).

We obtain Eq. (2.14) by substituting $dt = d\tau_r t_{r,\max}$, $k(r) = \kappa(\rho)k_{UE}$, $dT(r, t) = d\theta(\rho, \tau_r)(T_s - T_m)$, $dr = d\rho(R_{\max} - 1)r_1$, $dr_m = d\rho_m(R_{\max} - 1)r_1$ into Eq. (2.10). After rearrangement, the right-hand-side of Eq. (2.14) takes the form

$$\begin{aligned}
-\kappa(\rho) \frac{\partial \theta(\rho, \tau_r)}{\partial \rho} \Big|_{\rho=\rho_m(\tau_r)} &= \left[\frac{\lambda(R_{\max} - 1)^2 r_1^2}{k_{\text{UE}}(T_s - T_m) t_{r,\max}} \right] \frac{d\rho_m(\tau_r)}{d\tau_r} \\
&= \left[\frac{(R_{\max} - 1)^2}{\frac{R_{\max}^2}{2} \ln(R_{\max}) - \frac{R_{\max}^2}{4} + \frac{1}{4}} \right] \frac{d\rho_m(\tau_r)}{d\tau_r}.
\end{aligned} \tag{7.3.1}$$

Substituting the derivative of $\theta(\rho, \tau_r)$ from Eq. (2.13) into the left-hand side of Eq. (7.3.1) results in

$$\begin{aligned}
\int_0^{\tau_r} d\tau'_r &= \frac{R_{\min}^2}{(GR_{\min} - H) \left[\frac{R_{\max}^2}{2} \ln(R_{\max}) - \frac{R_{\max}^2}{4} + \frac{1}{4} \right]} \\
&\times \left\{ \int_0^{\rho_m} d\rho'_m (1 + \rho'_m R_{\min}) \right. \\
&\times \left. \left[\ln(1 + \rho'_m R_{\min}) - \ln\left(\frac{G}{H} \rho'_m + 1\right) \right] \right\}.
\end{aligned} \tag{7.3.2}$$

Then, the reciprocal of τ_r in Eq. (7.3.2) with $\rho_m = 1$ and $R_m = R_{\max}$ is defined as the enhancement ratio in Eq. (2.16). Under the conservation of average volume fraction of mesh, we eliminate G and work $\kappa(\rho)$ as a function of H and R_{\max} (Eq. (2.20)) to obtain the enhancement ratio as a function of H and R_{\max} in Eq. (2.21).

7.4. Derivation of the maximum melting time ($t_{\text{sp,max}}$)

The maximum melting time is the time for the melting front to reach $r_m = r_2$ ($t = t_{\text{sp,max}}$) in 1-D spherical coordinates. The maximum melting time for uniform mesh (k_{UE}) is determined when k_{UE} is substituted for $k(r)$ in Eqs. (3.1) and (3.2). The temporal temperature distribution in 1-D spherical coordinates $T(r, t) = T_s + (T_m - T_s) (1/r_1 - 1/r) / (1/r_1 - 1/r_m)$, where r_m is a function of time, is substituted into Eq. (3.2) as

$$k_{\text{UE}} \left(\frac{T_s - T_m}{1/r_1 - 1/r_m} \right) \frac{1}{r^2} \Big|_{r=r_m} = \lambda \frac{dr_m}{dt}, \quad (7.4.1)$$

and $t_{\text{sp,max}}$ is acquired by integration as

$$\int_0^{t_{\text{sp,max}}} dt = \int_{r_1}^{r_2} dr_m \left(\frac{r_m^2}{r_1} - r_m \right) \left[\frac{\lambda}{k_{\text{UE}}(T_s - T_m)} \right]. \quad (7.4.2)$$

7.5. Derivation of the numerical solution in the dimensionless form

The normalized melting front position $\rho_{\text{sp,m}}$ is discretized as $\rho_{\text{sp,m},i} = (i - 1)\Delta\rho_{\text{sp}}$ where $\Delta\rho_{\text{sp}} = 1/N$ and the node index i ranges from 1 to $N + 1$. Since the discretized temporal melting front is known to progress from $\rho_{\text{sp,m},i=1} = 0$ and end at $\rho_{\text{sp,m},i=N+1} = 1$, the cumulative melting time $\tau_{\text{sp},i} = \tau_{\text{sp},i-1} + \Delta\tau_{\text{sp},i}$ is determined based on the associated time step $\Delta\tau_{\text{sp},i}$ from node $i - 1$ to node i .

After the first analytical integration, Eq. (3.5)(3.4) becomes

$$(1 + \rho_{\text{sp}}R_{\text{min}})^2 \kappa(\rho_{\text{sp}}) \frac{\partial\theta(\rho_{\text{sp}}, \tau_{\text{sp}})}{\partial\rho_{\text{sp}}} = C_{\text{int},i}, \quad (7.5.1)$$

where $C_{\text{int},i}$ is the integration constant for node i . This integration constant is then acquired using numerical integration as

$$\begin{aligned} C_{\text{int},i} &= \frac{\int_{\theta(\rho_{\text{sp}}=0, \tau_{\text{sp}})=1}^{\theta(\rho_{\text{sp}}=\rho_{\text{sp,m},i}, \tau_{\text{sp}})=0} d\theta}{\int_0^{\rho_{\text{sp,m},i}} \frac{d\rho_{\text{sp}}}{(1 + \rho_{\text{sp}}R_{\text{min}})^2 \kappa(\rho_{\text{sp}})}} \\ &= \frac{-1}{\int_0^{\rho_{\text{sp,m},i}} \frac{d\rho_{\text{sp}}}{(1 + \rho_{\text{sp}}R_{\text{min}})^2 \kappa(\rho_{\text{sp}})}}. \end{aligned} \quad (7.5.2)$$

The constant $C_{\text{int},i}$ is numerically integrated at each node.

The time step $\Delta\rho_{\text{sp},i=n}$ is acquired by substituting $\kappa(\rho_{\text{sp}})[\partial\theta(\rho_{\text{sp}},\tau_{\text{sp}})/\partial\rho_{\text{sp}}] = C_{\text{int},i}/(1 + \rho_{\text{sp}}R_{\text{min}})^2$ from Eq. (7.5.1) into Eq. (3.5) and then discretizing to reach

$$\Delta\tau_{\text{sp},i} \approx \left(\frac{6R_{\text{min}}^2}{2R_{\text{max}}^3 - 3R_{\text{max}}^2 + 1} \right) \frac{(1 + \rho_{\text{sp},m,i} R_{\text{min}})^2}{C_{\text{int},i}} \Delta\rho_{\text{sp}}. \quad (7.5.3)$$

The cumulative melting time $\Delta\tau_{\text{sp},i}$ is acquired from explicit forward time marching

$$\tau_{\text{sp},i} = \tau_{\text{sp},i-1} + \Delta\tau_{\text{sp},i}, \quad (7.5.4)$$

where $\tau_{\text{sp},i=1} = 0$ represents the initial condition. The reciprocal of $\tau_{\text{sp},i=N+1} = 1$ is the enhancement ratio.

7.6. Derivation of the coefficients $C_{\text{ev},i}$ in Eq. (3.9)

From Eq. (3.3), the volume fraction of metal mesh in k_{SE} is $v'_{\text{Mesh}} = [\kappa(\rho_{\text{sp}})k_{\text{UE}} - k_{\text{PCM}}]/\Delta k$, where $\Delta k = k_{\text{Mesh}} - k_{\text{PCM}}$. By utilizing $\Delta r = r_2 - r_1$, $r = r_1 + \Delta r\rho_{\text{sp}}$ and $dr = \Delta r d\rho_{\text{sp}}$ the conservation of metal volume fraction $\bar{v}'_{\text{Mesh}}(r) = \left[\int_{r_1}^{r_2} 4\pi r^2 v'_{\text{Mesh}}(r) dr \right] / [4\pi(r_2^3 - r_1^3)/3] = v_{\text{Mesh}}$ takes the form

$$\begin{aligned} \bar{v}'_{\text{Mesh}}(r) &= \frac{3 \int_0^1 \Delta r (r_1 + \Delta r \rho_{\text{sp}})^2 v'_{\text{Mesh}} d\rho_{\text{sp}}}{(r_2^3 - r_1^3)} \\ &= \frac{3 \int_0^1 \Delta r (r_1 + \Delta r \rho_{\text{sp}})^2 \left[\kappa(\rho_{\text{sp}}) \frac{k_{\text{UE}}}{\Delta k} - \frac{k_{\text{PCM}}}{\Delta k} \right] d\rho_{\text{sp}}}{(r_2^3 - r_1^3)} \\ &= v_{\text{Mesh}} = \frac{k_{\text{UE}}}{\Delta k} - \frac{k_{\text{PCM}}}{\Delta k}. \end{aligned} \quad (7.7.1)$$

Eq. (3.3) is substituted for $\kappa(\rho_{\text{sp}})$ in Eq. (7.7.1). Eq. (7.7.1) can be rearranged as

$$\begin{aligned} \frac{k_{\text{UE}}}{\Delta k} - \frac{k_{\text{PCM}}}{\Delta k} &= \frac{3(R_{\text{max}} - 1)}{R_{\text{max}}^3 - 1} \left(\frac{k_{\text{UE}}}{\Delta k} \right) \\ &\times \left\{ \sum_{i=0}^{i=n} \left[\frac{(R_{\text{max}} - 1)^2}{i + 3} + \frac{2(R_{\text{max}} - 1)}{i + 2} + \frac{1}{i + 1} \right] C_i \right\} \\ &- \frac{k_{\text{PCM}}}{\Delta k}. \end{aligned} \quad (7.7.2)$$

Furthermore, $k_{\text{UE}}/\Delta k$ and $k_{\text{PCM}}/\Delta k$ in Eq. (7.7.2) are cancelled as

$$\begin{aligned} 1 &= \frac{3(R_{\text{max}} - 1)}{R_{\text{max}}^3 - 1} \\ &\times \left\{ \sum_{i=0}^{i=n} \left[\frac{(R_{\text{max}} - 1)^2}{i + 3} + \frac{2(R_{\text{max}} - 1)}{i + 2} + \frac{1}{i + 1} \right] C_i \right\} \\ &= \sum_{i=0}^{i=n} C_{\text{CV},i} C_i. \end{aligned} \quad (7.7.3)$$

Finally, by comparison with Eq. (3.8) we find,

$$C_{\text{CV},i} = \left[\frac{(R_{\text{max}} - 1)^2}{i + 3} + \frac{2(R_{\text{max}} - 1)}{i + 2} + \frac{1}{i + 1} \right] \frac{3(R_{\text{max}} - 1)}{R_{\text{max}}^3 - 1}. \quad (7.7.4)$$

7.7. Equations and parameters in 1-D cylindrical coordinates

In 1-D cylindrical coordinates [97], the heat diffusion equation and energy balance at the melting front take the form

$$\frac{1}{r} \frac{\partial}{\partial r} \left[rk(r) \frac{\partial T(r, t)}{\partial r} \right] = 0, \quad (7.8.1)$$

$$-k(r) \frac{\partial T(r, t)}{\partial r} \Big|_{r=r_m(t)} = \lambda \frac{dr_m(t)}{dt}. \quad (7.8.2)$$

Eqs. (7.8.1) and (7.8.2) are nondimensionalized using the terms from Ref. [97] as

$$\frac{1}{(1 + \rho R_{\min})} \frac{\partial}{\partial \rho} \left[(1 + \rho R_{\min}) \kappa(\rho) \frac{\partial \theta(\rho, \tau_r)}{\partial \rho} \right] = 0. \quad (7.8.3)$$

$$\begin{aligned} & -\kappa(\rho) \frac{\partial \theta(\rho, \tau_r)}{\partial \rho} \Big|_{\rho=\rho_m(\tau_r)} \\ & = \left[\frac{(R_{\max} - 1)^2}{\frac{R_{\max}^2}{2} \ln(R_{\max}) - \frac{R_{\max}^2}{4} + \frac{1}{4}} \right] \frac{d\rho_m(\tau_r)}{d\tau_r}. \end{aligned} \quad (7.8.4)$$

Then, the enhancement ratio ($\epsilon_r = 1/\tau_{r,\max}$) is numerically solved using Eqs (7.8.3) and (7.8.4) based on the procedures in section 7.5 and Eq. (3.6).

In Eq. (3.10), $\Delta\kappa$ cylindrical coordinates is obtained using the conservation of metal volume fraction $\bar{v}'_{\text{Mesh}}(r) = \left[\int_{r_1}^{r_2} 2\pi r v'_{\text{Mesh}}(r) dr \right] / [\pi(r_2^2 - r_1^2)] = v_{\text{Mesh}}$ as

$$\Delta\kappa = \frac{1 - \kappa_{\min}}{\frac{2(R_{\max} - 1)}{R_{\max}^2 - 1} \left[\frac{R_{\max}}{n+1} - \frac{R_{\min}}{n+2} \right]}. \quad (7.8.5)$$

7.8. Uncertainty analysis

The uncertainty δk in the measured thermal conductivity k is estimated based on the uncertainty of each independent variable δj in Eq. (4.3) as

$$\delta k = \sqrt{\sum (\delta k_j)^2}, \quad \delta k_j = \frac{\partial k}{\partial j} \delta \quad (7.9.1)$$

$$j = I, R_0, V, \beta_{\text{ref}}, L,$$

where k takes the form using Eqs. (4.2) and (4.3) as

$$k = \frac{q'/4\pi}{d(\Delta T)/d(\ln t)} = \frac{I^2 R_0 V_{\text{ref}} \beta_{\text{ref}}}{4\pi L [d(\Delta V)/d(\ln t)]} \quad (7.9.2)$$

where $\Delta R/R_{\text{ref}} = \Delta V/V_{\text{ref}}$ in Eq. (4.2) and $V_{\text{ref}} = IR_{\text{ref}}$. The relative uncertainty can be estimated by dividing Eq. (7.9.1) by k as

$$\frac{\delta k}{k} = \sqrt{\sum \left(\frac{\delta k_j}{k} \right)^2}. \quad (7.9.3)$$

For instance, relative uncertainty of one Inconel 718 measurement listed in Table 7.1 indicates the uncertainty is mainly from temperature coefficient $\delta k_{j=\beta_{\text{ref}}}/k = 4.59\%$, and the overall uncertainty $\delta k/k$ is 5.42%.

Table 7.1 Uncertainty of each independent variable in the transient hot wire method from one Inconel 718 measurement

Parameter, j	δj	$\delta k_j/k$ (%)
Current, I	0.15 mA	0.63
Resistance, R_0	0.09 ohm	0.63
Voltage, V	1.14×10^{-5} V	3.17×10^{-3}
Temperature coefficient, β_{ref}	1.71×10^{-4} K ⁻¹	4.59
Length of a Pt wire, L	2 mm	2.74

7.9. Simulation of a melting process of paraffin in a vertical cylinder

7.9.1. Introduction

In our preliminary study, a PCM (octadecane) charge process was experimentally carried out. As shown in Figure 7.2, octadecane in the cylindrical cavity is heated by a Pt wire of 25.4 μm in diameter. The melting of octadecane near to the top end was faster than that near to the bottom. This indicates a non-uniform melting process. The height and radius of the cavity are 0.2 m and

0.015 m. The melting temperature of octadecane is 302.15 K. These parameters are utilized in our simulation introduced in section 7.9.2.

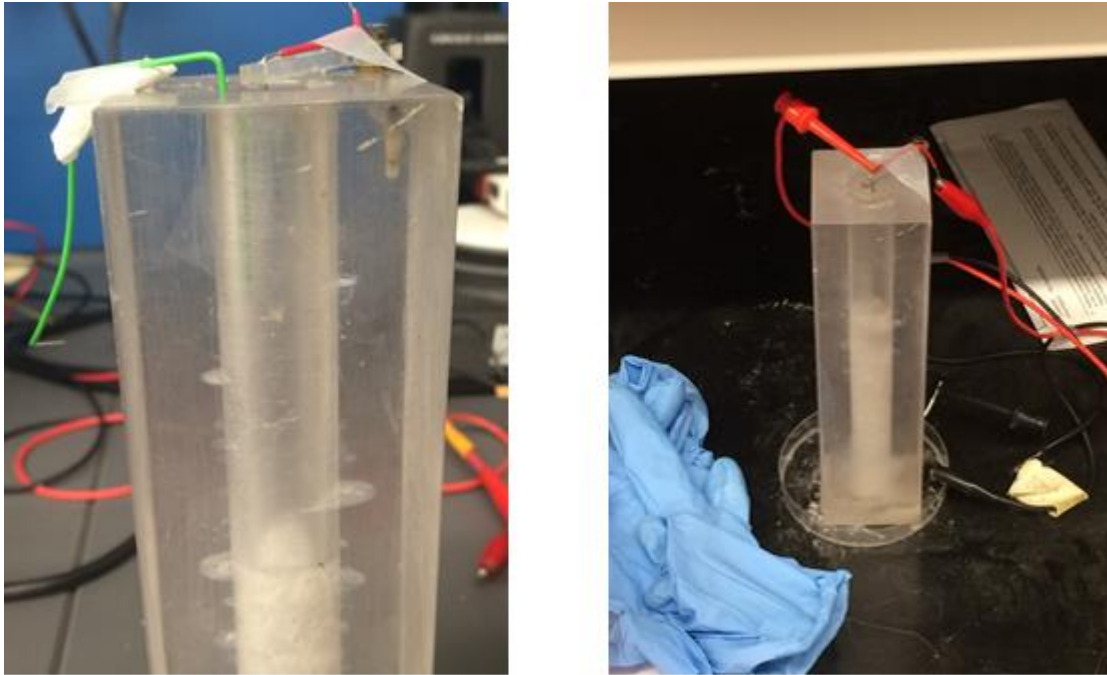


Figure 7.2 Octadecane in the cylindrical cavity is heated by a Pt wire of 25.4 μm in diameter. The melting of Octadecane near to the top end was faster than that near to the bottom. This indicates a non-uniform melting process.

7.9.2. Parameters in COMSOL

This simulation was carried out using the commercial CFD package, COMSOL. The parameters and settings are presented as screenshots as follows.

As shown in Figure 7.3, the dimension of the cylindrical cavity in the COMSOL setting/parameters menu includes the radius of the cylinder ($r_{\text{top}} = r_{\text{bottom}} = 0.015 \text{ m}$), the height ($H_g = 0.2 \text{ m}$), and the radius of the Pt wire heater ($r_{\text{heater}} = 1.27 \mu\text{m}$). The cross-sectional view of the cylindrical cavity is shown in Figure 7.4. The computation domain has 2-D symmetry due to

the radial symmetry in the cavity. This setting is cost-effective way with regard to computation time.

Settings

Parameters

Parameters

Name	Expression	Value	Description
r_top	1.5[cm]	0.015 m	Radius of the top
r_bottom	1.5[cm]	0.015 m	Radius of the bottom
Hg	20[cm]	0.2 m	Height of the glass
r_heater	1.27e-6[m]	1.27E-6 m	radius of the Pt heater
element_s	0.001[m]	0.001 m	
Tm	302.15[K]	302.15 K	Melting temp of Octadec...

Figure 7.3 The settings/parameters menu showing the physical dimension and properties for the simulation.

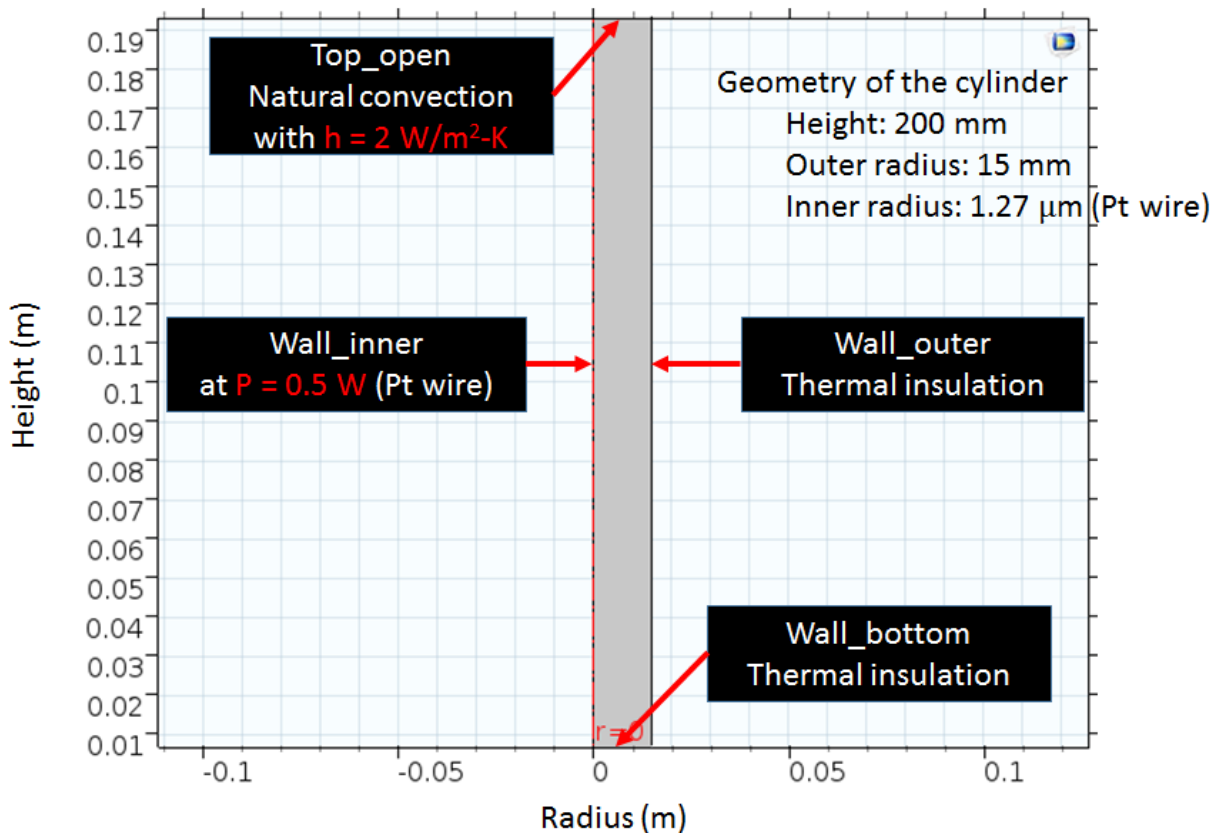


Figure 7.4 Schematic of the cross-sectional view of the cylindrical cavity and corresponding boundary conditions. The bottom and outer walls are made of thermally-insulating Acrylic (i.e., PMMA), whereas the top is open to the surrounding air with a weak natural convection heat transfer coefficient of 2 W/m-K.

The boundary conditions are shown in Figure 7.3. The bottom and outer walls are made of thermally-insulating Acrylic (i.e., PMMA), whereas the top is open to the surrounding air with a weak natural convection heat transfer coefficient of 2 W/m-K. The Pt wire is maintained at a uniform temperature of 313.15 K as the heater.

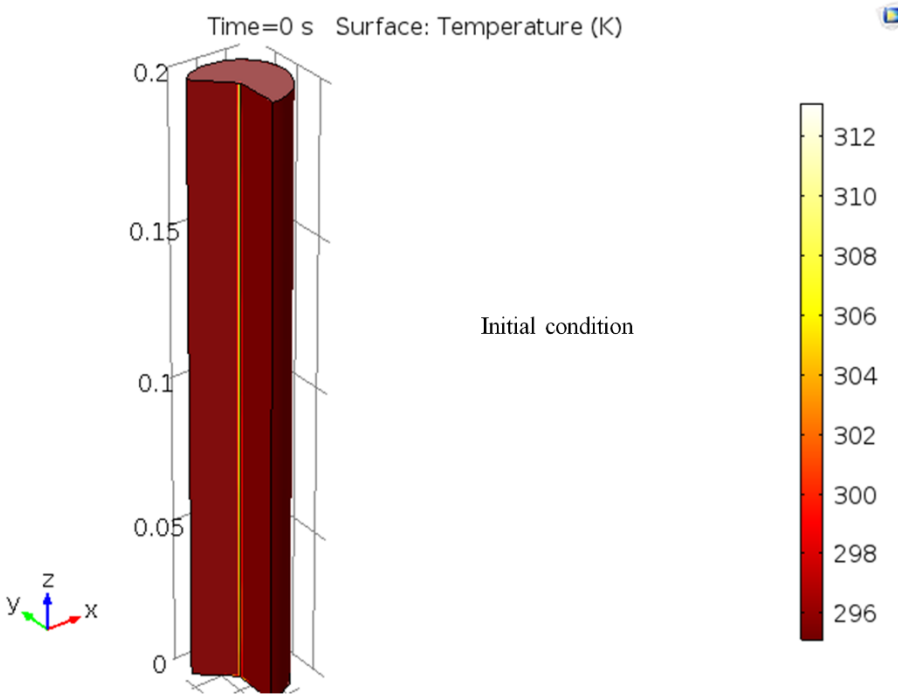


Figure 7.5 Settings of the initial condition at 295 K for the simulation.

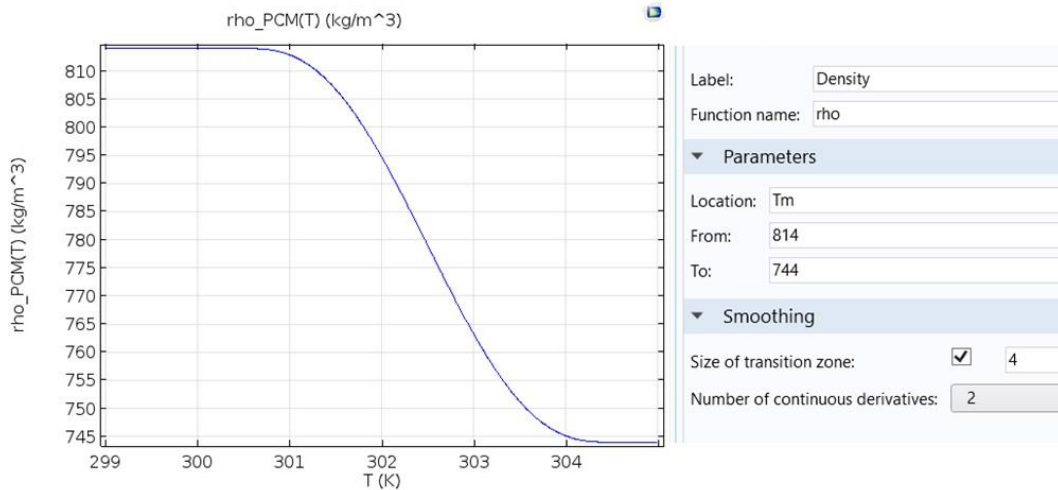


Figure 7.6 The density of octadecane changes from 814 kg/m³ to 744 kg/m³ (from solid to liquid phase) [221].

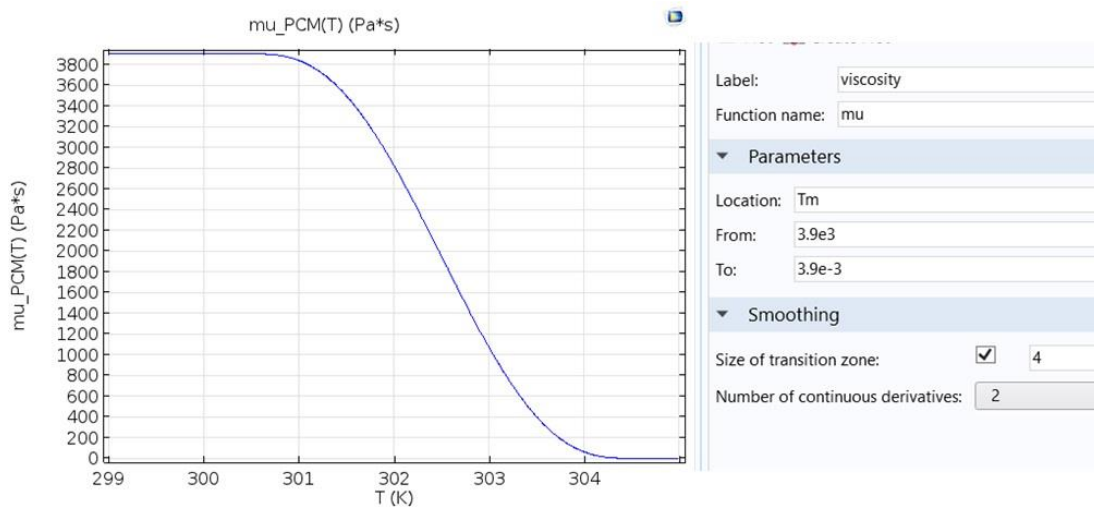


Figure 7.7 The viscosity of octadecane changes from 3.9×10^3 Pa*s [221] to 3.9×10^{-3} Pa*s (from solid to liquid phase). Note the viscosity of the solid phase is set six orders of magnitude higher than that of the liquid phase so as to approximate nearly as a solid.

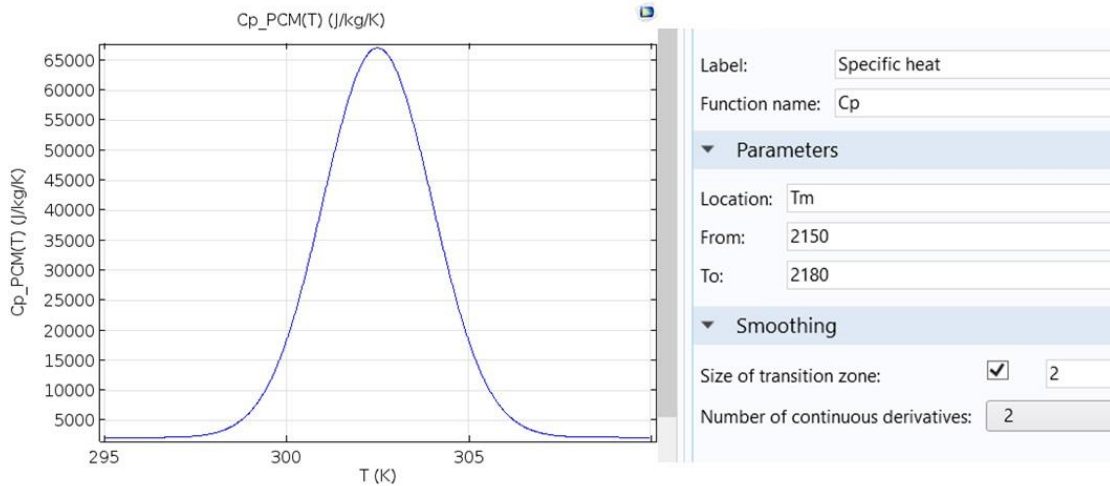


Figure 7.8 The effective specific heat varies from 2150 J/kg-K to 2180 J/kg-K (from solid to liquid phase). The latent heat of fusion is approximated as the integration of the effective specific heat versus temperature from 298 to 307 K, which is close to the latent heat of 244000 J/kg [221].

The initial condition at 295 K for the simulation and the PCM properties (i.e., octadecane in this case) are shown in Figure 7.5-Figure 7.8. Since octadecane is melted at T_m during the charge process, the change of the temperature-dependent properties, such as dynamic viscosity and density, indicates the change of octadecane from solid to liquid phase, as shown in Figure 7.6 and Figure 7.7. For the latent heat of fusion of the PCM, we utilized an effective specific heat to account for the latent heat of fusion for the melting [222]. Mathematically, the integration of the effective specific heat versus temperature is equivalent to the latent heat of fusion. Physically, the spike centering at $T_m = 302.15$ K in Figure 7.5 implies that the latent heat of fusion occurring at T_m is approximated as the sensible heat absorbed by the PCM over the temperature range from $T_m \pm 2$ K.

7.9.3. Results

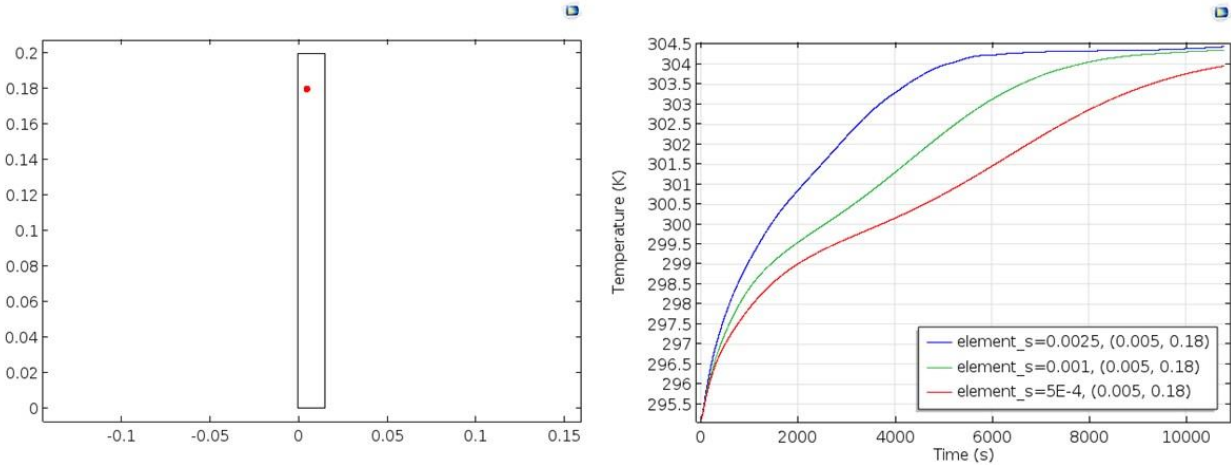


Figure 7.9 The local temperatures, located at coordinates $(r, h) = (0.005, 0.18)$ marked with a red dot, are samples for three different mesh sizes (0.0025 m, 0.001 m, and 0.0005 m). The temperature versus time points out a distinct difference among the three cases.

To ensure the accuracy of the simulation, we test different mesh sizes. We seek to find the mesh size where the temperature distribution converges, such that smaller mesh sizes give the same values. As shown in Figure 7.9, the local temperatures, located at coordinates $(r, h) = (0.005, 0.18)$ marked with a red dot, are samples for three different mesh sizes (0.0025 m, 0.001 m, and 0.0005 m). The temperature versus time data indicates a distinct difference among the three cases (e.g., a maximum difference of 1 K at $t = 4000$ sec between 0.0025 m and 0.001 m). This test result concludes that multiple cases with mesh sizes finer than 0.0005 m are needed until the maximum temperature difference between cases is smaller than 0.1 K.

The 3-D plot of temperature field and the melting front as the blue line are in Figure 7.10. Although the accuracy of our current simulation needs to be improved, the results qualitatively point out that the melting is similarly faster near to the top of the cavity. These melting front positions agree with the observation of our preliminary experiment shown in Figure 7.2. Furthermore, the red arrows in Figure 7.11 represent the direction and logarithmic-scale magnitude

of the velocity field as at 10800 sec after the melting begins. The higher flow velocity (larger arrow) results from the gravity-buoyancy driven natural convection.

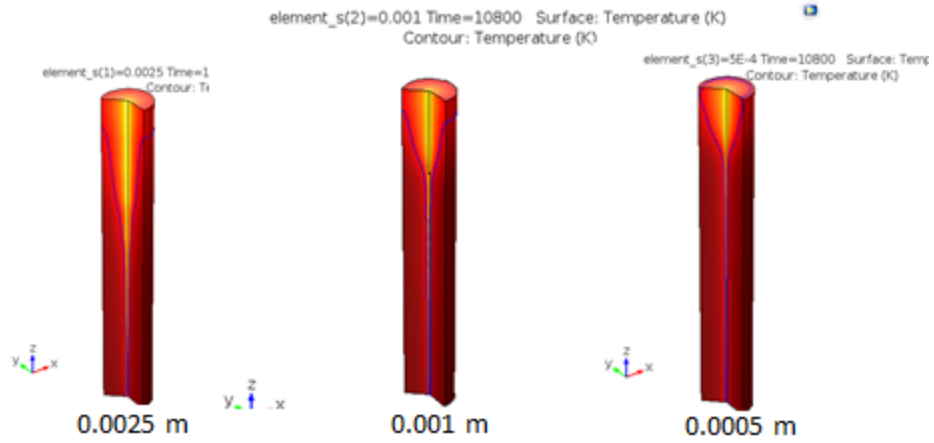


Figure 7.10 Schematics of the 3-D plot of temperature field at 10800 sec after the melting begins.

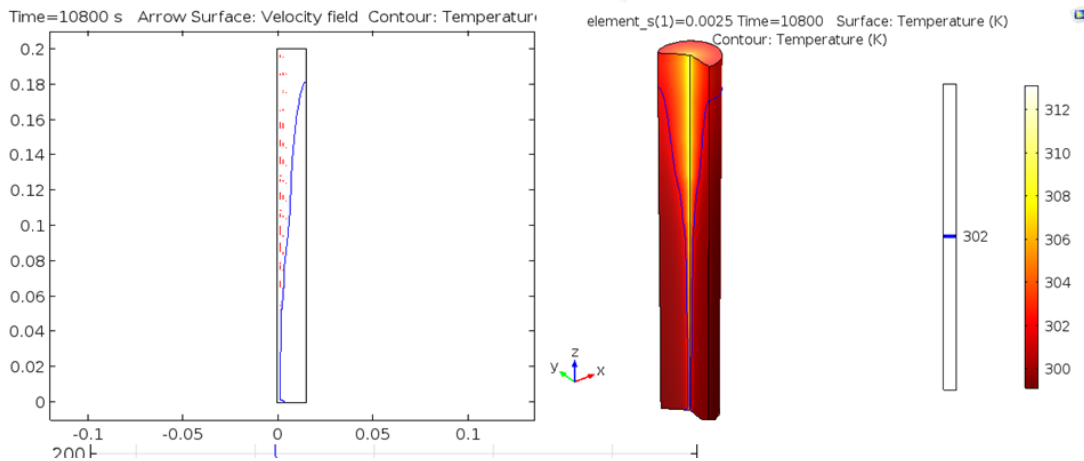


Figure 7.11 Schematics of the melting front and the 3-D plot of temperature and flow velocity fields (mesh size is 0.0025 m). The blue line is the melting front position at 10800 sec after the melting begins. The red arrows indicate the direction and logarithmic-scale magnitude of the flow velocity in the melted region. The higher flow velocity takes places due to natural convection.

7.9.4. Outlook

This work demonstrates the charge process of the PCM and the groundwork for simulations of phase change in mesh/PCM composites. The appropriate mesh sizes may need to be reduced to 0.0001 m. Furthermore, the Pt wire may be modified to generate heat with a constant power, which approximates well the realistic situation of the Pt wire. While the heat rate of the Pt wire is constant, the axial-temperature distribution tends to be non-uniform because the small radius of the Pt wire results in high axial thermal resistance. In addition, nonequilibrium thermal transport between mesh and PCM is another potential area to study in simulation [45].

8. References

1. Waghmare, A.V. and A.T. Pise, *Numerical Investigation of Concentric Cylinder Latent Heat Storage with / without Gravity and Buoyancy*. Energy Procedia, 2015. **75**: p. 3133-3141.
2. Tiari, S., S. Qiu, and M. Mahdavi, *Numerical study of finned heat pipe-assisted thermal energy storage system with high temperature phase change material*. Energy Conversion and Management, 2015. **89**: p. 833-842.
3. Malan, D.J., R.T. Dobson, and F. Dinter, *Solar Thermal Energy Storage in Power Generation Using Phase Change Material with Heat Pipes and Fins to Enhance Heat Transfer*. Energy Procedia, 2015. **69**: p. 925-936.
4. Gu, X., J. Niu, and S. Qin, *Antarcticite: A Phase Change Material for Thermal Energy Storage—Experiments and Simulation*, in *Proceedings of the 11th International Congress for Applied Mineralogy (ICAM)*, F. Dong, Editor. 2015, Springer International Publishing: Cham. p. 125-135.
5. Delgado, M., et al., *Experimental analysis of a low cost phase change material emulsion for its use as thermal storage system*. Energy Conversion and Management, 2015. **106**: p. 201-212.
6. de Gracia, A. and L.F. Cabeza, *Phase change materials and thermal energy storage for buildings*. Energy and Buildings, 2015. **103**: p. 414-419.
7. Kuravi, S., et al., *Thermal energy storage technologies and systems for concentrating solar power plants*. Progress in Energy and Combustion Science, 2013. **39**(4): p. 285-319.
8. Oró, E., et al., *Review on phase change materials (PCMs) for cold thermal energy storage applications*. Applied Energy, 2012. **99**(0): p. 513-533.
9. Agyenim, F., et al., *A review of materials, heat transfer and phase change problem formulation for latent heat thermal energy storage systems (LHTESS)*. Renewable and Sustainable Energy Reviews, 2010. **14**(2): p. 615-628.
10. Agyenim, F., P. Eames, and M. Smyth, *Heat transfer enhancement in medium temperature thermal energy storage system using a multitube heat transfer array*. Renewable Energy, 2010. **35**(1): p. 198-207.
11. Sharma, A., et al., *Review on thermal energy storage with phase change materials and applications*. Renewable and Sustainable Energy Reviews, 2009. **13**(2): p. 318-345.
12. Rao, Z. and S. Wang, *A review of power battery thermal energy management*. Renewable and Sustainable Energy Reviews, 2011. **15**(9): p. 4554-4571.
13. Anandan, S.S. and V. Ramalingam, *Thermal management of electronics: A review of literature*. Thermal science, 2008. **12**(2): p. 5-26.
14. Garimella, S.V., *Advances in mesoscale thermal management technologies for microelectronics*. Microelectronics Journal, 2006. **37**(11): p. 1165-1185.
15. Huang, H., et al., *Aligned Carbon Nanotube Composite Films for Thermal Management*. Advanced Materials, 2005. **17**(13): p. 1652-1656.
16. Moore, A.L. and L. Shi. *Emerging challenges and materials for thermal management of electronics*. Materials Today [0]; Available from: <http://www.sciencedirect.com/science/article/pii/S1369702114001138>.
17. Humphreys, C.J., *Solid-State Lighting*. MRS Bulletin, 2011. **33**(4): p. 459-470.
18. Krames, M.R., et al., *Status and Future of High-Power Light-Emitting Diodes for Solid-State Lighting*. Journal of Display Technology, 2007. **3**(2): p. 160-175.
19. D'Andrade, B.W. and S.R. Forrest, *White Organic Light-Emitting Devices for Solid-State Lighting*. Advanced Materials, 2004. **16**(18): p. 1585-1595.
20. Zukauskas, A., M.S. Shur, and R. Gaska, *Introduction to solid-state lighting*. Vol. 122. 2002: John Wiley & Sons New York.

21. Steigerwald, D.A., et al., *Illumination with solid state lighting technology*. IEEE Journal of Selected Topics in Quantum Electronics, 2002. **8**(2): p. 310-320.
22. Arik, M., J. Petroski, and S. Weaver. *Thermal challenges in the future generation solid state lighting applications: light emitting diodes*. in *ITherm 2002. Eighth Intersociety Conference on Thermal and Thermomechanical Phenomena in Electronic Systems (Cat. No.02CH37258)*. 2002.
23. Siddique, A.R.M., S. Mahmud, and B.V. Heyst, *A review of the state of the science on wearable thermoelectric power generators (TEGs) and their existing challenges*. Renewable and Sustainable Energy Reviews, 2017. **73**: p. 730-744.
24. Champier, D., *Thermoelectric generators: A review of applications*. Energy Conversion and Management, 2017. **140**: p. 167-181.
25. Zhang, H., et al., *Bi1-xSbx Alloy Nanocrystals: Colloidal Synthesis, Charge Transport, and Thermoelectric Properties*. ACS Nano, 2013. **7**(11): p. 10296-10306.
26. Yu, J.K., S. Mitrovic, and J.R. Heath, *Nanomesh phononic structures for low thermal conductivity and thermoelectric energy conversion materials*, 2013, Google Patents.
27. Tritt, T.M., *Thermoelectric Phenomena, Materials, and Applications*. Annual Review of Materials Research, 2011. **41**(1): p. 433-448.
28. *Thermoelectrics handbook; macro to nano*, in *Scitech Book News2006*, Ringgold Inc: Portland.
29. Telkes, M. and E. Raymond, *Storing solar heat in chemicals*. Heat. Vent.;(), 1949. **46**.
30. Telkes, M., *Thermal energy storage in salt hydrates*. Solar Energy Materials, 1980. **2**(4): p. 381-393.
31. Duffie, J.A. and W.A. Beckman, *Solar engineering of thermal processes*. 1980.
32. Abhat, A., *Low temperature latent heat thermal energy storage: Heat storage materials*. Solar Energy, 1983. **30**(4): p. 313-332.
33. Voller, V., *Fast implicit finite-difference method for the analysis of phase change problems*. Numerical Heat Transfer, 1990. **17**(2): p. 155-169.
34. Pincemin, S., et al., *Highly conductive composites made of phase change materials and graphite for thermal storage*. Solar Energy Materials and Solar Cells, 2008. **92**(6): p. 603-613.
35. Tatsidjodoung, P., N. Le Pierrès, and L. Luo, *A review of potential materials for thermal energy storage in building applications*. Renewable and Sustainable Energy Reviews, 2013. **18**: p. 327-349.
36. Fan, L. and J.M. Khodadadi, *Thermal conductivity enhancement of phase change materials for thermal energy storage: A review*. Renewable and Sustainable Energy Reviews, 2011. **15**(1): p. 24-46.
37. Dutil, Y., et al., *A review on phase-change materials: Mathematical modeling and simulations*. Renewable and Sustainable Energy Reviews, 2011. **15**(1): p. 112-130.
38. Jegadheeswaran, S. and S.D. Pohekar, *Performance enhancement in latent heat thermal storage system: A review*. Renewable and Sustainable Energy Reviews, 2009. **13**(9): p. 2225-2244.
39. Khudhair, A.M. and M.M. Farid, *A review on energy conservation in building applications with thermal storage by latent heat using phase change materials*. Energy Conversion and Management, 2004. **45**(2): p. 263-275.
40. Farid, M.M., et al., *A review on phase change energy storage: materials and applications*. Energy Conversion and Management, 2004. **45**(9-10): p. 1597-1615.
41. Zalba, B., et al., *Review on thermal energy storage with phase change: materials, heat transfer analysis and applications*. Applied Thermal Engineering, 2003. **23**(3): p. 251-283.
42. Wang, J., et al., *A new approach to modelling the effective thermal conductivity of heterogeneous materials*. International Journal of Heat and Mass Transfer, 2006. **49**(17-18): p. 3075-3083.
43. Krishnan, S., et al., *Towards a Thermal Moore's Law*. IEEE Transactions on Advanced Packaging, 2007. **30**(3): p. 462-474.

44. Krishnan, S., S.V. Garimella, and S.S. Kang, *A novel hybrid heat sink using phase change materials for transient thermal management of electronics*. IEEE Transactions on Components and Packaging Technologies, 2005. **28**(2): p. 281-289.
45. Krishnan, S., J.Y. Murthy, and S.V. Garimella, *A Two-Temperature Model for Solid-Liquid Phase Change in Metal Foams*. Journal of Heat Transfer, 2004. **127**(9): p. 995-1004.
46. Krishnan, S. and S.V. Garimella, *Analysis of a phase change energy storage system for pulsed power dissipation*. IEEE transactions on components and packaging technologies, 2004. **27**(1): p. 191-199.
47. Tomizawa, Y., et al., *Experimental and numerical study on phase change material (PCM) for thermal management of mobile devices*. Applied Thermal Engineering, 2016. **98**: p. 320-329.
48. Wang, Z., et al., *Paraffin and paraffin/aluminum foam composite phase change material heat storage experimental study based on thermal management of Li-ion battery*. Applied Thermal Engineering, 2015. **78**: p. 428-436.
49. Lin, C., et al., *Experiment and simulation of a LiFePO₄ battery pack with a passive thermal management system using composite phase change material and graphite sheets*. Journal of Power Sources, 2015. **275**: p. 742-749.
50. Lee, K.O., et al., *Assessing the integration of a thin phase change material (PCM) layer in a residential building wall for heat transfer reduction and management*. Applied Energy, 2015. **137**: p. 699-706.
51. Ling, Z., et al., *Review on thermal management systems using phase change materials for electronic components, Li-ion batteries and photovoltaic modules*. Renewable and Sustainable Energy Reviews, 2014. **31**: p. 427-438.
52. Weinstein, R.D., et al., *The Experimental Exploration of Embedding Phase Change Materials With Graphite Nanofibers for the Thermal Management of Electronics*. Journal of Heat Transfer, 2008. **130**(4): p. 042405-042405-8.
53. Tan, F.L. and S.C. Fok. *Thermal Management of Mobile Phone using Phase Change Material*. in *2007 9th Electronics Packaging Technology Conference*. 2007.
54. Hodes, M., et al., *Transient Thermal Management of a Handset Using Phase Change Material (PCM)*. Journal of Electronic Packaging, 2002. **124**(4): p. 419-426.
55. Vesligaj, M.J. and C.H. Amon, *Transient thermal management of temperature fluctuations during time varying workloads on portable electronics*. IEEE Transactions on Components and Packaging Technologies, 1999. **22**(4): p. 541-550.
56. Lipeng, C., et al., *Transient thermal management of portable electronics using heat storage and dynamic power dissipation control*. IEEE Transactions on Components, Packaging, and Manufacturing Technology: Part A, 1998. **21**(1): p. 113-123.
57. Wahid, M.A., et al., *An Overview of Phase Change Materials for Construction Architecture Thermal Management in Hot and Dry Climate Region*. Applied Thermal Engineering.
58. Moore, A.L. and L. Shi, *Emerging challenges and materials for thermal management of electronics*. Materials Today, 2014. **17**(4): p. 163-174.
59. Wang, P., et al., *Analytical modeling of silicon thermoelectric microcooler*. Journal of Applied Physics, 2006. **100**(1): p. 014501.
60. Huang, W., et al., *Scaling with Design Constraints: Predicting the Future of Big Chips*. IEEE Micro, 2011. **31**(4): p. 16-29.
61. Ferain, I., C.A. Colinge, and J.-P. Colinge, *Multigate transistors as the future of classical metal-oxide-semiconductor field-effect transistors*. Nature, 2011. **479**(7373): p. 310-316.
62. Fang, X., et al., *Increased Thermal Conductivity of Eicosane-Based Composite Phase Change Materials in the Presence of Graphene Nanoplatelets*. Energy & Fuels, 2013. **27**(7): p. 4041-4047.

63. Khodadadi, J.M., L. Fan, and H. Babaei, *Thermal conductivity enhancement of nanostructure-based colloidal suspensions utilized as phase change materials for thermal energy storage: A review*. Renewable and Sustainable Energy Reviews, 2013. **24**: p. 418-444.
64. *CRC Handbook of Chemistry and Physics, 86th Edition Edited by David R. Lide (National Institute of Standards and Technology)*. CRC Press (an imprint of Taylor and Francis Group): Boca Raton, FL. 2005. 2544 pp. \$125.96. ISBN 0-8493-0486-5. Journal of the American Chemical Society, 2006. **128**(16): p. 5585-5585.
65. O'Neil, M., et al., *éditeurs. The Merck Index: An Encyclopedia of Chemicals, Drugs, and Biologicals, 13 e édition*. Whitehouse Station (NJ): Merck & Co, 2001, Inc.
66. Sharma, S.D. and K. Sagara, *Latent heat storage materials and systems: A review*. International Journal of Green Energy, 2005. **2**(1): p. 1-56.
67. Abhat, A., *Short term thermal energy storage*. Revue de physique appliquee, 1980. **15**(3): p. 477-501.
68. Zhang, P., X. Xiao, and Z.W. Ma, *A review of the composite phase change materials: Fabrication, characterization, mathematical modeling and application to performance enhancement*. Applied Energy, 2016. **165**: p. 472-510.
69. Pereira da Cunha, J. and P. Eames, *Thermal energy storage for low and medium temperature applications using phase change materials – A review*. Applied Energy, 2016. **177**: p. 227-238.
70. Xu, B., P. Li, and C. Chan, *Application of phase change materials for thermal energy storage in concentrated solar thermal power plants: A review to recent developments*. Applied Energy, 2015. **160**: p. 286-307.
71. Kibria, M.A., et al., *A review on thermophysical properties of nanoparticle dispersed phase change materials*. Energy Conversion and Management, 2015. **95**: p. 69-89.
72. Ferrer, G., et al., *Review on the methodology used in thermal stability characterization of phase change materials*. Renewable and Sustainable Energy Reviews, 2015. **50**: p. 665-685.
73. Cui, Y., et al., *Review of Phase Change Materials Integrated in Building Walls for Energy Saving*. Procedia Engineering, 2015. **121**: p. 763-770.
74. Regin, A.F., S.C. Solanki, and J.S. Saini, *Heat transfer characteristics of thermal energy storage system using PCM capsules: A review*. Renewable and Sustainable Energy Reviews, 2008. **12**(9): p. 2438-2458.
75. Jankowski, N.R. and F.P. McCluskey, *A review of phase change materials for vehicle component thermal buffering*. Applied Energy, 2014. **113**: p. 1525-1561.
76. Zhai, X.Q., et al., *A review on phase change cold storage in air-conditioning system: Materials and applications*. Renewable and Sustainable Energy Reviews, 2013. **22**: p. 108-120.
77. Waqas, A. and Z. Ud Din, *Phase change material (PCM) storage for free cooling of buildings—A review*. Renewable and Sustainable Energy Reviews, 2013. **18**: p. 607-625.
78. Salunkhe, P.B. and P.S. Shembekar, *A review on effect of phase change material encapsulation on the thermal performance of a system*. Renewable and Sustainable Energy Reviews, 2012. **16**(8): p. 5603-5616.
79. Verma, P., Varun, and S.K. Singal, *Review of mathematical modeling on latent heat thermal energy storage systems using phase-change material*. Renewable and Sustainable Energy Reviews, 2008. **12**(4): p. 999-1031.
80. Karimi, G. and J.R. Culham. *Review and assessment of Pulsating Heat Pipe mechanism for high heat flux electronic cooling*. in *The Ninth Intersociety Conference on Thermal and Thermomechanical Phenomena In Electronic Systems (IEEE Cat. No.04CH37543)*. 2004.
81. Simons, R.E. and R.C. Chu. *Application of thermoelectric cooling to electronic equipment: a review and analysis*. in *Sixteenth Annual IEEE Semiconductor Thermal Measurement and Management Symposium (Cat. No.00CH37068)*. 2000.

82. Bergman, T.L., F.P. Incropera, and A.S. Lavine, *Fundamentals of Heat and Mass Transfer*. 2011: Wiley.
83. Sun, X., et al., *Experimental observations on the heat transfer enhancement caused by natural convection during melting of solid–liquid phase change materials (PCMs)*. *Applied Energy*, 2016. **162**: p. 1453-1461.
84. Mettawee, E.-B.S. and G.M.R. Assassa, *Thermal conductivity enhancement in a latent heat storage system*. *Solar Energy*, 2007. **81**(7): p. 839-845.
85. Cabeza, L.F., et al., *Heat transfer enhancement in water when used as PCM in thermal energy storage*. *Applied Thermal Engineering*, 2002. **22**(10): p. 1141-1151.
86. Fukai, J., et al., *Thermal conductivity enhancement of energy storage media using carbon fibers*. *Energy Conversion and Management*, 2000. **41**(14): p. 1543-1556.
87. Elgafy, A. and K. Lafdi, *Effect of carbon nanofiber additives on thermal behavior of phase change materials*. *Carbon*, 2005. **43**(15): p. 3067-3074.
88. Fan, L.-W., Z.-Q. Zhu, and M.-J. Liu, *A similarity solution to unidirectional solidification of nano-enhanced phase change materials (NePCM) considering the mushy region effect*. *International Journal of Heat and Mass Transfer*, 2015. **86**: p. 478-481.
89. Ji, H., et al., *Enhanced thermal conductivity of phase change materials with ultrathin-graphite foams for thermal energy storage*. *Energy & Environmental Science*, 2014. **7**(3): p. 1185-1192.
90. Yavari, F., et al., *Enhanced Thermal Conductivity in a Nanostructured Phase Change Composite due to Low Concentration Graphene Additives*. *The Journal of Physical Chemistry C*, 2011. **115**(17): p. 8753-8758.
91. Xia, M., et al., *Cold storage condensation heat recovery system with a novel composite phase change material*. *Applied Energy*, 2016. **175**: p. 259-268.
92. Humphries, W.R., Griggs, E. I., *A design handbook for phase change thermal control and energy storage devices*. NASA Technical paper 1977. **1074**: p. 256.
93. Lafdi, K., O. Mesalhy, and S. Shaikh, *Experimental study on the influence of foam porosity and pore size on the melting of phase change materials*. *Journal of Applied Physics*, 2007. **102**(8): p. 083549.
94. Mesalhy, O., K. Lafdi, and A. Elgafy, *Carbon foam matrices saturated with PCM for thermal protection purposes*. *Carbon*, 2006. **44**(10): p. 2080-2088.
95. Jiji, L.M., *Heat Conduction*. 2009: Springer Berlin Heidelberg.
96. Šarler, B., *Stefan's work on solid-liquid phase changes*. *Engineering Analysis with Boundary Elements*, 1995. **16**(2): p. 83-92.
97. Wei, L.C. and J.A. Malen, *Amplified charge and discharge rates in phase change materials for energy storage using spatially-enhanced thermal conductivity*. *Applied Energy*, 2016. **181**: p. 224-231.
98. Gibson, I., D.W. Rosen, and B. Stucker, *Additive manufacturing technologies*. Vol. 238. 2010: Springer.
99. Kruth, J.P., M.C. Leu, and T. Nakagawa, *Progress in Additive Manufacturing and Rapid Prototyping*. *CIRP Annals - Manufacturing Technology*, 1998. **47**(2): p. 525-540.
100. Coopers, P.W., *3D printing and the new shape of industrial manufacturing*, 2014.
101. Chua, C.K., K.F. Leong, and C.S. Lim, *Rapid prototyping: principles and applications*. 2010: World Scientific.
102. DEAN SIGLER, *Additive Manufacturing for Electric Motors*. 2013. <http://cafe.foundation/blog/additive-manufacturing-for-electric-motors/> (accessed 12 July 2017).
103. Santos, E., et al. *Mechanical properties of pure titanium models processed by selective laser melting*. in *Proceedings of the Solid Freeform Fabrication Symposium*. 2002.
104. Jones, M.G. *Direct laser sintering of metals*. DTIC Document.
105. Frazier, W.E., *Metal Additive Manufacturing: A Review*. *Journal of Materials Engineering and Performance*, 2014. **23**(6): p. 1917-1928.

106. Sears, J.W., *Direct laser powder deposition - 'State of the Art'*. Conference: ASTM/TMS Materials Week, Cincinnati, OH (US), 11/01/1999--11/04/1999; Other Information: PBD: 1 Nov 1999. 1999; ; Knolls Atomic Power Lab., Niskayuna, NY (US). Medium: P; Size: 16 pages.
107. Ehrlich, L.E., et al., *Large Thermal Conductivity Differences between the Crystalline and Vitriified States of DMSO with Applications to Cryopreservation*. PLoS ONE, 2015. **10**(5): p. e0125862.
108. Kestin, J. and W.A. Wakeham, *A contribution to the theory of the transient hot-wire technique for thermal conductivity measurements*. Physica A: Statistical Mechanics and its Applications, 1978. **92**(1–2): p. 102-116.
109. Healy, J.J., J.J. de Groot, and J. Kestin, *The theory of the transient hot-wire method for measuring thermal conductivity*. Physica B+C, 1976. **82**(2): p. 392-408.
110. De Groot, J.J., J. Kestin, and H. Sookiazian, *Instrument to measure the thermal conductivity of gases*. Physica, 1974. **75**(3): p. 454-482.
111. Jeffrey, D.J., *Conduction Through a Random Suspension of Spheres*. Proceedings of the Royal Society of London A: Mathematical, Physical and Engineering Sciences, 1973. **335**(1602): p. 355-367.
112. Xu, B., et al., *General volume sizing strategy for thermal storage system using phase change material for concentrated solar thermal power plant*. Applied Energy, 2015. **140**: p. 256-268.
113. Kenisarin, M. and K. Mahkamov, *Solar energy storage using phase change materials*. Renewable and Sustainable Energy Reviews, 2007. **11**(9): p. 1913-1965.
114. Medrano, M., et al., *Experimental evaluation of commercial heat exchangers for use as PCM thermal storage systems*. Applied Energy, 2009. **86**(10): p. 2047-2055.
115. Biswas, K., et al., *Combined experimental and numerical evaluation of a prototype nano-PCM enhanced wallboard*. Applied Energy, 2014. **131**: p. 517-529.
116. Mehling, H. and L.F. Cabeza, *Heat and cold storage with PCM: An up to date introduction into basics and applications*. 2008: Springer Berlin Heidelberg.
117. Kim, S. and L.T. Drzal, *High latent heat storage and high thermal conductive phase change materials using exfoliated graphite nanoplatelets*. Solar Energy Materials and Solar Cells, 2009. **93**(1): p. 136-142.
118. Schiffres, S.N., et al., *Tunable Electrical and Thermal Transport in Ice-Templated Multilayer Graphene Nanocomposites through Freezing Rate Control*. ACS Nano, 2013. **7**(12): p. 11183-11189.
119. Yin, H., et al., *Experimental research on heat transfer mechanism of heat sink with composite phase change materials*. Energy Conversion and Management, 2008. **49**(6): p. 1740-1746.
120. Wang, H., et al., *Experimental investigation on the thermal performance of a heat sink filled with porous metal fiber sintered felt/paraffin composite phase change material*. Applied Energy, 2016. **176**: p. 221-232.
121. Schuetz, M.A. and L.R. Glicksman, *A Basic Study of Heat Transfer Through Foam Insulation*. Journal of Cellular Plastics, 1984. **20**(2): p. 114-121.
122. Kruth, J.P., et al., *Consolidation phenomena in laser and powder-bed based layered manufacturing*. CIRP Annals - Manufacturing Technology, 2007. **56**(2): p. 730-759.
123. Murr, L.E., et al., *Metal Fabrication by Additive Manufacturing Using Laser and Electron Beam Melting Technologies*. Journal of Materials Science & Technology, 2012. **28**(1): p. 1-14.
124. Tarzia, D., *Explicit and Approximated Solutions for Heat and Mass Transfer Problems with a Moving Interface*, in: M. El-Amin (Ed.). Advanced Topics in Mass Transfer, InTech, 2011.
125. Nicolin Douglas, J., et al., *Numerical Solution of a Nonlinear Diffusion Model for Soybean Hydration with Moving Boundary*, in *International Journal of Food Engineering* 2015. p. 587-595.
126. Hill, J. and V. Hart, *The Stefan problem in nonlinear heat conduction*. Zeitschrift für angewandte Mathematik und Physik ZAMP, 1986. **37**(2): p. 206-229.

127. Rogers, C., *On a class of moving boundary problems in non-linear heat conduction: Application of a Bäcklund transformation*. International Journal of Non-Linear Mechanics, 1986. **21**(4): p. 249-256.
128. Rogers, C. and P. Broadbridge, *On a nonlinear moving boundary problem with heterogeneity: application of a reciprocal transformation*. Zeitschrift für angewandte Mathematik und Physik ZAMP, 1988. **39**(1): p. 122-128.
129. Natale, M.a.F. and D.A. Tarzia, *Explicit solutions to the one-phase Stefan problem with temperature-dependent thermal conductivity and a convective term*. International Journal of Engineering Science, 2003. **41**(15): p. 1685-1698.
130. Briozzo, A.C., M.F. Natale, and D.A. Tarzia, *The Stefan problem with temperature-dependent thermal conductivity and a convective term with a convective condition at the fixed face*. Communications on Pure and Applied Analysis, 2010. **9**(5): p. 1209-1220.
131. Voller, V.R. and F. Falcini, *Two exact solutions of a Stefan problem with varying diffusivity*. International Journal of Heat and Mass Transfer, 2013. **58**(1–2): p. 80-85.
132. Zhou, Y. and L.-j. Xia, *Exact solution for Stefan problem with general power-type latent heat using Kummer function*. International Journal of Heat and Mass Transfer, 2015. **84**: p. 114-118.
133. Yousefi, T., et al., *Experimental investigation on the performance of CPU coolers: Effect of heat pipe inclination angle and the use of nanofluids*. Microelectronics Reliability, 2013. **53**(12): p. 1954-1961.
134. Ho, C.J., L.C. Wei, and Z.W. Li, *An experimental investigation of forced convective cooling performance of a microchannel heat sink with Al₂O₃/water nanofluid*. Applied Thermal Engineering, 2010. **30**(2–3): p. 96-103.
135. Chein, R. and G. Huang, *Thermoelectric cooler application in electronic cooling*. Applied Thermal Engineering, 2004. **24**(14–15): p. 2207-2217.
136. Alawadhi, E.M. and C.H. Amon, *PCM thermal control unit for portable electronic devices: experimental and numerical studies*. IEEE Transactions on Components and Packaging Technologies, 2003. **26**(1): p. 116-125.
137. Fok, S.C., W. Shen, and F.L. Tan, *Cooling of portable hand-held electronic devices using phase change materials in finned heat sinks*. International Journal of Thermal Sciences, 2010. **49**(1): p. 109-117.
138. Setoh, G., F.L. Tan, and S.C. Fok, *Experimental studies on the use of a phase change material for cooling mobile phones*. International Communications in Heat and Mass Transfer, 2010. **37**(9): p. 1403-1410.
139. Raghavan, A., et al. *Computational sprinting*. in *IEEE International Symposium on High-Performance Comp Architecture*. 2012.
140. King, W.E., et al., *Laser powder bed fusion additive manufacturing of metals; physics, computational, and materials challenges*. Applied Physics Reviews, 2015. **2**(4): p. 041304.
141. Gao, D., Z. Chen, and L. Chen, *A thermal lattice Boltzmann model for natural convection in porous media under local thermal non-equilibrium conditions*. International Journal of Heat and Mass Transfer, 2014. **70**: p. 979-989.
142. Cárdenas, B. and N. León, *High temperature latent heat thermal energy storage: Phase change materials, design considerations and performance enhancement techniques*. Renewable and Sustainable Energy Reviews, 2013. **27**: p. 724-737.
143. Zhao, C.Y., *Review on thermal transport in high porosity cellular metal foams with open cells*. International Journal of Heat and Mass Transfer, 2012. **55**(13): p. 3618-3632.
144. Tian, Y. and C.Y. Zhao, *A numerical investigation of heat transfer in phase change materials (PCMs) embedded in porous metals*. Energy, 2011. **36**(9): p. 5539-5546.
145. Zhao, C.Y., W. Lu, and Y. Tian, *Heat transfer enhancement for thermal energy storage using metal foams embedded within phase change materials (PCMs)*. Solar Energy, 2010. **84**(8): p. 1402-1412.

146. Shabgard, H., et al., *High temperature latent heat thermal energy storage using heat pipes*. International Journal of Heat and Mass Transfer, 2010. **53**(15): p. 2979-2988.
147. Krishnan, S., J.Y. Murthy, and S.V. Garimella, *Direct Simulation of Transport in Open-Cell Metal Foam*. Journal of Heat Transfer, 2006. **128**(8): p. 793-799.
148. Karen M. B. Taminger, R.A.H., and Dennis L. Dicus, *Solid Freeform Fabrication: An Enabling Technology for Future Space Missions*. 2002 International Conference on Metal Powder Deposition for Rapid Manufacturing, San Antonio, TX; United States, 2002.
149. Soylemez, E., J.L. Beuth, and K. Taminger. *Controlling melt pool dimensions over a wide range of material deposition rates in electron beam additive manufacturing*. in *Proceedings of 21st Solid Freeform Fabrication Symposium, Austin, TX, Aug.* 2010.
150. Yadroitsev, I., et al., *Single track formation in selective laser melting of metal powders*. Journal of Materials Processing Technology, 2010. **210**(12): p. 1624-1631.
151. Yagi, S. and D. Kunii, *Studies on effective thermal conductivities in packed beds*. AIChE Journal, 1957. **3**(3): p. 373-381.
152. Masamune, S. and J.M. Smith, *Thermal Conductivity of Beds of Spherical Particles*. Industrial & Engineering Chemistry Fundamentals, 1963. **2**(2): p. 136-143.
153. Butt, J.B., *Thermal conductivity of porous catalysts*. AIChE Journal, 1965. **11**(1): p. 106-112.
154. Godbee, H.W. and W.T. Ziegler, *Thermal Conductivities of MgO, Al₂O₃, and ZrO₂ Powders to 850°C. II. Theoretical*. Journal of Applied Physics, 1966. **37**(1): p. 56-65.
155. Swift, D.L., *The thermal conductivity of spherical metal powders including the effect of an oxide coating*. International Journal of Heat and Mass Transfer, 1966. **9**(10): p. 1061-1074.
156. Luikov, A.V., et al., *Thermal conductivity of porous systems*. International Journal of Heat and Mass Transfer, 1968. **11**(2): p. 117-140.
157. Wakao, N. and K. Kato, *EFFECTIVE THERMAL CONDUCTIVITY OF PACKED BEDS*. Journal of Chemical Engineering of Japan, 1969. **2**(1): p. 24-33.
158. Wakao, N. and D. Vortmeyer, *Pressure dependency of effective thermal conductivity of packed beds*. Chemical Engineering Science, 1971. **26**(10): p. 1753-1765.
159. Batchelor, G. and R. O'brien. *Thermal or electrical conduction through a granular material*. in *Proceedings of the Royal Society of London A: Mathematical, Physical and Engineering Sciences*. 1977. The Royal Society.
160. Nozad, I., R.G. Carbonell, and S. Whitaker, *Heat conduction in multiphase systems—I*. Chemical Engineering Science, 1985. **40**(5): p. 843-855.
161. Hadley, G.R., *Thermal conductivity of packed metal powders*. International Journal of Heat and Mass Transfer, 1986. **29**(6): p. 909-920.
162. Tsotsas, E. and H. Martin, *Thermal conductivity of packed beds: A review*. Chemical Engineering and Processing: Process Intensification, 1987. **22**(1): p. 19-37.
163. Bala, K., et al., *Effective thermal conductivity of copper powders*. Journal of Physics D: Applied Physics, 1989. **22**(8): p. 1068.
164. Shonnard, D.R. and S. Whitaker, *The effective thermal conductivity for a pointcontact porous medium: an experimental study*. International Journal of Heat and Mass Transfer, 1989. **32**(3): p. 503-512.
165. Cheng, G.J., A.B. Yu, and P. Zulli, *Evaluation of effective thermal conductivity from the structure of a packed bed*. Chemical Engineering Science, 1999. **54**(19): p. 4199-4209.
166. Vargas, W.L. and J.J. McCarthy, *Conductivity of granular media with stagnant interstitial fluids via thermal particle dynamics simulation*. International Journal of Heat and Mass Transfer, 2002. **45**(24): p. 4847-4856.
167. Vargas, W.L. and J.J. McCarthy, *Heat conduction in granular materials*. AIChE Journal, 2001. **47**(5): p. 1052-1059.

168. Abou-Sena, A., A. Ying, and M. Abdou, *Experimental measurements of the effective thermal conductivity of a lithium titanate (Li₂TiO₃) pebbles-packed bed*. Journal of Materials Processing Technology, 2007. **181**(1–3): p. 206-212.
169. Zhang, H.W., et al., *A DEM study on the effective thermal conductivity of granular assemblies*. Powder Technology, 2011. **205**(1–3): p. 172-183.
170. Asakuma, Y., et al., *Thermal analysis with contact resistance of packed bed by a homogenization method*. Powder Technology, 2016. **291**: p. 46-51.
171. Gan, J., Z. Zhou, and A. Yu, *Effect of particle shape and size on effective thermal conductivity of packed beds*. Powder Technology, 2017. **311**: p. 157-166.
172. Giri, A. and P.E. Hopkins, *Analytical model for thermal boundary conductance and equilibrium thermal accommodation coefficient at solid/gas interfaces*. The Journal of Chemical Physics, 2016. **144**(8): p. 084705.
173. Sengers, J.V. and J.T.R. Watson, *Improved International Formulations for the Viscosity and Thermal Conductivity of Water Substance*. Journal of Physical and Chemical Reference Data, 1986. **15**(4): p. 1291-1314.
174. McElroy, D.L., et al., *The Physical Properties of Inconel Alloy 718 from 300 to 1000 K*, in *Thermal Conductivity 15*, V.V. Mirkovich, Editor. 1978, Springer US: Boston, MA. p. 149-151.
175. Rack, H.J., *Physical and mechanical properties of cast 17-4 PH stainless steel*, 1981, ; Sandia National Labs., Albuquerque, NM (USA). p. Medium: ED; Size: Pages: 63.
176. Zagula-Yavorska, M., et al. *The Effect of the Aluminide Coating on the Thermal Properties and Oxidation Resistance of Inconel 625 Ni-Base Superalloy*. in *Solid State Phenomena*. 2015. Trans Tech Publ.
177. Welsch, G., R. Boyer, and E. Collings, *Materials properties handbook: titanium alloys*. 1993: ASM international.
178. Ho, C.Y. and T. Chu, *Electrical resistivity and thermal conductivity of nine selected AISI stainless steels*, 1977, DTIC Document.
179. Parker, W.J., et al., *Flash Method of Determining Thermal Diffusivity, Heat Capacity, and Thermal Conductivity*. Journal of Applied Physics, 1961. **32**(9): p. 1679-1684.
180. Carslaw, H.S. and J.C. Jaeger, *Conduction of Heat in Solids*. 1986: Clarendon Press.
181. Reiter, F., J. Camposilvan, and R. Nehren, *Accommodation coefficient of noble gases on Pt surface from 80 K up to 450 K*. *Warme-und Stoffubertragung*, 1972. **5**(2): p. 325-334.
182. Bauer, R., *Ewektive radiale Wa (rmeleitfa (higkeit gasdurchstro (mter Schu (ttungen mit Partikeln unterschiedlicher Form und GroK ßenver-teilung*, 1976, Dissertation, University of Karlsruhe.
183. Semyonov, Y.G., S.F. Borisov, and P.E. Suetin, *Investigation of heat transfer in rarefied gases over a wide range of Knudsen numbers*. International Journal of Heat and Mass Transfer, 1984. **27**(10): p. 1789-1799.
184. Borisov, S.F., Y.G. Semenov, and P.E. Suetin, *Inert-gas energy-accommodation coefficients on tungsten*. Journal of engineering physics, 1982. **43**(6): p. 1394-1398.
185. Bolz, R.E., *CRC handbook of tables for applied engineering science*. 1973: CRC press.
186. Kennard, E.H., *Kinetic theory of gases with an introduction to statistical mechanics*. 1938.
187. Younglove, B.A. and H.J.M. Hanley, *The Viscosity and Thermal Conductivity Coefficients of Gaseous and Liquid Argon*. Journal of Physical and Chemical Reference Data, 1986. **15**(4): p. 1323-1337.
188. Schiffres, S.N., et al., *Gas Diffusion, Energy Transport, and Thermal Accommodation in Single-Walled Carbon Nanotube Aerogels*. Advanced Functional Materials, 2012. **22**(24): p. 5251-5258.
189. Kim, K., et al., *Radiative heat transfer in the extreme near field*. Nature, 2015. **528**(7582): p. 387-391.
190. Song, B., et al., *Near-field radiative thermal transport: From theory to experiment*. AIP advances, 2015. **5**(5): p. 53503.

191. Wachman, H.Y., *The thermal accommodation coefficient: a critical survey*. ARS Journal, 1962. **32**(1): p. 2-12.
192. Logan, R.M. and R.E. Stickney, *Simple Classical Model for the Scattering of Gas Atoms from a Solid Surface*. The Journal of Chemical Physics, 1966. **44**(1): p. 195-201.
193. Goodman, F.O. and H.Y. Wachman, *Formula for Thermal Accommodation Coefficients*. The Journal of Chemical Physics, 1967. **46**(6): p. 2376-2386.
194. Goodman, F.O., *Dynamics of gas-surface scattering*. 2012: Elsevier.
195. Roberts, J.K., *The Exchange of Energy between Gas Atoms and Solid Surfaces. II. The Temperature Variation of the Accommodation Coefficient of Helium*. Proceedings of the Royal Society of London. Series A, Containing Papers of a Mathematical and Physical Character, 1932. **135**(826): p. 192-205.
196. Thomas, L.B. and E.B. Schofield, *Thermal Accommodation Coefficient of Helium on a Bare Tungsten Surface*. The Journal of Chemical Physics, 1955. **23**(5): p. 861-866.
197. Moroz, G. *How Helium Improves Additive Manufacturing of Ti-6Al-4V and IN718 Parts*. in *RAPID + TCT 2017: 3D Printing & Additive Manufacturing Event*. 2017. Pittsburgh, PA, USA.
198. Mason, E.A. and S.C. Saxena, *Approximate Formula for the Thermal Conductivity of Gas Mixtures*. The Physics of Fluids, 1958. **1**(5): p. 361-369.
199. Butler, J.N. and R.S. Brokaw, *Thermal Conductivity of Gas Mixtures in Chemical Equilibrium*. The Journal of Chemical Physics, 1957. **26**(6): p. 1636-1643.
200. Lindsay, A.L. and L.A. Bromley, *Thermal conductivity of gas mixtures*. Industrial & Engineering Chemistry, 1950. **42**(8): p. 1508-1511.
201. Regner, K.T., L.C. Wei, and J.A. Malen, *Interpretation of thermoreflectance measurements with a two-temperature model including non-surface heat deposition*. Journal of Applied Physics, 2015. **118**(23): p. 235101.
202. Paddock, C.A. and G.L. Eesley, *Transient thermoreflectance from thin metal films*. Journal of Applied Physics, 1986. **60**(1): p. 285-290.
203. Capinski, W.S. and H.J. Maris, *Improved apparatus for picosecond pump-and-probe optical measurements*. Review of Scientific Instruments, 1996. **67**(8): p. 2720-2726.
204. Bonello, B., B. Perrin, and C. Rossignol, *Photothermal properties of bulk and layered materials by the picosecond acoustics technique*. Journal of Applied Physics, 1998. **83**(6): p. 3081-3088.
205. Taketoshi, N., et al., *Homodyne detection technique using spontaneously generated reference signal in picosecond thermoreflectance measurements*. Review of Scientific Instruments, 2003. **74**(12): p. 5226-5230.
206. Cahill, D.G., *Analysis of heat flow in layered structures for time-domain thermoreflectance*. Review of Scientific Instruments, 2004. **75**(12): p. 5119-5122.
207. Schmidt, A.J., R. Cheaito, and M. Chiesa, *A frequency-domain thermoreflectance method for the characterization of thermal properties*. Review of Scientific Instruments, 2009. **80**(9): p. 094901-6.
208. Regner, K.T., et al., *Broadband phonon mean free path contributions to thermal conductivity measured using frequency domain thermoreflectance*. Nat Commun, 2013. **4**: p. 1640.
209. Regner, K.T., S. Majumdar, and J.A. Malen, *Instrumentation of broadband frequency domain thermoreflectance for measuring thermal conductivity accumulation functions*. Review of Scientific Instruments, 2013. **84**(6): p. -.
210. Koh, Y.K. and D.G. Cahill, *Frequency dependence of the thermal conductivity of semiconductor alloys*. Physical Review B, 2007. **76**(7): p. 075207.
211. Wilson, R. and D.G. Cahill, *Anisotropic failure of Fourier theory in time-domain thermoreflectance experiments*. Nature communications, 2014. **5**: p. 5075.
212. Liao, B., J. Zhou, and G. Chen, *Generalized Two-Temperature Model for Coupled Phonon-Magnon Diffusion*. Physical Review Letters, 2014. **113**(2): p. 025902.

213. Choi, G.-M., R.B. Wilson, and D.G. Cahill, *Indirect heating of Pt by short-pulse laser irradiation of Au in a nanoscale Pt/Au bilayer*. Physical Review B, 2014. **89**(6): p. 064307.
214. Wilson, R.B., et al., *Two-channel model for nonequilibrium thermal transport in pump-probe experiments*. Physical Review B, 2013. **88**(14): p. 144305.
215. Jiang, L. and H.-L. Tsai, *Improved Two-Temperature Model and Its Application in Ultrashort Laser Heating of Metal Films*. Journal of Heat Transfer, 2005. **127**(10): p. 1167-1173.
216. Tas, G. and H.J. Maris, *Electron diffusion in metals studied by picosecond ultrasonics*. Physical Review B, 1994. **49**(21): p. 15046-15054.
217. Qiu, T.Q. and C.L. Tien, *Short-pulse laser heating on metals*. International Journal of Heat and Mass Transfer, 1992. **35**(3): p. 719-726.
218. Kaganov, M., *Relaxation between electrons and the crystalline lattice*. Sov. Phys. JETP, 1957. **4**: p. 173-178.
219. Regner, K.T., A.J.H. McGaughey, and J.A. Malen, *Analytical interpretation of nondiffusive phonon transport in thermoreflectance thermal conductivity measurements*. Physical Review B, 2014. **90**(6): p. 064302.
220. Regner, K.T., J.P. Freedman, and J.A. Malen, *Advances in Studying Phonon Mean Free Path Dependent Contributions to Thermal Conductivity*. Nanoscale and Microscale Thermophysical Engineering, 2015. **19**(3): p. 183-205.
221. Bennon, W. and F. Incropera, *Developing laminar mixed convection with solidification in a vertical channel*. ASME J. Heat Transfer, 1988. **110**: p. 410-415.
222. Promoppatum, P., et al., *Experimental and numerical investigation of the cross-flow PCM heat exchanger for the energy saving of building HVAC*. Energy and Buildings, 2017. **138**: p. 468-478.